ISSN: 2639-0108

Research Article

Advances in Theoretical & Computational Physics

# Sgr A*, M87* and OJ287 as Extreme Central Binaries of Supermassive Black Holes--Confirmation and extension of decameter radio wave observation results through VLBI data comparison

**Hiroshi Oya***

*Geophysical Department, Graduate School for Science, Tohoku University; and Astrophysics Research Task, Seisa University.*

***Corresponding Author**
Hiroshi Oya, Geophysical Department, Graduate School for Science, Tohoku University; and Astrophysics Research Task, Seisa University. Japan.

**Submitted:** 2024, Feb 19; **Accepted:** 2024, Mar 26; **Published:** 2024, Apr 20

**Citation:** Oya, H. (2024). Sgr A*, M87* and OJ287 as Extreme Central Binaries of Supermassive Black Holes--Confirmation and extension of decameter radio wave observation results through VLBI data comparison. *Adv Theo Comp Phy, 7*(2), 01-57.

## Abstract

*Based on a deduced 2153±5 s orbiting period of the extreme central binary of the supermassive black hole (ECB-SMBH), at Sgr A*,that is confirmed being based on the decameter radio wave pulse observations compared with 1.3 mm wavelength very long baseline interferometry (VLBI) data from the event horizon telescope (EHT-Data), we depict moving images of Sgr A* from EHT-Data, confirming further the existence of ECB-SMBH. The results show that radio wave images of the two members of ECB-SMBH are radio-bright objects due to emissions caused by source agents accreting from a thick disk toward ECB-SMBH. We extend the confirmed concept of ECB-SMBH to the interpretation of M87*, based on two images released by Miyoshi et al. in 2022 using EHT-Data and by Lu et al. in 2023 using the 3.5 mm wavelength data from the Global Millimeter VLBI Arrays as core telescopes. For the double brilliant spots displayed in two different images of M87*, we consider them the same two objects that shift locations during the 369-day interval of the observation periods of the two images. It is concluded that M87* A and M87* B (temporarily named) are orbiting with a period of 168.8 d at velocities of (6.28±0.54)% and (16.7±1.5)% of the speed of light, respectively. For the existence of ECB-SMBH, the condition of "no gravitational wave radiation" from the SMBH is essential. Regarding the secondary BH of blazar OJ 287, we find around 58~60-year period oscillation of the orbiting period, which is recently in a shortening phase. By applying the concept of ECB-SMBH to the OJ287 primary BH, whose orbiting period is approximately 1.6 yr, we interpret that the orbital period variation of the secondary BH is not due to the radiation of gravitational waves but is caused by the orbital motions of ECB-SMBH.*

## 1. Introduction

In parallel to the search for a central concentration of matter, identified as a supermassive black hole through the observations of movements of stars around Sgr A* , [1−5], the quest to capture images with radio waves that reflect the existence of a possible supermassive black hole began to make progress , [6,7] The event horizon telescope (EHT), using globally developed network of 1.3 mm very long baseline interferometry (VLBI), conducted observations in 2017, and the image of Sgr A* was released in 2022 , [8−13].

Independently of the aforementioned efforts, observations using a decameter radio wave interferometer for Sgr A* have been ongoing for 20 years at Tohoku University, aiming to detect decameter wavelength pulses at 21.86 MHz, whose timings coincide with the spinning periods of rotating black holes (Kerr BHs). After developing the devices and methods for data analysis, the results were published in 2019 [14] based on observations made in 2016 and 2017, showing the existence of two intrinsic pulses with frequencies of 173±1 s and 148±1 s, which are associated with multiple sidebands corresponding to a period of 2200±50 s. These results indicated the existence of a binary system of Kerr BHs with masses of $(2.27\pm0.02)\times10^6\ M_\odot$ (named Gaa) and $(1.94\pm0.01)\times10^6\ M_\odot$ (named Gab). Assuming Keplerian circular orbits based on Newtonian dynamics, the radii of Gaa and Gab are deduced to be $1.89\times10^{12}$cm and $2.21\times10^{12}$ cm, respectively, with orbiting velocities of 18% and 21% of the speed of light for Gaa and Gab, respectively. Given the current understanding of gravitational wave radiation, especially after extensive reports of successful observations [15-18] of gravitational waves from potential stellar mass black holes, these results were initially considered unrealistic and incorrect by standard evaluations. However, we interpret these observation results as evidence necessitating a clarification in the physics of gravitational wave generation, particularly for supermassive black holes whose average material densities within the event horizon become extremely tenuous, as function inversely proportional to the square of the total mass.

Consequently, we published a theory on gravitational waves for supermassive black holes [19], stating "No gravitational wave from orbiting supermassive Kerr black holes." Here, we introduce the terminology "the extreme central binary of the supermassive black hole" (ECB-SMBH) about the reported supermassive black hole at Sgr A*, coupled with the theory of no gravitational waves from orbiting supermassive Kerr black holes. The aim of this paper is, therefore, to find confirmation for the existence of ECB-SMBH.

Contrary to initial expectations that the published Sgr A* image from EHT might serve as the standard for confirming the existence of supermassive BH at Sgr A*, criticisms have been raised regarding flaws in the EHT image results [20]. Initially the indication of erroneous processes for formation of the EHT image arose from the imaging of M87* [21-26], whose basic data were collected in April 2017 during the same EHT campaign as the Sgr A* observations. Without addressing the fundamental issues in the process of constructing source maps from the observed visibility data, the EHT collaboration (EHTC) released the image of Sgr A*.

As a first step toward confirming the proposed existence of ECB-SMBH at Sgr A*, we investigated the results of 1.3 mm wavelength VLBI observations carried out by Fish et al. (F-paper) [27], comparing the time-variation data provided by the F-paper. with a constructed" radiation model of 1.3 mm wavelength radio waves, applying the possible ECB-SMBH parameters derived from decameter radio wave pulse observations" (DRWP-Model). The results [28] indicated an orbital period of 2150±2.5 s, nearly matching the predicted range of 2200±50 s, showing consistency with the time-variation results of the F-paper

The second step of confirmation was carried out [29], using publicly released EHT data [30], independent of the analyses of the EHTC. To confirm the existence of ECB-SMBH, the model (DRWP-Model) was based on parameters concluded from decameter radio wave pulse observations to predict possible visibilities by the corresponding baselines of the VLBI system of the EHT. The process revealed a high correlation level between the observed EHT visibility data and DRWP-Model, affirming the existence of ECB-SMBH with an orbiting period of 2193±27 s [29]. To solidify these results, the third step are carried out in the present works recovering the moving image of ECB-SMBH from the EHT-VLBI visibility data [30], using the established orbiting period as an essential key.

In Section 3, we describe the principle of the recovering the moving source image. The data processing approach markedly differs from the current method of the radio wave source mapping from VLBI visibility data in that the objects of the data are assumed to be stationary. Because ECB-SMBH at SgrA* is moving as a fundamental characteristic we should pick up the observed visibilities as a sequential series of static data from the original dataset, synchronizing it with the existing variation period. Owing to the special situation of ECB-SMBH at Sgr A*, whose orbital plane is almost edge-on, inclined by only 6° with respect to the line of sight, the black holes' movements can be approximately described as a back-and-forth motion along the orbit line. This allows us to approximate the source image in a one-dimensional configuration without resorting to the orthodox method of two-dimensional radio source mapping typically utilized in VLBI studies. In this one-dimensional approach, we apply analyses of one-dimensional Fourier and inverse Fourier transformations with respect to the linearized visibility along the orbit line, as detailed in Sections 3 and 4.

After confirming the existence of ECB-SMBH at Sgr A* by recovering the moving image of the BH's from EHT visibility data, we extend the confirmation to a fourth stage. By applying the essence of radio wave sources surrounding ECB-SMBH, we apply the concept of ECB-SMBH to interpret the published VLBI observation images of M87* (the core of galaxy M87). As discussed in Section 5, for the published two mm wavelength VLBI images of M87* [20,31] showing two bright spots in each image, we apply the concept of the ECB-SMBH taking the couple of bright spots as radio wave emitting zones surrounding BHs, drawing on the results from the Sgr A* case.

In progressing the steps to confirm ECB-SMBH, the blazar OJ287 presents a significant challenge because of reports of the existence of the gravitational wave reaction [47,48], on the orbiting supermassive BH (secondary BH). In Section 6, we discuss that the commonly accepted concept of the in-spiral stage of the secondary SMBH due to gravitational wave generation reactions is incorrect, proposing instead the existence of ECB-SMBH as an alternative mechanism involving the primary SMBH. After an investigation of the historical records of OJ287's luminosity with burst timing [47] related to the secondary BH's movement across the accreting disk of the primary BH of OJ287 system, we clarified that the orbiting period of the secondary BH varies periodically, with a cycle of approximately 58~ 60 yr. This modulation in the secondary BH's orbiting period can be explained by the existence of ECB-SMBH, whose member BHs are orbiting with a period around1.6 yr. Studies on the jet [48] revealed that it shows presession motion with clear nutation, with a period of 1.60±0.1 yr. We infer that in the process of accelerating plasma in the jet through electromagnetic force, the orbital motions of ECB-SMBH impart energy, reflecting an orbital period of approximately 1.6 yr as the nutation period of the jet.

## 2. Brief Review for Step 2 Confirmation of Existing ECB-SMBH at Sgr A*[29]

The second step in confirming the existence of ECB-SMBH, (illustrated in Figure 1), begins with constructing the decameter radio wave pulse (DRWP-Model:see Introduction). This model aims to find correlations between the VLBI data from the EHT and ECB-SMBH resulted from observed DRWPs. DRWP-Model is thus constructed to represent the real existence of ECB-SMBH for 1.3 mm wavelength VLBI observations, accommodating all baselines within the globally distributed EHT system. Specifically, DRWP-Model delineates the orbital geometry and actual orbital plane configuration, observing an angle of 33μas for an orbit size of $4.1 \times 10^7$km at Sgr A*, where the two black holes orbit with a period 2200±50 s, (as depicted in Figure 2).

The EHT observations of Sgr A* were conducted on April 6 and April 7, 2017. The data, captured at high (229.1 GHz) and low (227.1 GHz) frequencies by 8 antennas located at globally distributed stations, were correlated to produce visibility data corresponding to 24 sets of baselines through two data handling pipelines, rPICARD (CASA) and HOPS. Consequently, we accessed eight types of visibility data from each pair of observation stations, totaling 24 pairs. The VLBI data from the EHT, when compared with the constructed DRWP-Model, comprise a full visibility dataset. This dataset consist of baseline lengths given by u and v coordinates, amplitude and phase of visibilities, along with the sigma of observed values listed as functions of observation timing, with intervals of 10 s corresponding to the average timing of the data.

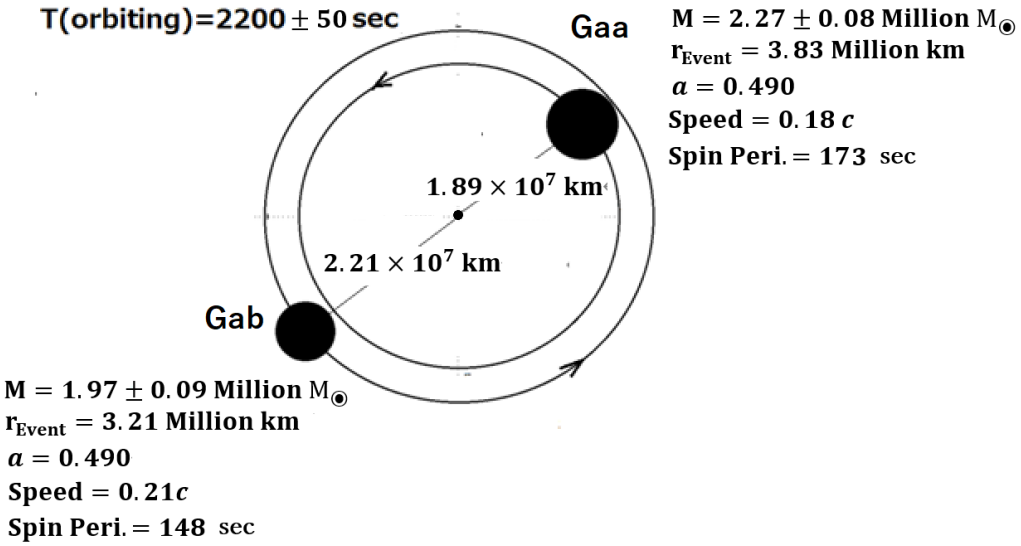


**Figure 1.** Configuration of ECB-SMBH confirmed from FFT spectra for decameter wavelength radio waves from Sgr A*, assuming that pulse frequencies are synchronized with spins of SMBHs Gaa and Gab subjected to Doppler effect produced via orbital motion. Distance between two SMBHs is 2.84 R_ss with respect to Schwartzschild radius R_ss if we assume a non rotating single BH. (After Oya [14,28]).

In this step2 confirmation paper, we did not use the visibility data as regular usages to form the source mapping but tried to find correlation between the DRWP-Model that contains the periodic variation of the orbiting ECB-SMBH and constructed as a model visibility detected by the VLBI system with the baseline corresponding to the same baseline to obtain the EHT visibility. From the perspective of investigating time variation, the EHT-VLBI visibilities can be morphologically classified into three categories based on the observation baseline length: these are, the case of short baseline whose length is shorter than 3 Gλ, the case of medium baseline whose length is in a range from 3 Gλ to 6 Gλ, and long baseline whose length is longer than 6 Gλ. The visibilities within the medium and long categories are characterized by a spread of visibility levels over time, displaying data oscillations with peak-to-peak (P-P) amplitudes below 2 Jy. Although there is mention of some systematic oscillation in the EHTC paper [32], the predominant understanding [32,33] is that time variations are mostly random noises associated with intrinsic and stochastically stationary levels of emission from sources around Sgr A*, except for the case of report of orbital motion of the hotspot in magnetized plasma. Therefore, independent of the ETHC 's approach, it has been clarified that the oscillatory visibilities of the VLBI-EHT data represent a mix of random noise and radio wave emissions closely related to the orbital motions associated with ECB-SMBH. With an orbit size of $4.1\times10^7$ km as determined by DRWP observations, for a baseline length of approximately

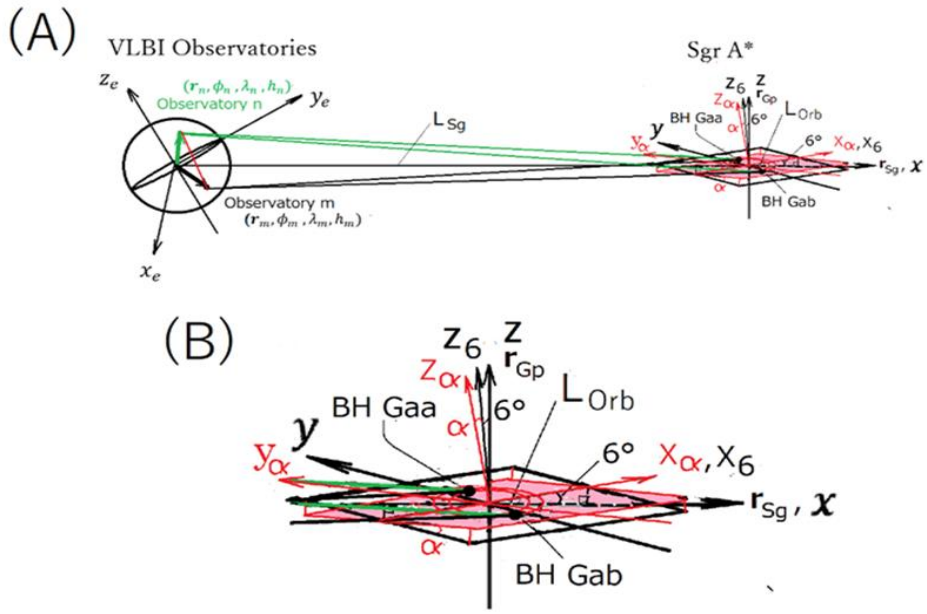


**Figure 2.** Geometrical relations between the rotating ECB-SMBH at SgrA* and EHT-VLBI observatories (m) and (n) for construction of DRWP-Model. (A) Over all description. The orbiting ECB-SMBH Gaa and Gab are described in the Cartesian coordinate with the origin at the center of SgrA* ; the direction of x-axis coincides with the unit vector $\hat{k}_{Sg}$ that is defined to coincide with the direction to connect between the earth's center and the center of SgrA*.The y axis of the reference coordinate prepared to describe the ECB-SMBH orbital plane is set to be vertical to x axis and also to the Galactic north pole direction to be in parallel with the Galactic plane . The location of the VLBI observatories of EHT are described in the regular astronomical coordinate of the equatorial-spring equinox system whose $z_e$ axis coincides with the axis of the earth rotation with parameters $r_m$,$\varphi_m$,$\lambda_m$ and $h_m$ for observatory m, respectively for the distance between the earth center, longitude, latitude and the height from the sea surface. The distance from the earth center and the center of the SgrA* is given by $L_{sg}$ meanwhile the distance between ECB-SMBH Gaa and Gab is expressed by $L_{Orb}$ . (B) Fine description of ECB-SMBH plane with respect to the reference coordinate. The orbital plane of ECB-SMBH is set with two inclination steps ; these are the 6 degree inclination of ECB-SMBH orbital plane looking from the Earth and inclination which is described as tilt of the normal direction of the ECB-SMBH orbital plane from the Galactic north pole direction by the angle α(see red vector) ; the new y direction in the inclined ECB-SMBH plane is defined as $y_\alpha$ . The real case of inclined angle $\alpha$ is searched by finding maximum correlation between the EHT-Data and DRWP-Model.(After Oya [29])

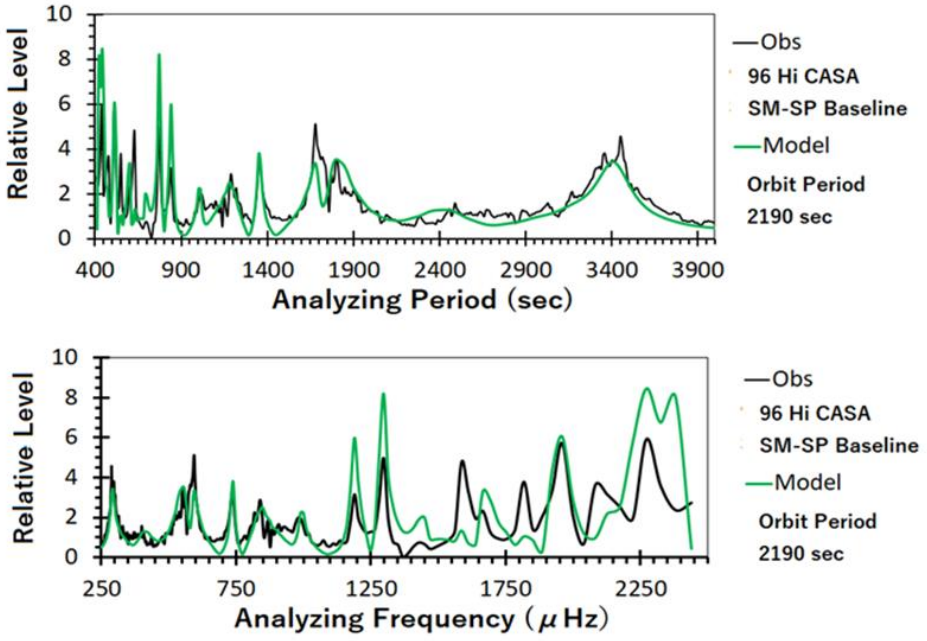


**Figure 3.** Final results showing coincidence of the Modified Fourier Transformation (MDFT) for EHT-Data (black curve) and the MDFT for DRWP-Model (green curve). Via the identity of the results, it can be concluded that the EHT-Data have definitely the component of the steady time variation coinciding with the ECB-SMBH orbiting period of 2190 sec prepared in DRWP-Model. (After Oya [29]).

3 Gλ begin to reveal a correlated signal from the area of orbiting ECB-SMBH motions (ECB-SMBH signal) when we estimate the distance of Sgr A* to be 8.3 kpc from the Earth. Through a morphological study of medium and long baselines, it is roughly estimated that the ratio of ECB-SMBH signal to random noise ranges from approximately 0.5 to 6.

In our comparative analysis, we directly calculated the numerical correlation factors between EHT observation data (EHT-Data) and DRWP-Model for three example cases of baselines. These baselines provide geometric parameters for the orbits of ECB-SMBH as outlined in our constructed model. Through this process, we sought coincidences between EHT-Data and DRWP-Model, determining that the orbital plane of ECB-SMBH aligns closely with the Galactic plane, deviating by no more than ±3° in the direction perpendicular to the Earth–Sgr A* line. Moreover, there is a tilt in the orbital plane of ±6° degrees in the direction of the Earth–Sgr A* line, as previously established [28].

| Abbreviation | Location | Latitude | Longitude | Elevation (m) |
|---|---|---|---|---|
| LM | Mexico | $+18^{\circ}59'08''.8$ | $-97^{\circ}18'53''.2$ | 4593.3 |
| SM | Hawaii USA | $+19^{\circ}49'27''.2$ | $-155^{\circ}28'39''.1$ | 4115.1 |
| AZ | Arizona USA | $+32^{\circ}42'05''.8$ | $-109^{\circ}53'28''.5$ | 3158.7 |
| SP | Antarctica | $-89^{\circ}59'22''.9$ | $-45^{\circ}15'00''.3$ | 2816.5 |

**Table 1. Locations of EHT-VLBI stations selected from original information [21].**

Although direct comparisons between EHT-Data and DRWP-Model showed a clear coincidence, suggesting the existence of ECB-SMBH with an accurate geometrical relationship, we opt for the modified Fourier transformation (MDFT) as our principal method of comparison. This choice was made to eliminate the disturbances of a significant fraction of coexisting random noise. Furthermore, the visibility data from EHT-VLBI in the medium and long baseline categories, directly relevant to the existence of ECB-SMBH, were sampled intermittently with unique data sampling time window (DSTWs), featuring quasi-periodic pauses approximately 1000 to 1100 s. These DSTWs complicate direct comparisons, especially in identifying existing periodic variations in data with short characteristic periods. The MDFT approach goes beyond a simple application of Fourier transformation to EHT-Data and DRWP-Model; it satisfies the requirement to apply a function equivalent to the application of deconvolution processes to compensate the biased effects of inhomogeneous data sampling windows. Instead of applying deconvolution directly within the MDFT method, our second confirmation paper introduced the use of Fourier transformation on white noise (random noise series); noises are generated in complete synchronizing timing with the data sampling windows of the EHT-VLBI observations prepared as a third Fourier transformation value S(ω), with angular frequency ω, independent of the Fourier transformation values of EHT-Data and DRWP-Model (also sampled in synchronization with EHT-VLBI data sampling windows). The MDFT was then defined as the Fourier-transformed function divided by S(ω),and we compared the MDFT calculated for EHT-Data with the MDFT calculated for the DRWP-Model. An example of this comparison, shown in Figure 3, demonstrates the coincidence of the two MDFTs for EHT-Data and DRWP-Model after adjusting two free parameters [29] and accurately identifying the orbiting period in the DRWP-Model where the orbiting periods of ECB-SMBH are set in the searching range. By selecting three baselines SM-SP, AZ-SP, and LM-SM, where information for each station

| Baseline | Day | Frequency | Pipeline | Period (sec) |
|---|---|---|---|---|
| AZ-SP | 96 | Hi | CASA | 2185 |
| | | Hi | HOPS | 2220 |
| | | Lo | CASA | 2235 |
| | | Lo | HOPS | 2240 |
| | 97 | Hi | CASA | 2200 |
| | | Hi | HOPS | 2180 |
| | | Lo | CASA | 2220 |
| | | Lo | HOPS | 2225 |
| SM-SP | 96 | Hi | CASA | 2190 |
| | | Hi | HOPS | 2140 |
| | | Lo | CASA | 2215 |
| | | Lo | HOPS | 2140 |
| | 97 | Hi | CASA | 2190 |
| | | Hi | HOPS | 2170 |
| | | Lo | CASA | 2195 |
| | | Lo | HOPS | 2190 |
| LM-SM | 96 | Hi | CASA | 2175 |
| | | Hi | HOPS | 2150 |
| | | Lo | CASA | 2195 |
| | | Lo | HOPS | 2175 |
| | 97 | Hi | CASA | 2235 |
| | | Hi | HOPS | 2195 |
| | | Lo | CASA | 2205 |
| | | Lo | HOPS | 2175 |
| Average | | | | 2193.3 |
| STD | | | | 27.5 |

**Table 2. Results of comparison of EHT-Data and DRWP-Model with finding ECB.**

provided by EHTC is listed in Table 1. The lengths of SM-SP, AZ-SP, and LM-SM baseline are 7.89 Gλ, 8.39 to 8.46 Gλ, and 4.23 to 4.26 Gλ, respectively; we searched for the orbital periods of a potential ECB-SMBH within the range of 2100–2245 s. The results are detailed in Table 2. To ascertain that the variation in the resulting period is not a true variation but rather stochastic ambiguity attributable to existing noise, we analyzed all eight possible data sets for each baseline and averaged the 24 results obtained using the MDFT method. The aggregated results yield an orbital period for ECB-SMBH of 2193.3 s with a standard deviation of 27.5 s. We can thus assert that the time variations observed in VLBI data of Sgr A* from the 2017 EHT campaign exhibit periodicity. This periodicity aligns with the presence of ECB-SMBH within the error margin at Sgr A*, where ECB-SMBH is orbiting with a period of 2200 ± 50 sec and radius of $4.1\times10^7$ km in the plane nearly parallel to the Galactic equatorial plane.

## 3. Sampling and Stacking of EHT Visibilities Data Synchronized with Orbiting Period of ECB-SMBH

### 3.1 Linearized Visibility

#### 3.1.1 Coordinate Transformation of Baseline of VLBI

As discussed in Section 2, it is known that the orbital plane of ECB-SMBH is almost parallel to the Galactic equatorial plane, with a slight inclination of 6° toward or away from the line of sight from observation points. Therefore, we can approximately describe the observing orbital motion of ECB-SMBH as linearly constrained visibilities in the EHT-VLBI system.

The radio wave source $S(\xi,\eta)$ at the right ascension $\xi$ and declination η, is expressed by the VLBI visibility $V(u,v)$ using a two-dimensional baseline distribution (u,v) [34] as follows:

$$S(\xi,\eta) = \int\int V(u,v)exp[i(\xi u + \eta v)]dudv \tag{3.1}$$

To describe $S(\xi,\eta)$, we adhere to the same framework employed in previous investigation [29] for the relationship between the EHT observation system and assumed orbit of the ECB-SMBH motion, as depicted in Figure 2. Here, the directions of Sgr A* and Galactic north pole are denoted by unit vectors $\hat{x}$ and $\hat{z}$, respectively. In this Cartesian coordinate system, we can define the unit vector, $\hat{y}$ as parallel to the Galactic equator, which is considered approximately parallel to the orbital plane of ECB-SMBH. By denoting the unit vector $\hat{x}_e$ as directed toward the Sun at the spring equinox at UT 0 and unit vector $\hat{z}_e$ as directed toward the north of Earth's rotation axis with $\hat{y}_e$ perpendicular to both $\hat{x}_e$ and $\hat{z}_e$, we establish a conventional astronomical coordinate system. The unit vectors $\hat{x}$, $\hat{y}$, and $\hat{z}$ are described as follows:

$$\hat{x} = cos\delta_{Sg}cos\phi_{Sg}\hat{x}_e + cos\delta_{Sg}sin\phi_{Sg}\hat{y}_e + sin\delta_{Sg}\hat{z}_e.$$

$$\begin{aligned}\hat{y} = {} & \left(cos\delta_{Gp}sin\delta_{Sg}sin\phi_{Gp} - cos\delta_{Sg}sin\delta_{Gp}sin\phi_{Sg}\right)\hat{x}_e \\ & + \left(cos\delta_{Sg}sin\delta_{Gp}cos\phi_{Sg} - sin\delta_{Sg}cos\delta_{Gp}cos\phi_{Gp}\right)\hat{y}_e \\ & + \left(cos\delta_{Sg}sin\phi_{Sg}cos\delta_{Gp}cos\phi_{Gp} \right. \\ & \left. - cos\delta_{Sg}cos\phi_{Sg}cos\delta_{Gp}sin\phi_{Gp}\right)\hat{z}_e \quad (3.2)\end{aligned}$$

and

$$\hat{z} = cos\delta_{Gp}cos\phi_{GP}\hat{x}_e + cos\delta_{GP}sin\phi_{GP}\hat{y}_e + sin\delta_{GP}\hat{z}_e. \quad (3.3)$$

where $\phi_{Sg}$ and $\delta_{Sg}$ are the right ascension and declination of Sgr A*, respectively; and $\phi_{Gp}$ and $\delta_{Gp}$ are the right ascension and declination of North Galactic pole. Further, we introduce unit vectors $\hat{u}$ and $\hat{v}$ to describe the baseline vectors parallel to the variation direction of the right ascension and the declination, respectively:

$$\hat{u} \equiv \frac{\partial \hat{x}}{cos\delta_{Sg}\partial\phi_{Sg}} = -sin\phi_{Sg}\hat{x}_e + cos\phi_{Sg}\hat{y}_e, \quad (3.4)$$

and

$$\hat{v} \equiv \frac{\partial \hat{x}}{\partial\delta_{Sg}} = -sin\delta_{Sg}cos\phi_{Sg}\hat{x}_e - sin\delta_{Sg}sin\phi_{Sg}\hat{y}_e + cos\delta_{Sg}\hat{z}_e \quad (3.5)$$

By defining the unit vector $\hat{w}$ as parallel to the line of sight, i.e., the direction toward Sgr A*, we can form another Cartesian coordinate system (u,v,w), that is:

$$\hat{w} = cos\delta_{Sg}cos\phi_{Sg}\hat{x}_e + cos\delta_{Sg}sin\phi_{Sg}\hat{y}_e + sin\delta_{Sg}\hat{z}_e \quad (3.6)$$

In Appendix A, the unit vector $\hat{y}$, parallel to the ECB-SMBH motion in orbit as described in u-v plane, is given by:

$$\begin{aligned}\hat{y} = {} & \left[cos\delta_{Sg}sin\delta_{Gp} - sin\delta_{Sg}cos\delta_{Gp}cos\left(\phi_{Gp} - \phi_{Sg}\right)\right]\hat{u} \\ & -\left[cos\delta_{Gp}sin\left(\phi_{Gp} - \phi_{Sg}\right)\right]\hat{v} \quad (3.7)\end{aligned}$$

At this juncture, we define the inclination angle $\theta_0$ between the vectors $\hat{y}$ and $\hat{u}$ as follows:

$$cos\theta_0 = cos\delta_{Sg}sin\delta_{Gp} - sin\delta_{Sg}cos\delta_{Gp}cos\left(\phi_{Gp} - \phi_{Sg}\right). \quad (3.8)$$

The fundamental relation of VLBI given in eq.(3.1) can be transformed from the u,v coordinate system to the $(\ell,\tilde{t})$system, where the source mapping is expressed in the p, q system via transforming relations that are detailed as follows:

$$\ell = u \cdot cos\theta_0 + v \cdot sin\theta_0, \qquad (3.9-1)$$

$$\tilde{t} = -u \cdot sin\theta_0 + v \cdot cos\theta_0, \qquad (3.9-2)$$

This allows the EHT visibilities to be represented in this newly established baseline coordinate system, as follows:

$$S(\mathrm{p},\mathrm{q}) = \int\int V^*(\ell,\tilde{t},\theta_0)exp[i(\mathrm{p}\ell + \mathrm{q}\tilde{t})]d\ell d\tilde{t} \qquad (3.10)$$

where

$$V^*(\ell,\tilde{t},\theta_0) = V(\ell cos\theta_0 - \tilde{t}sin\theta_0, \ell sin\theta_0 + \tilde{t}cos\theta_0), \quad (3.10-1)$$

$$p = \xi cos\theta_0 + \eta sin\theta_0 \ , \qquad (3.10-2)$$

and

$$q = -\xi sin\theta_0 + \eta cos\theta_0 \ . \qquad (3.10-3)$$

### 3.1.2 Linearized Visibility (LV)

To describe the visibility constrained to express the orbiting ECB-SMBH detected as linear motion from observation points, we introduce the concept of linearized visibility (LV), which allows us to focus on the linear motion of ECB-SMBH from the two-dimensional EHT visibility data. Initially, without specifying the orbit inclination angle $\theta_0$ with respect to the u-axis, we further expand the coordinate system to describe the LV. By defining a new inclination angle $\theta$, as

$$\theta_0 - \varepsilon < \theta < \theta_0 + \varepsilon\,, \qquad (3.11)$$

where ε is a limit angle that permits the two-dimensional visibility to be approximated as one-dimensional visibility along the line with inclination angle $\theta_0$; we can reformulate eq.(3.10) as follows:

$$S(\mathrm{p},\theta_0) = \int\int_{\theta_0-\varepsilon}^{\theta_0+\varepsilon} V^*(\ell\cos\theta,\ell\sin\theta,\theta)\cdot exp[i(\mathrm{p}\ell + \mathrm{q}\tilde{t})]\cdot \ell d\ell d\theta \ . \qquad (3.12)$$

The limit angle $\varepsilon$, chosen to be as narrow as possible, focuses on the line of ECB-SMBH to concentrate on the analysis of periodically varying components in the EHT visibility data. However, due to the presence of noise and potential observational errors, there is a lower limit for selecting $\varepsilon$.

Related to eq.(3.12), we define the LV, tailored for detecting sources moving with a length parameter p along a line with inclination angle θ, as follows:

$$V_L(\ell,\theta_0) = \int_{\theta_0-\varepsilon}^{\theta_0+\varepsilon} V^*(\ell\cos\theta,\ell\sin\theta,\theta_0)\ell d\theta \ . \qquad (3.13)$$

This method of handling visible data, referred to as linearized visibility (LV), allows eq.(3.10) to be finally expressed by setting q=0, as follows:

$$S(\mathrm{p},\theta_0) = \int\int V_L(\ell,\theta_0)exp(i\mathrm{p}\ell)d\ell \qquad (3.14)$$

This indicates that data deviating from the orbit line are unrelated to periodic time variation due to their independence from ECB-SMBH orbital motion. Consequently, by sampling data synchronized with the orbiting motion's period, components unrelated to ECB-SMBH are averaged out, resulting in a constant bias level similar to averaging random noise.

### 3.2 Symmetry Approximation and Synchronized Data Stacking of LV

We now consider the periodic time dependence of VLBI visibility. Traditionally, VLBI study assumes statistically stationary sources. However, by viewing original visibility as data from time-varying sources, which change according to a given time sequence, we adopt a novel approach. Utilizing the identified orbiting period, we form the LV based on EHT data by sampling synchronized with the eclipse cycle of BHs, which is

half of the orbital period of ECB-SMBHB. In developing the LV, we aim to simplify the SgrA* system by assuming symmetry for both members of the binary system, without losing the essence of the phenomena. The symmetric approximation model for ECB-SMBH, illustrated in Figure 4, assumes both ECB-SMBH members of the binary system are identical, employing a unified circular orbit with a radius assumed to be the same as the actual distance, i.e., $4.1\times10^7$ km. By assuming 1 to 1 ratio of the binary members Gaa and Gab contrary to the real mass ratio of 1 to 0.87, the model's positions, deviate from actual positions by less than 8%, which is sufficiently smaller than the limit range detectable by the EHT's VLBI system. Therefore, this symmetry approximation is utilized throughout the entire process to deduce the image of ECB-SMBH motions from EHT data.

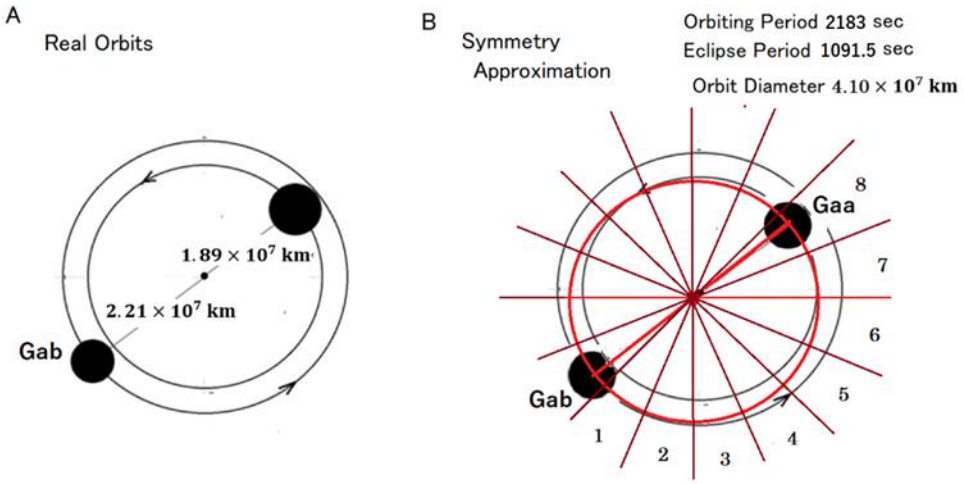


**Figure 4.** The symmetry approximation of ECB-SMBH at SgrA*. Panel A shows real situation of the ECB-SMBH at SgrA*; the symmetrically approximated orbit is given in Panel B where the configuration is twisted by 8% from the real orbits. The positions of symmetrically assumed orbit of ECB-SMBH are expressed by dividing 16 phases; eight positions numbering from 1 to 8 are selected as essential positions to descrive the orbital motion considering the symmetry of the configuration of the approximated orbit.

For the anticipated periodic time-varying LV, we have set eight phases corresponding to the approximated symmetry orbit as depicted in Figure 4. The entire period of the VLBI observation (one day of observation) is represented by LVs corresponding to these eight sampling phases, because of the periodic repetition of the orbital motions of ECB-SMBH. Consequently, eq.(3.13) is reformulated as :

$$V_L(\ell,\theta,T_m) = \frac{1}{N}\sum_{n=1}^{N}\int_{\theta-\varepsilon}^{\theta+\varepsilon} V^*\big(\ell\cos\theta,\ell\sin\theta,\theta,nt_p+T_m\big)\ell\,d\theta\ . \qquad (3.15)$$

where $t_p$ denotes the period of the eclipse cycle; n is twice the number of orbital rotations, and N represents the total number of eclipses. The timing $T_m$ refers to the intervals for each phase number $m$, which are detailed as :

$$T_m = m\big(t_p/8\big). \qquad (3.16)$$

The process described by eq.(3.15), defined as "data stacking for the LV," involves averaging EHT data sampled in synchrony with the eclipse cycle period, which is half of the determined orbiting period of ECB-SMBH. For additional context regarding sampling, the symmetrically assumed BH positions are determined by dividing the eclipse cycle period into eight intervals $T_m$, as illustrated in Panel B of Figure 4. In the context of observation, we cannot directly manage the phase numbering m depicted in the diagram due to the absence of precise phase information for the orbiting ECB-SMBH. Therefore, we employ two methods of phase numbering: the absolute phase numbering $m_a$, used for theoretical calculations where we can determine the phase of the ECB-SMBH's orbital motion, and the relative phase numbering $m_r$ (primarily for observation data).

An example of data sampling with respect to the 96 CASA AZ-JC baseline of EHT data, as part of the preparation for forming the LV, is presented in Figure 5. Here, the entire observation interval is divided into five time segments, with original EHT visibilities split into five groups along with their corresponding u-v values. In each time segment, we have multiple data points across the eight phase bins $m_r$, allowing us to average (data stack) EHT visibilities along with u-v values. Subsection 3.3 showcases the example results of data stacking prepared for the formation of the LV for the current case of EHT data from the 96 CASA AZ-JC baseline. The findings, as demonstrated in Figure 6, reveal that the averaged baselines (u, v) remain consistent across all phase bins within a given time segment, yet visibilities vary significantly depending on the chosen phase bins. The level of visibility variation significantly exceeds the associated standard deviation σ, suggesting the presence of periodic variation in the visibilities.

### 3.3 Results of Synchronized data Stacking of Linearized Visibility

#### 3.3.1 Formation Processes of LV from EHT Visibility Data

Following the processes described in Subsection 3.1.2, we formed the LV from the EHT data of SgrA* observed on April 6, 2017 [30], which consists of 21 sets of baseline observed at high frequencies (229.1 GHz) and low frequencies (227.1 GHz), calibrated and correlated in both CASA and HOPS data handling pipelines [30]. The original EHT data from April 7, 2017, subsequently provided four data groups for each observation day. However, as will be explained in Subsection 3.4, it becomes apparent that the data from April 7 are inadequate for the present LV method. Therefore, we selected two data sets, 96 (April 6) Hi CASA and 96 Lo HOPS, from the EHT data to form the LV corresponding to the eight phases, seeking.

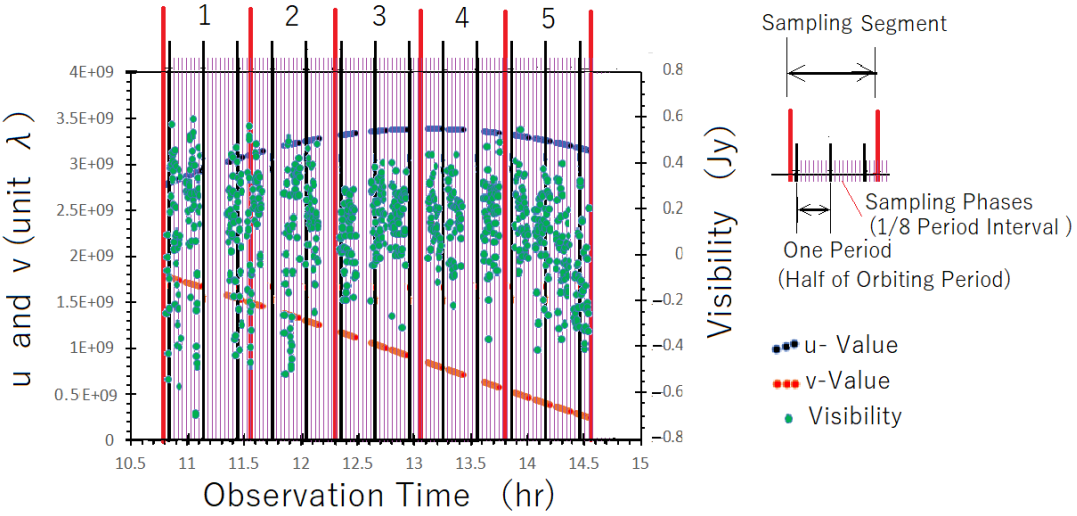


**Figure 5.** An example of "data stacking to form the LV" with respective to 96 CASA AZ-JC baseline observations of EHT data. The whole observation interval is divided into 5 time segments where original visibilities are divided into 5 groups together with corresponding u-v values. The sampled EHT data are averaged to eight sets of u-v values in each segment; i.e., for a given baseline of EHT data , we have 5 sets of linearized visibilities with corresponding eight $m_r$ phases.

the ECB-SMBH orbiting motion with an eclipse period (half of the orbiting period).

For the 96 (April 6) Hi CASA data set, observation times and data statistics with respect to the processes outlined in Subsections 3.1 and 3.2 for data stacking for the LV are presented in Table 3. Here, 21 baseline data consisting of Sgr A* observations at six observation stations (see Appendix B for information provided by EHTC) are utilized. Although start times at each observation baseline are not the same, we established a common sequence to synchronize with the orbital period of ECB-SMBH throughout all baseline data. For this purpose, we carefully set the time difference (TD), both in terms of real time and sequence numbers of the orbital rotation (Peri N.). The stacking numbers in Table 3, defined as the number of visibility data distributed into all eight phase bins (from 1 to 8 of $m_r$, see Subsection 3.2), are noted. When the stacking number is 20, as in the case of the baseline AA-SP in Table 3, there are four rounds of distributions of EHT visibility data for all eight phase bins throughout the entire observation interval of 10.3666 h; that is, because observation intervals are divided into five time segments, we observe four rounds of data distribution for each phase bin, allowing us to trace the orbital motion in each time segment. This means that the level of observed visibilities is averaged over four data points, reducing the sigma associated with the data by half.

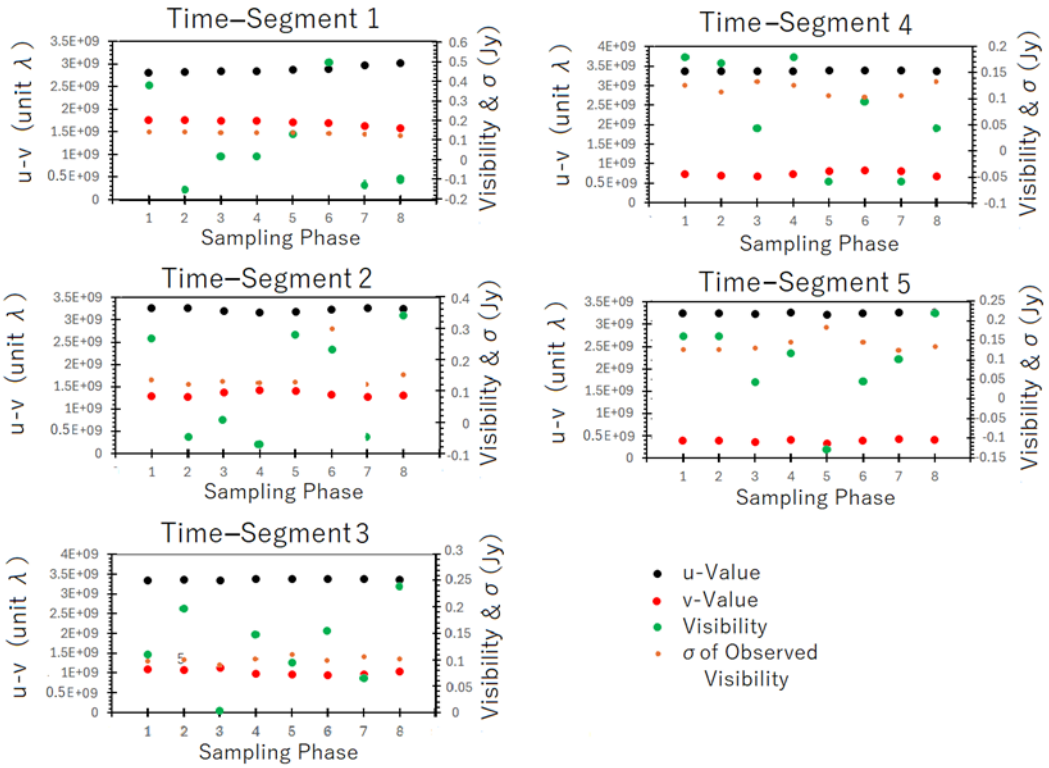


**Figure 6.** Example results of the data stacking prepared for the formation of the LV for the case of the EHT data of 96 CASA AZ-JC. The baseline length components u (black spot) and v (red spot) are given with scale in left ordinate; the visibilities (green spot) and associated σ (small orange spot) are given with scale in the right ordinate. The baselines (u, v) averaged in each corresponding phase bin are almost same for all phase bins in a given time-segment but visibilities vary clearly depending on the selected phase bins. The variation levels of the visibilities apparently overcome the associated σ suggesting the existence of the periodic variation of the visibilities.

### 3.3.2 Formation of LV from Stacking Visibilities

In the process of forming the LV, we transform the stacked baseline data in the (u, v) coordinate to the baseline values in $(\ell, \tilde{t}$ coordinate (see eqs.(3.10-1) and (3.10-2)) for the u-v values of the eight sets in the corresponding phase $m_r$ of the given time segments. As a final step, we form the LV by checking the associated $\tilde{t}$ (given by eq.(3.10-2)) considering the criteria that

$$|\ell| > 0.8|\,\tilde{t}|. \qquad (3.17)$$

This criterion corresponds to 0.21 rad as ε in eq.(3.16); the data within a fan-shaped area with an angle range of ± 39° deviating from the selected line are then considered as objective

| Baseline | Start Time | End Time | T.D. (h) | Obs. Int. (h) | T.D. (Peri. N.) | Stacking |
|---|---|---|---|---|---|---|
| AA-SP | 8.4013 | 14.5486 | 0 | 6.1472 | 0 | 20 |
| AA-AP | 8.4013 | 14.5486 | 0 | 6.1472 | 0 | 20 |
| AP-SP | 8.4013 | 14.5486 | 0 | 6.1472 | 0 | 20 |
| AZ-SP | 8.9013 | 14.5486 | 0.5 | 5.6472 | 1 | 20 |
| LM-SP | 8.9013 | 14.5486 | 0.5 | 5.6472 | 1 | 18 |
| AA-AZ | 8.9041 | 14.5486 | 0.5027 | 5.6445 | 1 | 18 |
| AA-LM | 8.9013 | 14.5458 | 0.5 | 5.6444 | 1 | 18 |
| AZ-LM | 8.9041 | 14.5486 | 0.5027 | 5.6445 | 1 | 18 |
| AP-AZ | 9.8402 | 14.5486 | 1.4388 | 4.7084 | 4 | 18 |
| AP-LM | 9.8402 | 14.5458 | 1.4388 | 4.7056 | 4 | 15 |
| JC-LM | 10.8013 | 14.5486 | 2.3999 | 3.7473 | 8 | 15 |
| AA-JC | 10.8013 | 14.5513 | 2.3999 | 3.75 | 8 | 12 |
| AP-JC | 10.8013 | 14.5486 | 2.3999 | 3.7473 | 8 | 12 |
| AZ-JC | 10.8013 | 14.5513 | 2.3999 | 3.75 | 8 | 12 |
| JC-SP | 10.8013 | 14.5486 | 2.3999 | 3.7473 | 8 | 12 |
| AA-SM | 11.5374 | 14.543 | 3.136 | 3.0055 | 10 | 12 |
| AZ-SM | 11.5374 | 14.5486 | 3.136 | 3.0112 | 10 | 10 |
| JC-SM | 11.5347 | 14.5486 | 3.1334 | 3.0138 | 10 | 10 |
| LM-SM | 11.8847 | 14.5486 | 3.4833 | 2.6639 | 11 | 10 |
| AP-SM | 11.5347 | 14.5486 | 3.1334 | 3.0138 | 10 | 8 |
| SM-SP | 11.5347 | 14.5486 | 3.1334 | 3.0138 | 10 | 10 |

T.D. (h) : Start Time difference from 8.4013 hour

T.D. (Peri. N.) : T.D. in term of period number

Obs. Int. (h) : Observation interval (hour)

Stacking N. : Total stacking number

**Table 3. List of VLBI baselines of EHT data, observation times and data stacking number for 96 (April 6, 2017) EHT data. (Baseline information is given in Appendix B).**

data for LV (see Figure 7). For the level of LVs, we set thresholds with sigmas; however, due to stacking effects on EHT data, where the resulting LVs are formed by averaging multiple numbers of EHT data, as described in Subsection 3.3.1, most levels of LV clear the threshold level with cases higher than 2 σ.

### 3.4 Possibilities of LV Formation for 96 Hi CASA and 97 Hi CASA

Results of the stacking visibility data synchronized with the eclipse cycle period of orbiting ECB-SMBH for the EHT visibility data of 96-Hi CASA are given in Figure 8, where the baseline coordinate is transformed from the u-v system to $\ell$-$\tilde{t}$ system. From the displayed data, the LVs are formed by taking the visibility data within the colored fan-shaped region as visibility to be the function of $\ell$ that satisfies the condition given by eq.(3.17). The data are displayed for the $m_r$ phases 1, 3, 5, and 7, where from seven to ten data points form effective

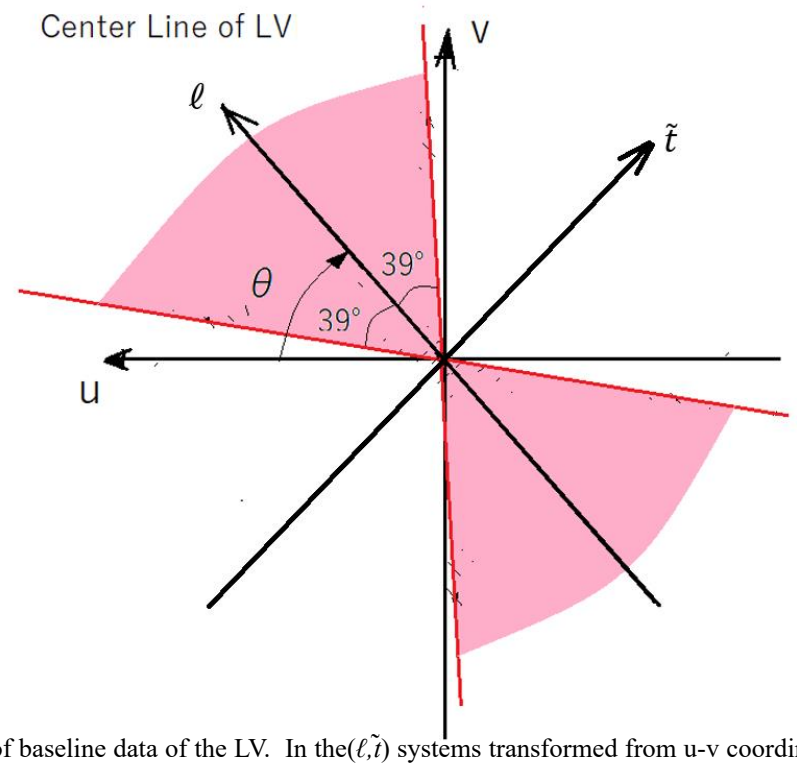


**Figure 7.** Selecting range of baseline data of the LV. In the($\ell$,$\tilde{t}$) systems transformed from u-v coordinate, the data deviating ±39° from $\ell$ line is selected as LV.

LVs in the range $\ell > 2.5\times 10^9\ \lambda$. In Figure 9, results of the stacking visibility data synchronized to the eclipse cycle period of orbiting ECB-SMBH for the EHT visibility data of 97-Hi CASA are indicated. Because there is only one or two data points contributing to effective LVs in the range $\ell > 2.5\times 10^9\ \lambda$, it is disclosed that applying the present LV concept for the 97-Hi CASA case is inadequate.

### 3.5 Results of LVs Corresponding to 96 Hi CASA and 96 Lo HOPS Data

#### 3.5.1 Real Part of LV

One of the most critical and difficult steps in visualizing the moving ECB-SMBH is to find an exactly accurate orbiting period. In this context, we have already attempted to find the orbital period after the initial proposal of 2200±50 s based on the decameter radio wave pulses from SgrA* [14]. As the first step to confirm the proposed existence of ECB-SMBH at Sgr A*, we investigated the results of 1.3 mm wavelength VLBI observations carried out by Fish et al. [27], which give orbital periods of 2150±2.5 s.

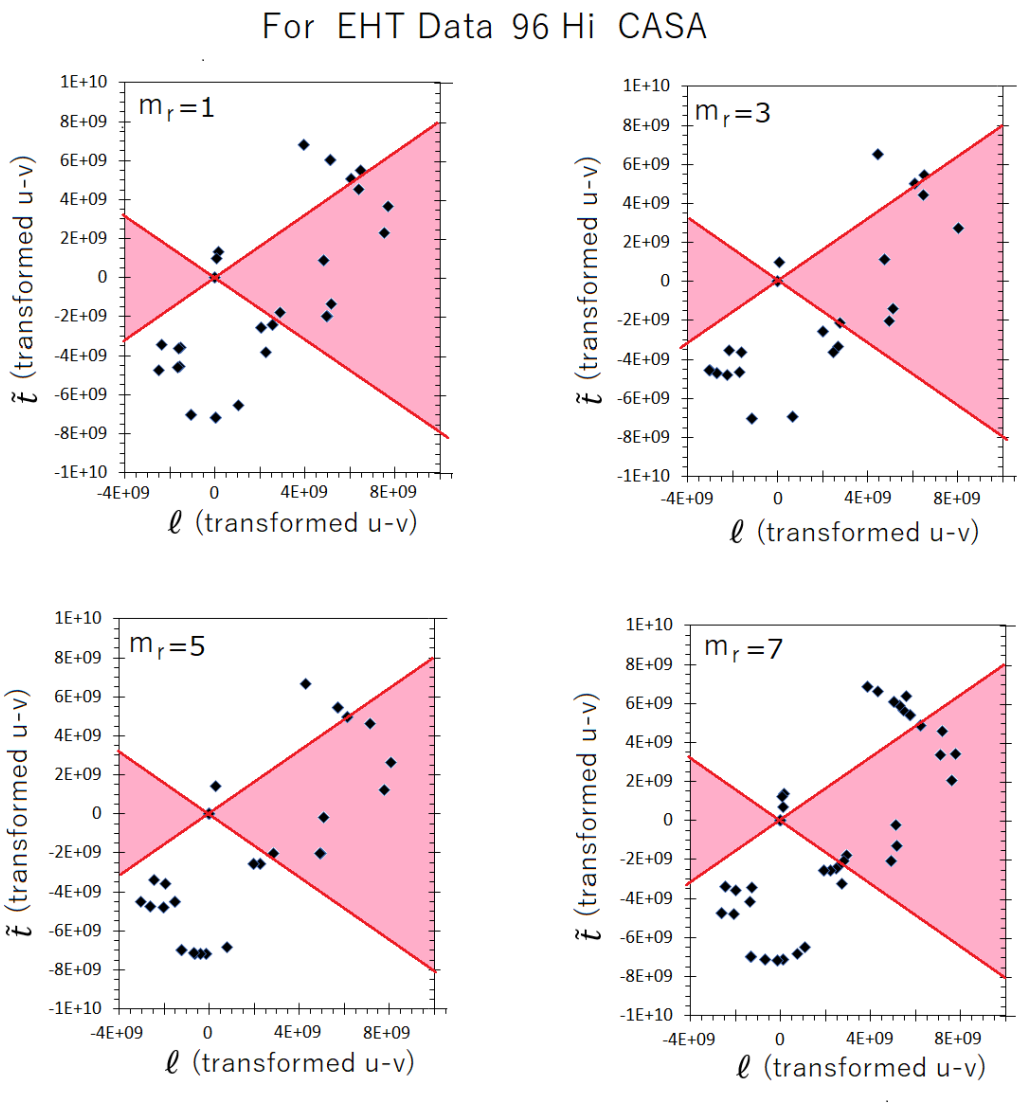


**Figure 8.** Results of baseline coordinate transformation from u-v system to $\ell$ -$\tilde{t}$ system for the EHT-data of ECB-SMBH orbiting period synchronized with stacking processes. The LVs are formed taking the visibility data within the colored fan shape region as visibility to be the function of $\ell$ approximately. The data are displayed for the $m_r$ phases 1, 3, 5 and 7. There are 7 ~10 data which form effective LVs in the range $\ell$>2.5× $10^9$ λ.

The second step of confirmation was carried out [29] using publicly released EHT data, [30] as the results are reproduced in Table 2, where the orbiting periods are given in the range from 2140 s to 2235 s for 24 cases of the EHT-VLBI data, giving an average of 2193.3 s with a standard deviation of 27.5 s. Considering the period ranges revealed by these cases, we have tried to search for the real orbital period of ECB-SMBH at 2143, 2153, 2163, 2173, 2183, 2193, 2203, 2213, 2223, and 2233 s. The adequate orbit period is judged by how the formed LV under the given period reveals reasonable variation compared with the theoretically calculated LV sequence based on the ECB-SMBH orbital motion. In the present work, we find by trial to the two data sets, 96 Hi CASA and 96 Lo HOPS, that the adequate orbiting period is close to 2153±5 s. For this point, we will describe the details in Section 4.

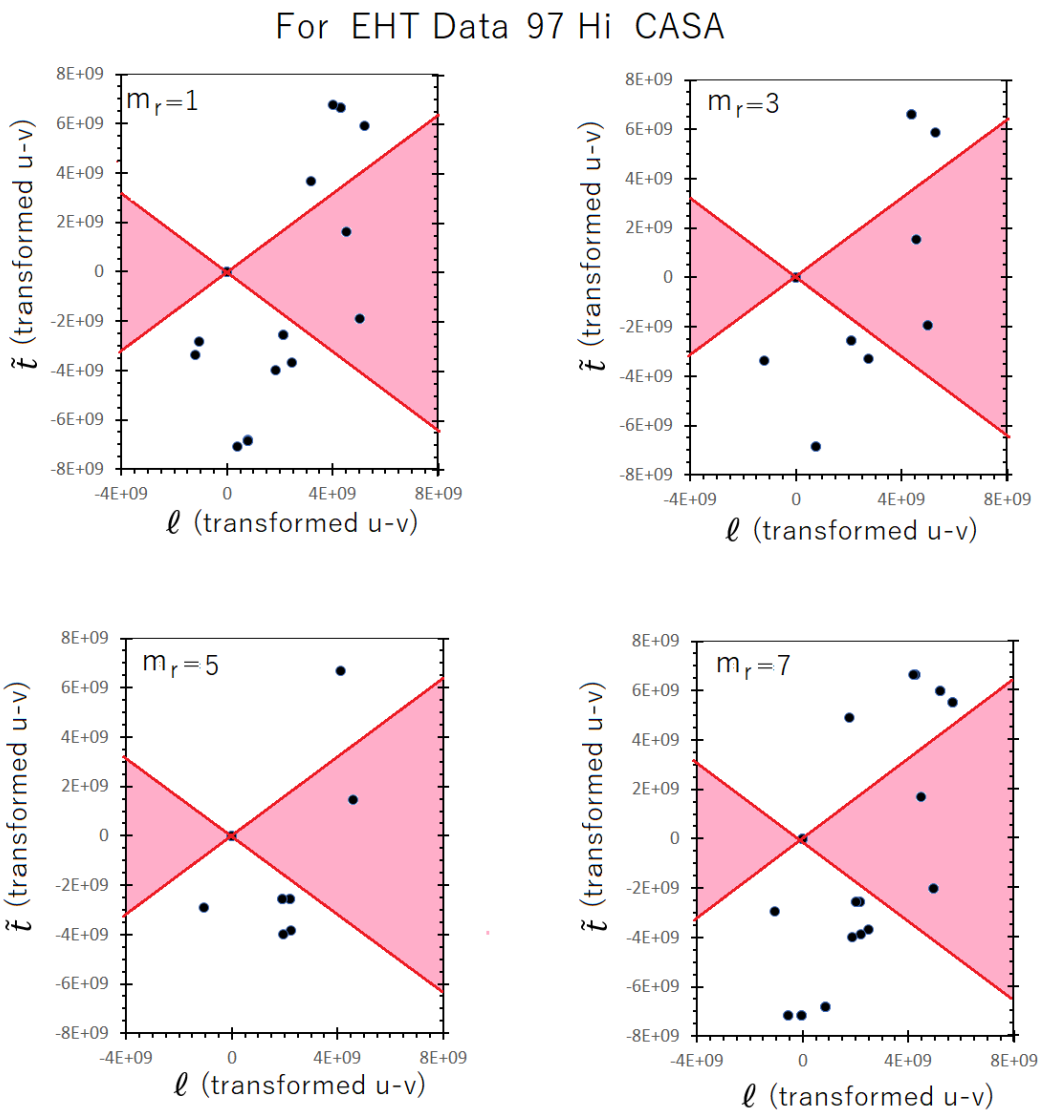


**Figure 9.** same with Figure 8. for the case of EHT data of 97 Hi CASA. There are only 1~2 data which contribute to effective LV's in the range $\ell > 2.5\times 10^9\ \lambda$; it is disclosed that to apply the present LV concept for this case is inadequate.

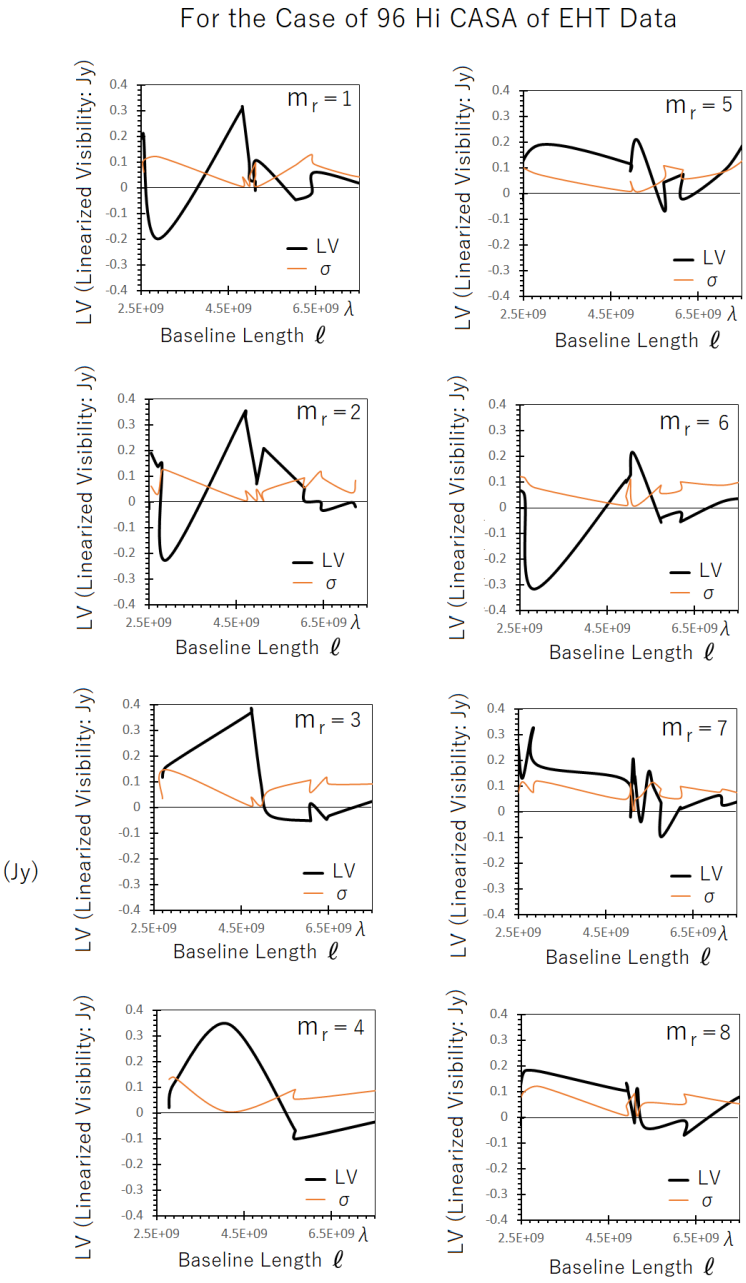


**Figure 10.** Results of real part of LV formed with the EHT, 96-Hi CASA visibility data being displayed with relative sequence number $m_r$ corresponding to eclipse cycle period of 2153/2 sec. The LV is given as the function of baseline length ℓ that is set in parallel to the orbital plane of ECB-SMBH transformed from the regular u-v baseline coordinate. The LV shows sensitive response in the ℓ range from 2.5× $10^9$ λ to 5.5× $10^9$ λ , with condition of |LV|>σ , in each panel corresponding the phase of the orbital motion of the ECB-SMBH with orbit size of 33μas.

In Figure 10, the results for the real part of LV formed with the EHT 96-Hi CASA visibility data are displayed sequentially with the relative phase number $m_r$. The LVs are presented as a function of the baseline length ℓ, which is aligned parallel to the orbital plane of ECB-SMBH as defined by eq.(3.9-1), with respect to the regular u-v baseline coordinate. It is observed that the LVs show a sensitive response in the ℓ range from 2.5×$10^9$ λ to 5.5×$10^9$ λ, where it is confirmed that $|LV|>\sigma$, in each panel corresponding to the phase of the orbital motion of ECB-SMBH. For baseline lengths longer than 5.5×$10^9$ λ, LV values significantly decrease, showing the condition $|LV|\leq\sigma$; this evidence indicates that the obtained LVs accurately reflect the motion effects of the ECB-SMBH, whose orbit size reveals 33 μas. As previously described in Section 2, the orbit size of ECB-SMBH from the study on the decameter radio wave pulse observation of SgrA* is 4.1×$10^7$ km [14], which provides an observing angle of 33μas for the distance of 8.3 kpc from SgrA*. The $LV_{ij}$ (linearized visibility defined between the i and j stations of VLBI) can be approximated as follows (see Appendix C):

$$LV_{ij} = W_{ij}cos\left(\frac{2\pi}{\lambda}sin\Theta_0 \cdot \ell_{ij}\Delta\Theta\right), \qquad (3.18)$$

where $W_{ij}$, $\ell_{ij}$, and $\Theta_0$ are the visibility amplitude, the baseline length between the i and j stations of VLBI, and the angle between the arrival direction of the radio wave and baseline direction, respectively; $\Delta\Theta$ represents the angle width of the observing object. The baseline range from $2.5\times10^9$ λ to $5.5\times10^9$ λ, provides a stable visibility angle range from 2.51 to 5.52 rad. Details confirming the existence of the binary motions of ECB-SMBH will be given in the next Section 4 with the case of LV deduced from the EHT 96 Lo HOPS data.

### 3.5.2 Imaginary Part of LV

In Figure 11, the results for the imaginary part of the LV, based on the EHT 96 Hi CASA data, are displayed as a function of the relative phase number $m_r$ corresponding to the orbiting periods of 2153 s (1076.5 s eclipse cycle period). When considering the case of negative σ, $|LV|\leq|\sigma|$ in almost the entire range of ℓ; this indicates that there are no significant LVs in the imaginary part of the linearized visibility. This is also evident in the case of negative values of ℓ as presented in Table 4, where the imaginary part of LVs is shown as a function of the data-stacked phases, which are relatively set by dividing the eclipse cycle period of ECB-SMBH into eight intervals, similar to the formation of the real part of LV. Compared with the magnitude of the real part, whose absolute values are always above 0.1 Jy, it is concluded that there are no significant values in the imaginary part, even in the case of negative ℓ.

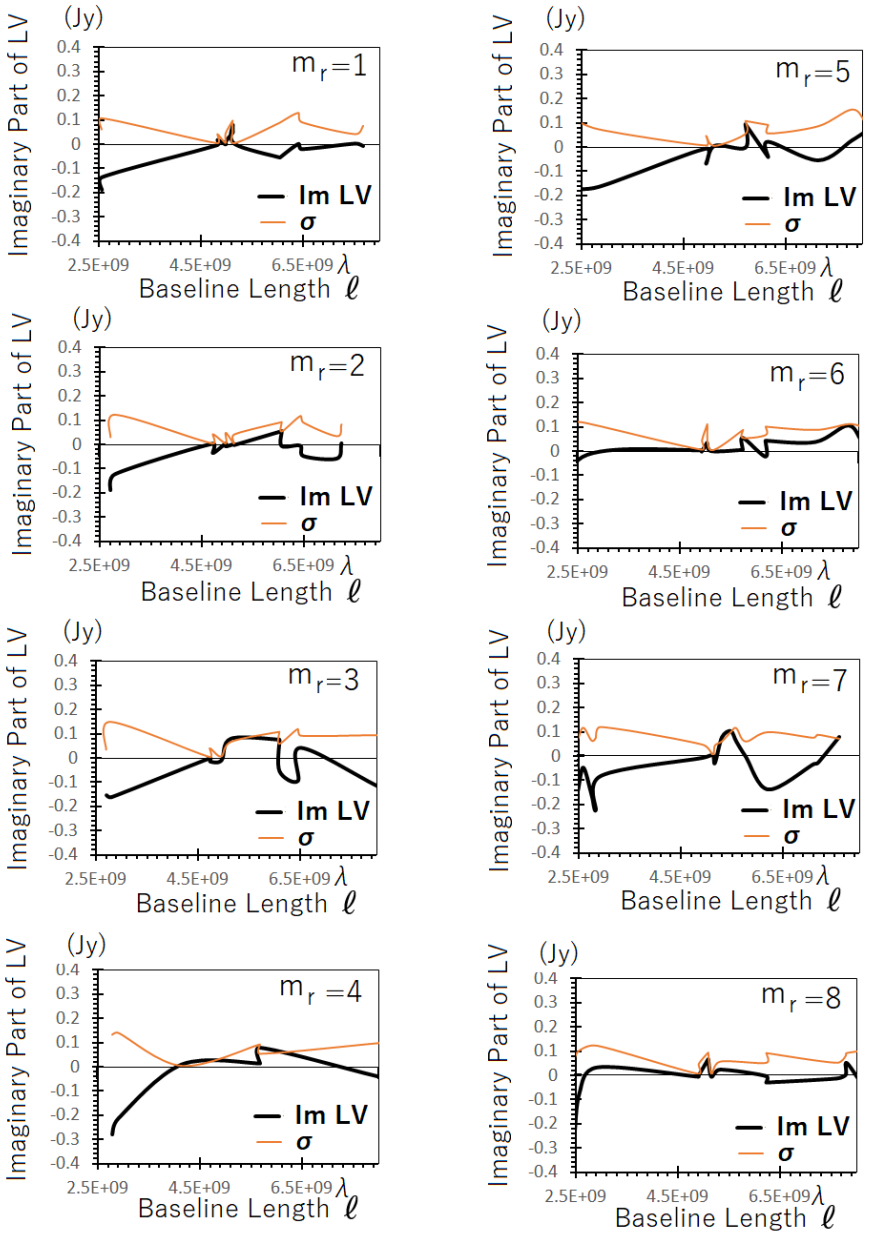


**Figure 11.** Results of the imaginary part of the LV based on the EHT, 96 Hi CASA VLBI data displayed as function of the relative phase number $m_r$ corresponding to the orbiting periods 2153 sec (1076.5 sec eclipse cycle period). In almost all range of ℓ, $|LV|\leq|\sigma|$ (considering minus case of σ together) suggesting that there are no significant LV in the imaginary part of the linearized visibility.

Part 1

| Relative Phase No. | | | | | | | | | | | | |
|---|---|---|---|---|---|---|---|---|---|---|---|---|
| 1 | | | 2 | | | 3 | | | 4 | | | |
| $\ell$ | Im-LV | $\sigma$ | $\ell$ | Im-LV | $\sigma$ | $\ell$ | Im-LV | $\sigma$ | $\ell$ | Im-LV | $\sigma$ | |
| -5.E+04 | 0 | 0.079 | -1.8E+06 | -0.03 | 0.003 | -1.7E+06 | 0.024 | 0.003 | -4.7E+04 | 0 | 0.073 | |
| -1.7E+06 | 0.01 | 0.003 | -1.9E+06 | 0.033 | 0.004 | | | | -4.7E+04 | 0 | 0.072 | |
| | | | | | | | | | -6.0E+04 | 0 | 0.096 | |
| | | | | | | | | | -1.9E+06 | -0.01 | 0.004 | |

Part 2

| Relative Phase No. | | | | | | | | | | | | |
|---|---|---|---|---|---|---|---|---|---|---|---|---|
| 5 | | | 6 | | | 7 | | | 8 | | | |
| $\ell$ | Im-LV | $\sigma$ | $\ell$ | Im-LV | $\sigma$ | $\ell$ | Im-LV | $\sigma$ | $\ell$ | Im-LV | $\sigma$ | |
| -4.7E+04 | 0 | 0.073 | -4.7E+04 | 0 | 0.069 | -4.6E+04 | 0 | 0.073 | -5.0E+04 | 0 | 0.078 | |
| -6.0E+04 | 0 | 0.098 | -5.9E+04 | 0 | 0.093 | -5.0E+04 | 0 | 0.082 | -1.9E+06 | 0.032 | 0.004 | |
| -1.9E+06 | 0.001 | 0.004 | -1.9E+06 | -0.006 | 0.004 | -5.9E+04 | 0 | 0.089 | -2.8E+09 | -0 | 0.007 | |
| -1.9E+06 | 0.019 | 0.003 | -2.8E+09 | 0.003 | 0.01 | -1.9E+06 | 0.006 | 0.003 | -1.9E+06 | 0.054 | 0.004 | |
| -1.9E+06 | -0.02 | 0.005 | | | | -1.9E+06 | -0.02 | 0.005 | -2.8E+09 | -0.01 | 0.007 | |

**Table 4. Imaginary part of LV in negative ℓ range.**

## 4. Confirmation of Existence of Binary Motions of ECB-SMBH

### 4.1 Theoretical Base-Fourier transformation of ECB-SMBH versus moving positions

We are at the stage of the work where we decipher the binary motion of ECB-SMBH from the analyzed LV. For this purpose, we first calculate the Fourier transformation of the moving ECB -SMBH for each corresponding phase of the orbiting motion to confirm its coincidence with the observed LV. Considering the relations from eqs.(3.10) to (3.14), given in Subsection 3.1.2, we can describe the radio wave source function $S(P,\theta_0,T_m)$ at selected timing $T_m$ as follows:

$$S(p,\theta_0,T_m)=\int V_L(\ell,\theta_0,T_m)\cdot exp(i\ell \mathrm{p})d\ell\ . \qquad (4.1)$$

In the present work, we adopt the approach of confirming the LV, $V_L(\ell,\theta_0,T_m)$ from the expected S$(p,\theta_0,T_m)$ function by taking the inverse Fourier transformation corresponding to eq.(4.1); i.e.,

$$V_L(\ell,\theta_0,T_m)=\frac{1}{2\pi}\int_{-\infty}^{\infty}S(p,\theta_0,T_m)\cdot exp(-\mathrm{i}\ell \mathrm{p})d\mathrm{p}\ . \qquad (4.2)$$

Based on a previous study ,[29], we consider the configuration of ECB-SMBH orbits in the plane approximately parallel to the Galactic equator, which are observed from the observation stations as linear back and forth motions along the line inclined by $\theta_0$ with respect to the direction of right ascension (see Figure 12). The moving center position of BHs is given by distance $a$ (×10$\mu as$) from the center of SgrA* along $p$(L); each BH is associated with a radio wave emission zone with an approximated radius of b(×10 $\mu as$).

For the configuration and motion of ECB-SMBH depicted in Figure 12, we calculate the LV, following eq.(4.2), as follows:

$$V_L(\ell,\theta_0,T_m)=\frac{1}{2\pi}\left[\int_{a-b}^{a+b}\mathrm{A}(p-a)\cdot\cos\left[\frac{\pi(p-a)}{2b}\right]\cdot exp(-\mathrm{i}\ell p)dp + \int_{-a-b}^{-a+b}\mathrm{A}(p+a)\cdot\cos\left[\frac{\pi(p+a)}{2b}\right]\cdot exp(-\mathrm{i}\ell p)dp\right]. \qquad (4.3)$$

where

$$\mathrm{A}(p\pm a)=\begin{cases} A_0:\ Const & for\ |p\pm a|<b \\ 0 & for\ |p\pm a|\geq b \end{cases}$$

In eq.(4.3), $A_0 cos[\pi(p-a)/2b]$ and $A_0\cdot cos[\pi(p+a)/2b]$ are models to express emission levels of the radio wave emitting zone around ECB-SMBH with an arbitrary constant $A_0$; we model the emission as part of a cosine function, which shows a maximum at the center part and fades to zero at the radius b of the observing disk of ECB-SMBH.

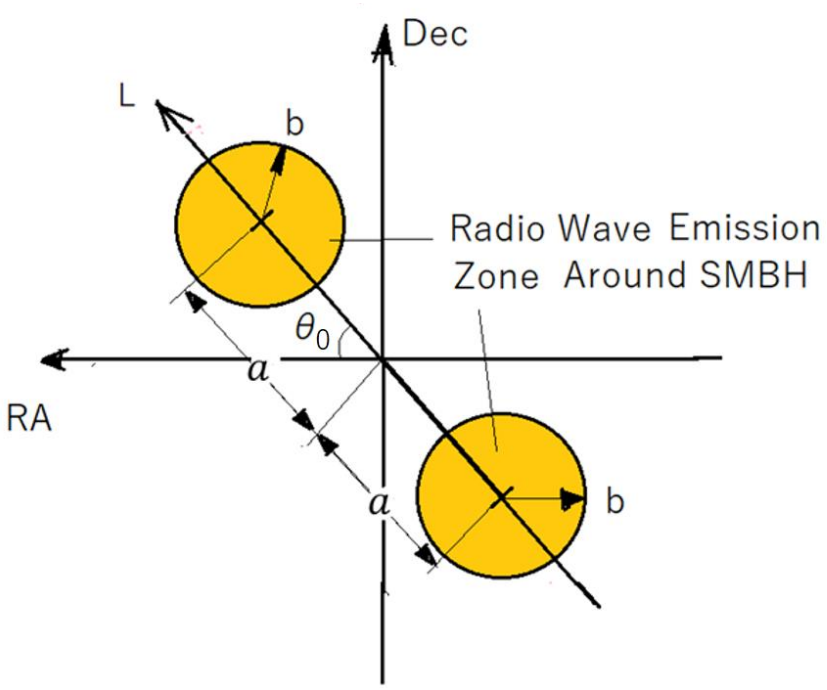


**Figure 12.** Configuration of moving ECB-SMBH. The binary motions orbiting in the plane approximately parallel to the Galactic equator are observed from the observation station as linear motion along the line inclined by $\theta_0$ with respective to the direction of the right ascension. The center position of BHs are given by distance $a(\times 10\mu as)$ from the center of SgrA* along p; each BH are associated with radio wave emission zone with approximated radius b ($\times 10\mu as$).

a) Real part of LV
The equation eq.(4.3) is then rewritten for the real part as,

$$V_{Re}(\ell,\theta_0,T_m) = \frac{1}{2\pi}\left[\int_{a-b}^{a+b} A_0 \cdot \cos\left[\frac{\pi(p-a)}{2b}\right]\cdot cos(-\ell p)dp + \int_{-a-b}^{-a+b} A_0 \cdot \cos\left[\frac{\pi(p+a)}{2b}\right]\cdot cos(-\ell p)dp\right] \quad . (4.4)$$

As detailed in **Appendix D**, $V_{Re}(\ell,\theta_0,T_m)$ can be given by,

$$V_{Re}(\ell,\theta_0,T_m) = \frac{A_0/b}{(\pi/2b)^2-\ell^2}\cdot cos(a\ell)\cdot cos(\mathrm{b}\ell). \qquad (4.5)$$

b) Imaginary part
Corresponding to eq.(4.3), the imaginary part of LV, $V_{Im}(\ell,\theta_0,T_m)$ is expressed by:

$$V_{Im}(\ell,\theta_0,T_m) = \frac{1}{2\pi}\left[\int_{a-b}^{a+b} A_0 \cdot \cos\left[\frac{\pi(p-a)}{2b}\right]\cdot sin(-\ell p)dp + \int_{-a-b}^{-a+b} A_0 \cdot \cos\left[\frac{\pi(p+a)}{2b}\right]\cdot sin(-\ell p)dp\right]. \qquad (4.6)$$

Taking the argument $p$ in the above eq.(4.6) as the integration parametric argument, we can rewrite the second integration on the right hand side, by changing $p=-p$ ,as,

$$V_{Im}(\ell, \theta_0, T_m)$$
$$= \frac{1}{2\pi}\left[\int_{a-b}^{a+b} A_0 \cdot \cos\left[\frac{\pi(p-a)}{2b}\right] \cdot sin(-\ell p)dp + \int_{a+b}^{a-b} A_0 \cdot \cos\left[\frac{\pi(p-a)}{2b}\right] \cdot sin(-\ell p)dp\right]. \quad (4.7)$$

Then it is concluded that:

$$V_{Im}(\ell, \theta_0, T_m) = 0. \quad (4.8)$$

### 4.2 Comparison of Fourier Transformation of Binary Motions with LV Based on EHT Observation Data

#### 4.2.1 Preparations for matching of conditions between theoretical and observational LV

**a) b Value Dependence**

In Figure 13, the calculated results of the Fourier transformation, following eq.(4.5), are displayed, taking positions $a$ of the moving ECB-SMBH along the linearly observable orbit as a parameter at position $m$; *i.e.*,$a$= $a_m$. Thus, the visibility levels (LV) in relative units are plotted against the transformed baseline ℓ for 17 positions ($a_m$) of ECB-SMBH, with the parameter $a_m$(×10 $\mu as$). The parameter b, expressing the radius of emission zones surrounding ECB-SMBH, significantly influences the appearance of the ℓ range through eq.(4.5). When compared with the LV formed from the EHT observation data of 95 Hi CASA, as shown in Figure 10, the feature of ℓ dependence of the visibility, which exhibits a clear decrease at 5.5×10$^9\lambda$, suggests that the possible limit of the expansion of the radio wave emission zone surrounding ECB-SMBH is approximately 8 $\mu as$. Then, from the perspective of searching for the positions of the moving BHs, the size of the radio emission zone surrounding the BHs is treated as a variable parameter. After exploring the possible range for the b(×10 $\mu as$) value, we selected two values; one case features a narrow zone with b=0.4 (4 $\mu as$), where the radius of the emission zone covers only approximately 1.5 times the radius of the event horizon of the maximally rotating Kerr BH. The other case features a wide zone with b=0.8, where the radius of the emission zone covers approximately three times the event horizon radius of the maximally rotating Kerr BH; for this case of a relatively wide emission zone, the calculated ℓ range of $V_{Re}(\ell,\theta_0,T_m)$ is confined from 2.5×10$^9\lambda$ to 5.5×10$^9\lambda$, which closely matches the observed LV, endorsing the certain existence of the ECB-SMBH (see Subsection 3.4).

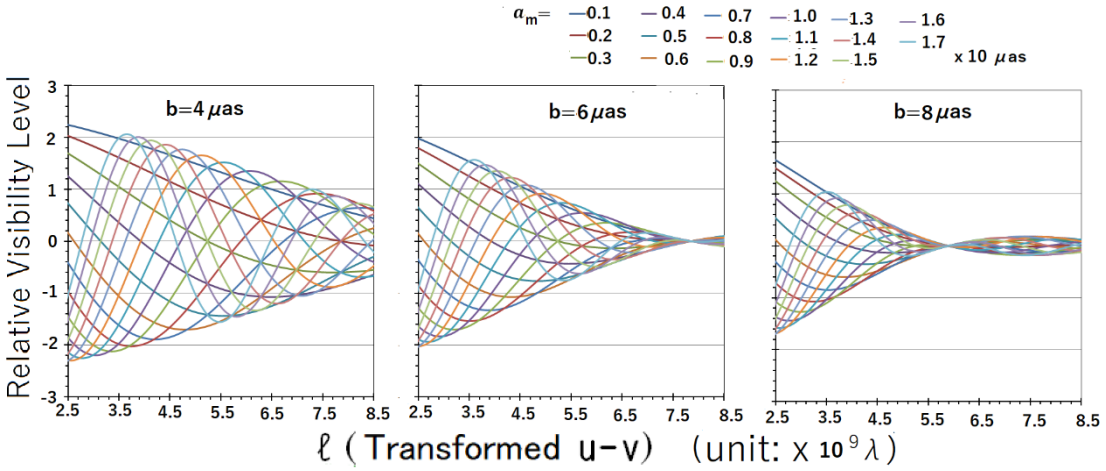


**Figure 13.** Theoretical results of the real part of the LV corresponding to eq.(4.5) for three cases of b values. Results are indicated as relative value of the visibility amplitude versus the linear baseline ℓwhich gives length of 10$^9$λunit corresponding to the distance 2$a$ of the ECB-SMBH where $a$ is given with corresponding colors ; $a$ is read with unit ×10 $\mu as$. Compared with LV formed from the EHT observation data of 95 Hi CASA as given in Figure 10, the feature of the ℓ dependence of the visibility which show clear diminishing at 5.5×10$^9\lambda$ suggests that the possible limit of the expansion of the radio wave emission zone surrounding ECB-SMBH is about 8 $\mu as$ .

In the ℓ range higher than 5.5E9λ, corresponding to a source size of less than approximately 10 $\mu as$ ( see Subsection 3.6), all LV values fall below the σ values. Therefore, in this range, we cannot discern any meaningful structure from the resulting LV; this may be consistent with the resolution limit of EHT VLBI data for sizes smaller than 10 $\mu as$.

**b). Selection of Amplitude and Bias Values**

The theoretical result expressed by eq.(4.5) focuses simply on the position of two radio sources whose emission intensity is modeled by a partial cosine function with a maximum point at the center of the binary objects. However, real data represent non-stationary objects associated with various origins of emissions

and a variety of background radio wave brightness. These factors contribute to the deviation from theoretical LV (T-LV) and EHT data-based observed LV (E-LV). Under these circumstances, we are permitted to adjust linear coefficients to align the T-LV with the E-LV; these adjustments involve amplitude and bias values. That is; to bridge the gap between the T-LV and E-LV, we can adjust the amplitude by selecting the $A_0$ value in eq.(4.5), while a new constant term —Bias. must be added to eq.(4.5) to account for background emissions.

Adding the new term "Bias" to eq.(4.5) introduces significant physical meaning to the equation. Since eq.(4.5) is the Fourier-transformed equation of the source distribution representing the central part of SgrA*, adding a constant to LV equates to incorporating white noise, in real space, composed of random noises without a spectrum peak.

**c). Selection of Eight Phases for T-LV to Coincide With E-LV**

For the comparison of Fourier-transformed T-LV with the E-LV, we need to align the timing of T-LV, for the orbiting ECB-SMBH, with the timing of E-LV. In the present algorithm, the selection of timing $t_m$ (m=1 to 8) to form T-LV is set by choosing the ECB-SMBH distance, $a_m(\times 10\ \mu as)$, as follows:

$$a_m = 1.65 \cdot cos\left[\Omega_{eq}(t_m - t_s)\right]. \qquad (4.9)$$

where $\Omega_{eq}$ is the angular frequency of the orbiting ECB SMBH in terms of the eclipse cycle, given by $\Omega_{eq}=2\pi/T_{eq}$ with $T_{eq}=2153/2\ s$ (for the presently selected eclipse cycle period); $t_s$ is the adjusting time to synchronize T-LV with E-LV. If we select $t_s=0$, the phase selection of T-LV is made by the absolute number $m_a$ (see Subsection 3.2), while E-LV is expressed by the relative number $m_r$. To reduce the difference between T-LV and E-LV, it is important to find a suitable $t_s$ for calculating T-LV.

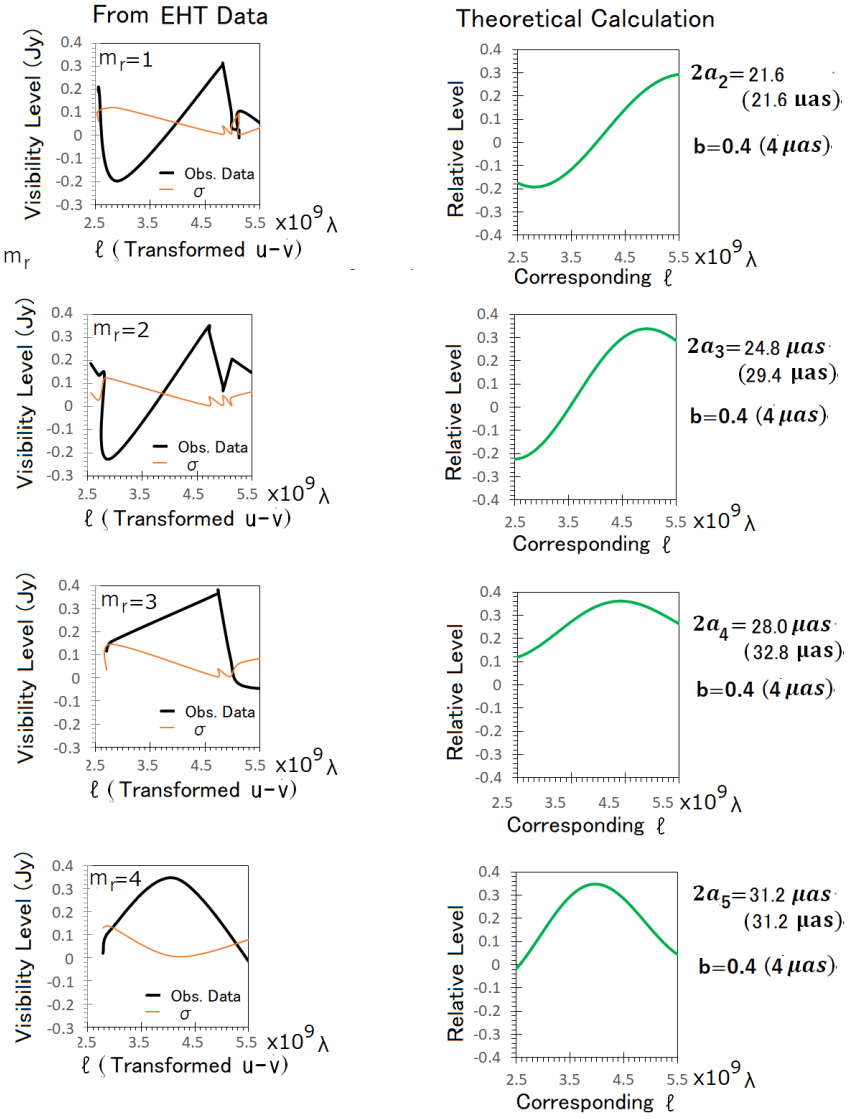


**Figure 14** (A). Results of theoretical linearized visibility (T-LV: green curves in the right collum for b=0.4) and linearized visibility formed from the EHT 96 Hi CASA visibility data (E-LV: black curves in the left collum). For the E-LV given sequentially with relative phase number $m_r$, the corresponding T-LVs are indicated being adjusted the amplitude and the bias level to meet with E-LV. The parameter $a_{m_a}$ in the T-LV column shows $a$ value in eq.(4.5); $2a_{m_a}$shows observing distance between two BHs of ECB-SMBH.

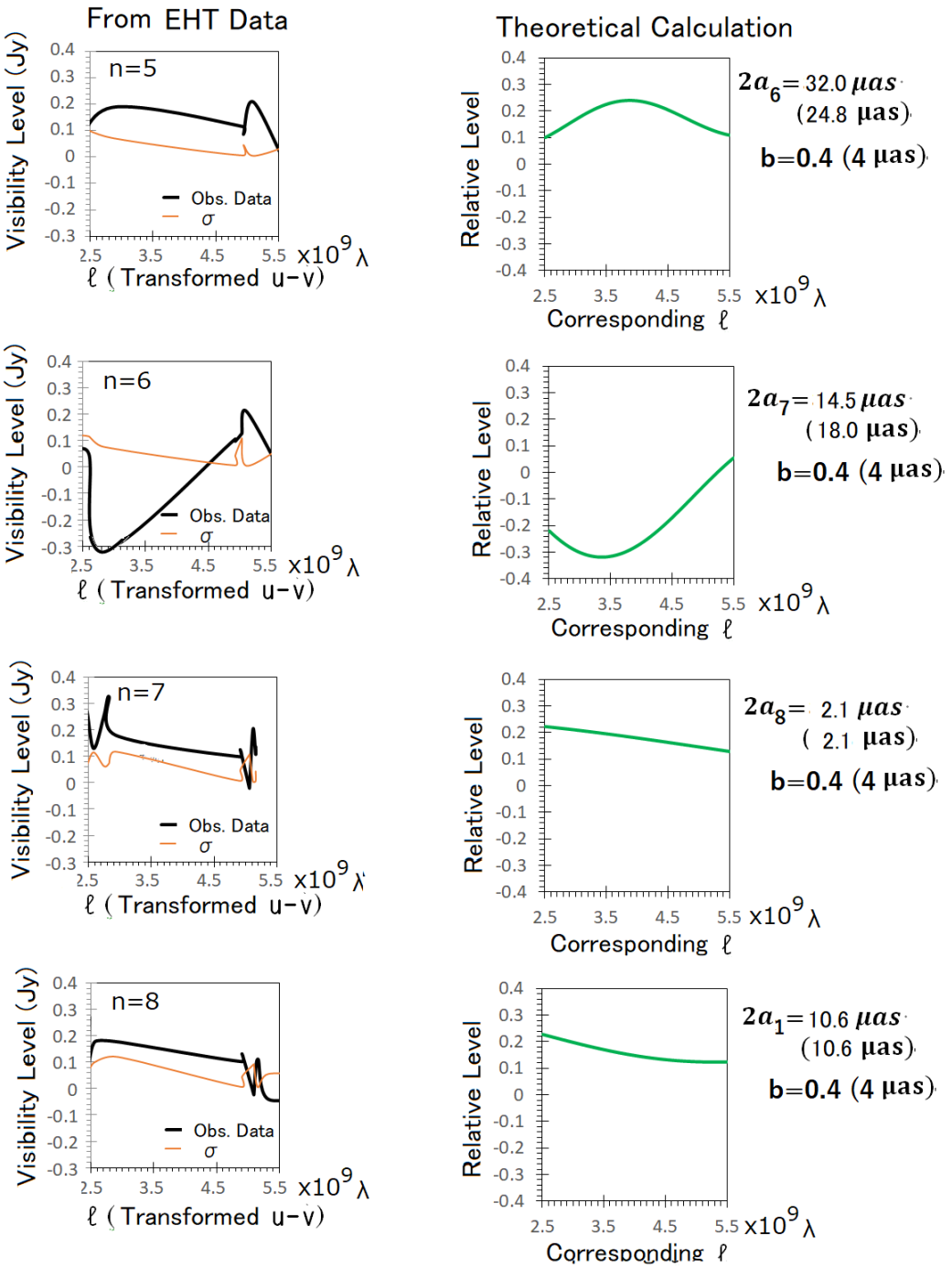


**Figure 14 (B).** Same with Figure 13(A) as continuation of phase number $m_r$ from 5 to 8.

### 4.3 Comparison of T-LV with E-LV for EHT 96 Hi CASA and 96 Lo HOPS Data

#### 4.3.1 Case of 96 Hi CASA

In Figures 14(A) and 14 (B), E-LVs are displayed, repeating the results in Figure 10 by trimming the LV to the effective range of ℓ from $2.5\times10^9\lambda$ to $5.5\times10^9\lambda$. In these figures, theoretically calculated linearized visibility (T-LV): green curves in the right column for b=0.4) and E-LV formed from the EHT 96 Hi CASA visibility data (black curves in the left column) are shown as pairs with the same $a_m$ in the left and right columns, respectively. Each pair of T-LV and E-LV results are displayed as a function of the data sampling timing for the orbiting ECB-SMBH. That is, for the E-LVs, which are given sequentially with relative phase number $m_r$, the corresponding T-LVs are indicated with phase number $m_a$; the numbers $m_r$ and $m_a$ are selected to the same BH distance $a_m$. To clarify the situation, Figure 15 is prepared, where the eight data sampling phases in the period of the ecliptic cycle of ECB-SMBH motions and parameter $a_m$ given as $a=a_m$ in eq.(4.5), are depicted. Along the orbit

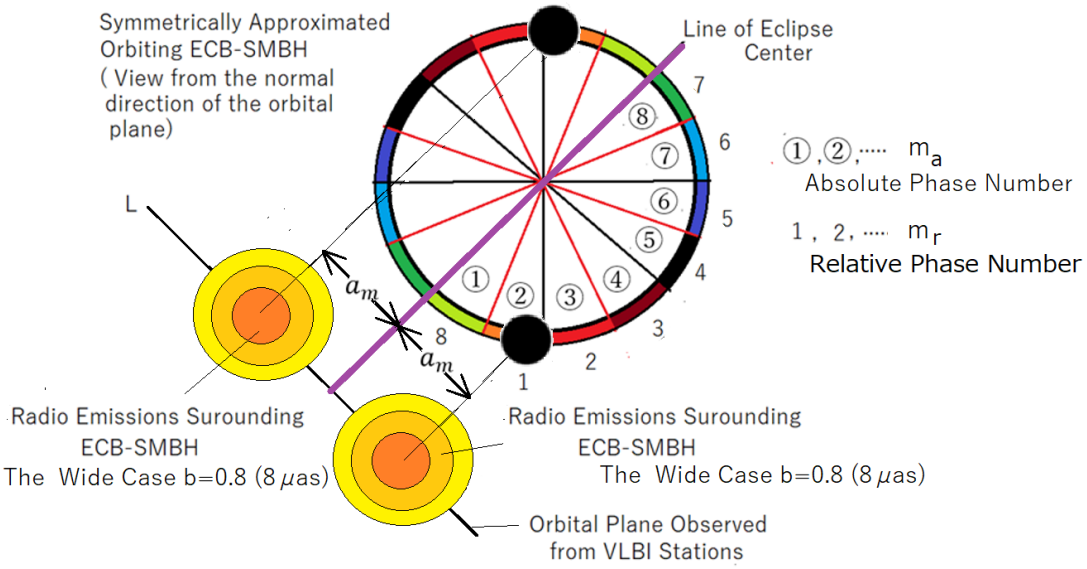


**Figure 15.** The depiction of 8 data sampling phases in the period of the ecliptic cycle of ECB-SMBH motions and parameter $a_m$ given as $a = a_m$, in eq.(4.5), that is given as projection of orbital position (phase) of the orbiting ECB-SMBH. The orbit of ECB -SMBH is observed as the line approximately parallel to the Galaxy equatorial plane from the observation sights of EHT VLBI systems. The ECB-SMBH that are surrounded by the radio wave emission zones with the zone radius expanded up to 3 times of the event horizon radius of the maximum rotating Kerr BHs move back and forth along the orbiting line with the corresponding projection phase of the circular orbit (approximated as a single). For a phase selected by a color along the circular orbit of ECB-SMBH, absolute number $m_a$ which is started to count from the closest phase to the eclipse line and the relative number $m_r$ which is started arbitrary at the phase corresponding to start timing of the analyses of EHT data are assigned .The distance of two BHs of ECB-SMBH is given by $2a_m$; for a given distance two numbers are assigned as $m_a$ for T-LV and $m_r$ for E-LV.

observed as a line parallel to the Galactic equatorial plane approximately from the observation sites of EHT VLBI systems, BHs of ECB-SMBH, surrounded by radio wave emission zones with the zone radius expanded up to three times the event horizon radius, of the maximally rotating Kerr BHs, move back and forth; the positions of BHs are expressed with the distance $2a_m$, projected onto the line orbit from the corresponding phase of the actual circular orbit (approximated as a single circle). To align the values between E-LV in Figures 14 (A) and 14 (B), amplitude and bias are adjusted to form T-LV based on the theoretical equation eq.(4.5), as given in Table 5. The effects of selecting the amplitude and bias will be discussed in the process of forming the image of ECB-SMBH in Subsection 4.5.

| The Case of 96 Hi CASA | | | The Case of 96 Lo HOPS | | |
|---|---|---|---|---|---|
| Relative Phase | Amplitude | Bias | Relative Phase | Amplitude | Bias |
| 1 | 0.05 | 0.2 | 1 | 0.3 | 0.25 |
| 2 | 0.13 | 0.1 | 2 | 0.075 | 0.18 |
| 3 | 0.14 | 0.1 | 3 | 0.14 | 0.13 |
| 4 | 0.06 | 0.25 | 4 | 0.06 | 0.25 |
| 5 | 0.1 | 0.15 | 5 | 0.065 | 0.25 |
| 6 | 0.04 | 0.16 | 6 | 0.04 | * |
| 7 | 0.15 | 0 | 7 | 0.065 | 0.16 |
| 8 | 0.1 | 0 | 8 | 0.1 | 0.03 |

* 0.57-0.05 $\ell$

**Table 5. Selected amplitude and Bias for T LV.**

Figure 15 is designed to elucidate the expressions of $m_a$ and $m_r$ in Figures 14 (A) and 14 (B). For a selected phase along the circular orbit of ECB-SMBH, the absolute number $m_a$, which starts counting from the closest phase to the eclipse line, and the relative number $m_r$, which begins arbitrarily at the phase corresponding to the start timing of the EHT data analysis, are assigned. The distance between the two BHs of ECB-SMBH is denoted by $2a_m$; $a_m$ is listed in the column of T-LV in Figures 14 (A) and 14 (B). The same distance between two ECB-SMBH members is assigned as $m_a$ for the T-LV and $m_r$ for the E-LV; the theoretically set distances of the core BHs are provided in the associated bracket as a reference. It is observed that in most cases, where the distance between the two members is closer than 15 $\mu as$, the theoretically set center position and detected center

position of the radio wave radiation zone coincide; however, there is a 10 to 20% difference in the positions of the BH center and center of the radio wave radiation zone, in cases where $2a_m$ (the distance between two member BHs) is larger than $20\mu as$.

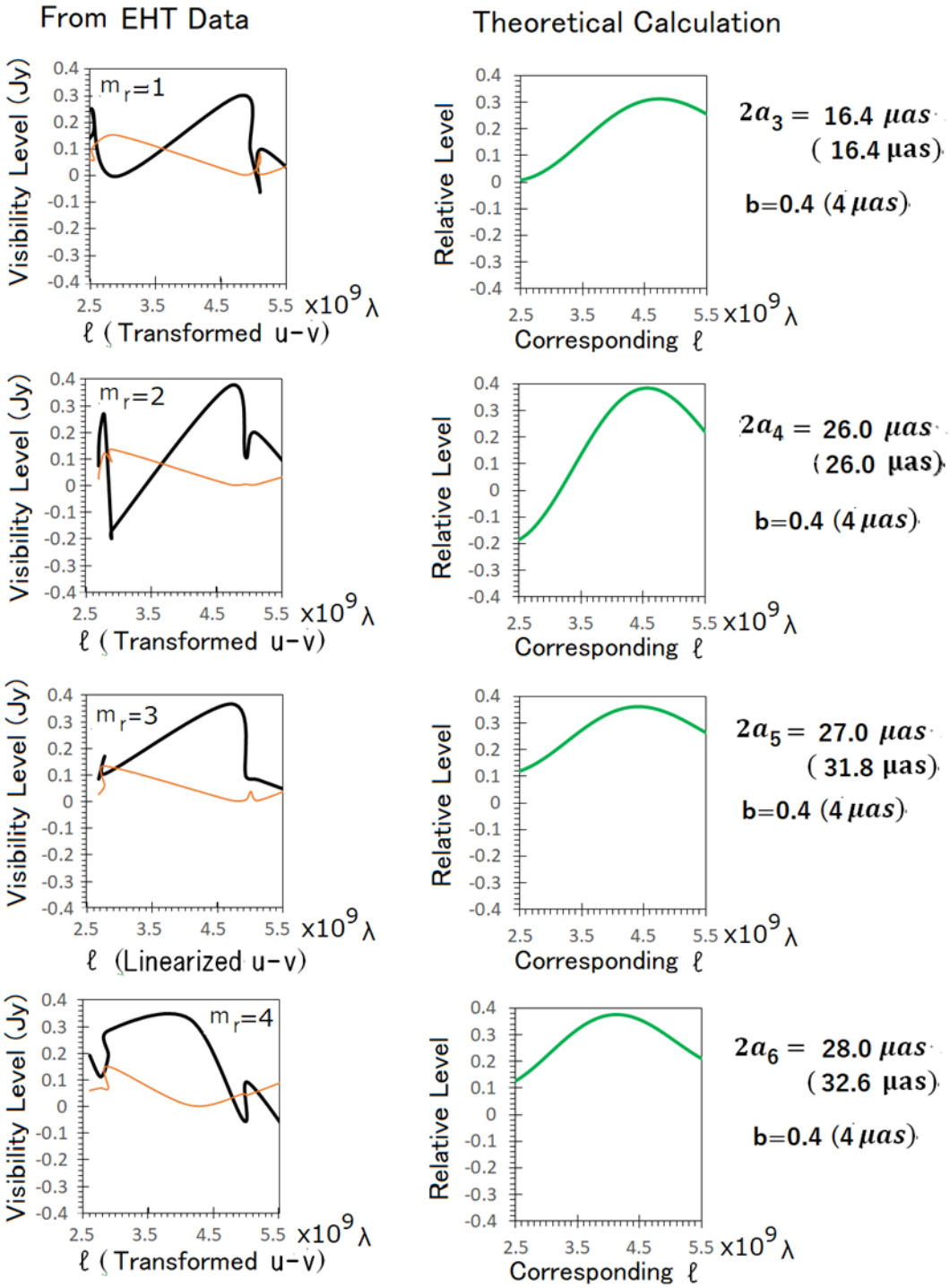


**Figure 16 (A).** Same with Figure 14 (A) for the case corresponding to EHT 96 Lo HOPS data.

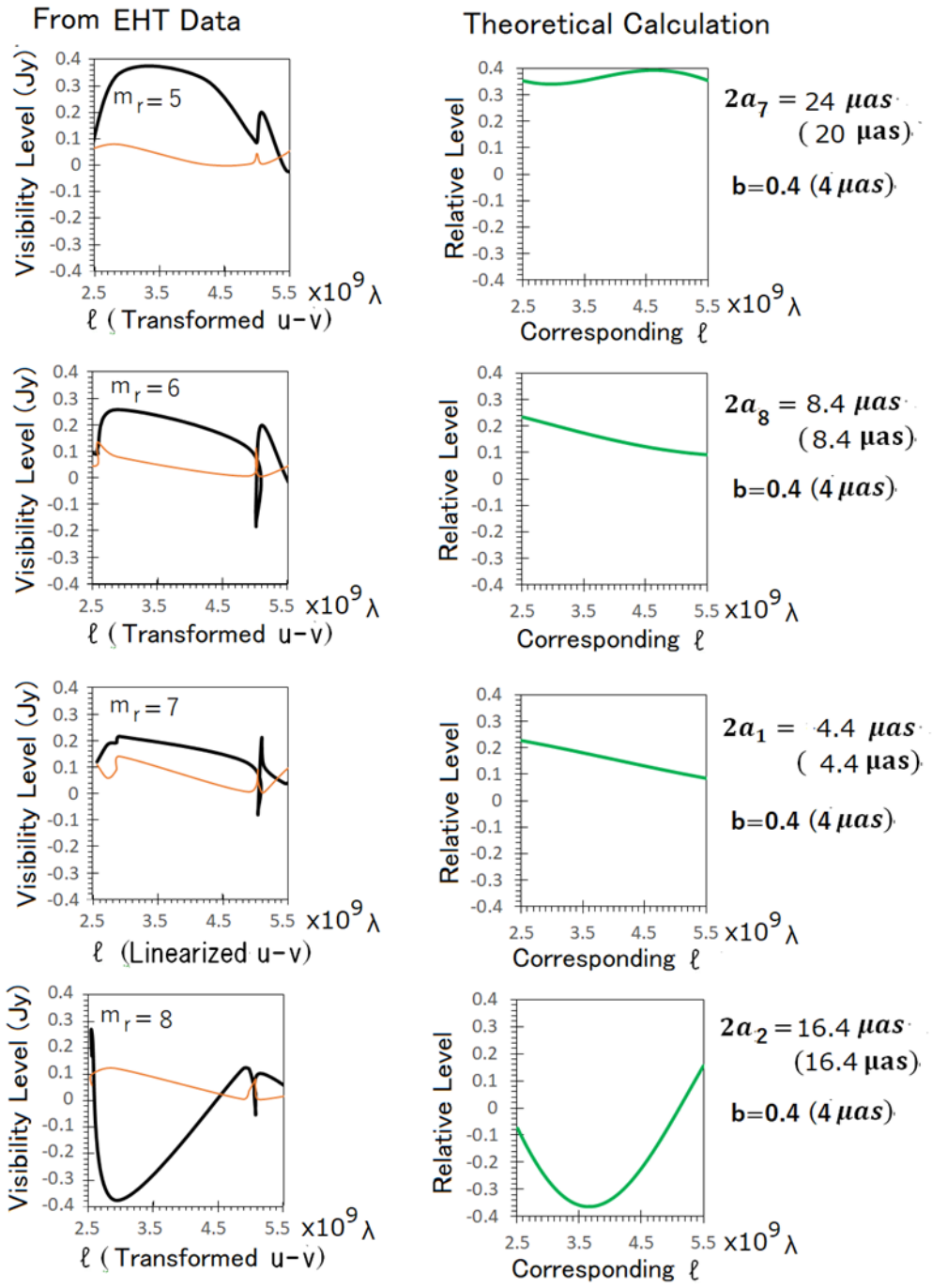


**Figure 16 (B):** Same with Figure 14 (B) for the case corresponding to EHT 96 Lo HOPS data.

### 4.3.2 Case of 96 Lo HOPS Data

In Figures 16 (A) and 16 (B), results of E-LV corresponding to the EHT data, 96 Lo HOPS, are presented alongside the corresponding T-LV, with same formats of the cases in Figures 14 (A) and 14 (B). As with the 96 Hi CASA data, E-LV formed from EHT 96 Lo HOPS data focus on the $\ell$ range from $2.5\times10^9\lambda$ to $5.5\times10^9\lambda$, where the orbital motions of ECB-SMBH are effectively reflected by EHT-VLBI observation. Theoretically calculated LVs (T-LV) are also shown to confirm the existence of the orbital motions of ECB-SMBH by revealing close similarity between E-LVs and T-LVs that are calculated based on eq.(4.5) with suitably adjusted amplitude and bias, as listed in Table 5. Similar to the EHT 96 Hi CASA case, T-LV (green curves in the right column for b=0.4) and E-LV formed from EHT visibility data (black curves in the left column) are indicated as pairs with the same $a_m$ (see Subsection 4.4). Akin to the 96 Hi CASA data, in most cases where the distance between two members is closer than 15 $\mu_{as}$ we see the center position of BHs set for calculation and detected center position of the radio wave radiation zone coinciding; however, there is a 10 to 20% difference in positions of the BH center and center of the radio wave radiation zone in cases where the distance between two member BHs is larger than 20μas. In general, there is a basic coincidence between E -LV and T-LV, similar to the 96 Hi CASA data case, in all these displayed comparison results.

### 4.4 Case of Wide Radio Wave Emission Zone

As described concerning theoretical eqs.(4.3)–(4.5), we assume

that the radio emissions surrounding ECB-SMBH form a single bright zone, showing maximum intensity at the center of the observing disk and fading to zero at the circular limb of the disk with radius b. We stand on the premise that, rather than adopting the previously proposed ring or shadow concept based on a thin accreting plasma disk surrounding BHs, we select results of a simple bright zone surrounding the supermassive black hole (see Section 5 also). The parameter b for the radius of the radio wave emitting zone significantly impacts the theoretically calculated T LV, as shown in Figure 13, where the minimum limit of the sensitive baseline length $\ell$ at $5.5\times10^{9}\lambda$ shows the maximum possibility of the radio wave emission zone for b=0.8 (8 $\mu as$).

In addition to the previously discussed comparison of E LV and T-LV corresponding to the EHT 96 Hi CASA data for E-LV and the case of b=0.4 for T-LV, we further investigate the comparison for the case of a wide radio wave emission zone with b=0.8. Figures 17 (A) and 17 (B) express the comparison of T-LV and E -LV for the case of a wide radio wave emission zone with b=0.8. The setup of the diagram remains consistent with the earlier cases of E-LVs and T-LV. To achieve a closer similarity between E-LV, shown in the left column by black curves, we search for the amplitude and bias values, which are then directly indicated in the corresponding phase of T-LV, calculated by changing the b value from 0.4 to the wider case of 0.8 (8 $\mu as$). With respect to the E-LV corresponding to EHT 96 Hi CASA visibility data, which are displayed by repeating the results in Figure 10 and focusing

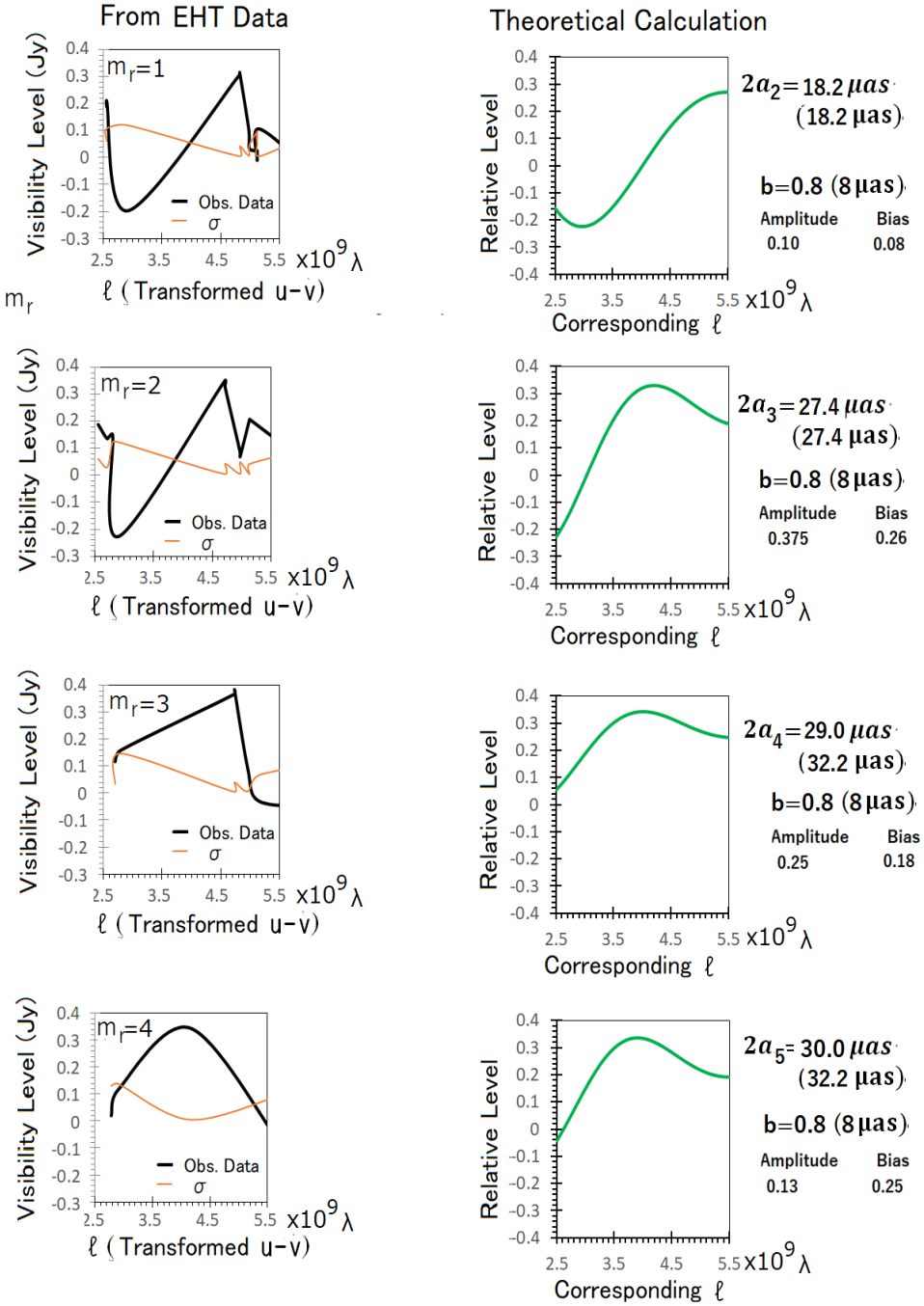


**Figure 17 (A).** Same with Figure 14 (A) for the case of wide radio emission zones with radius b=0.8 (8 $\mu as$). The amplitude and bias adding to eq.(4.5) to make T-LV and E-LV close are given in the corresponding $a_{ma}$.

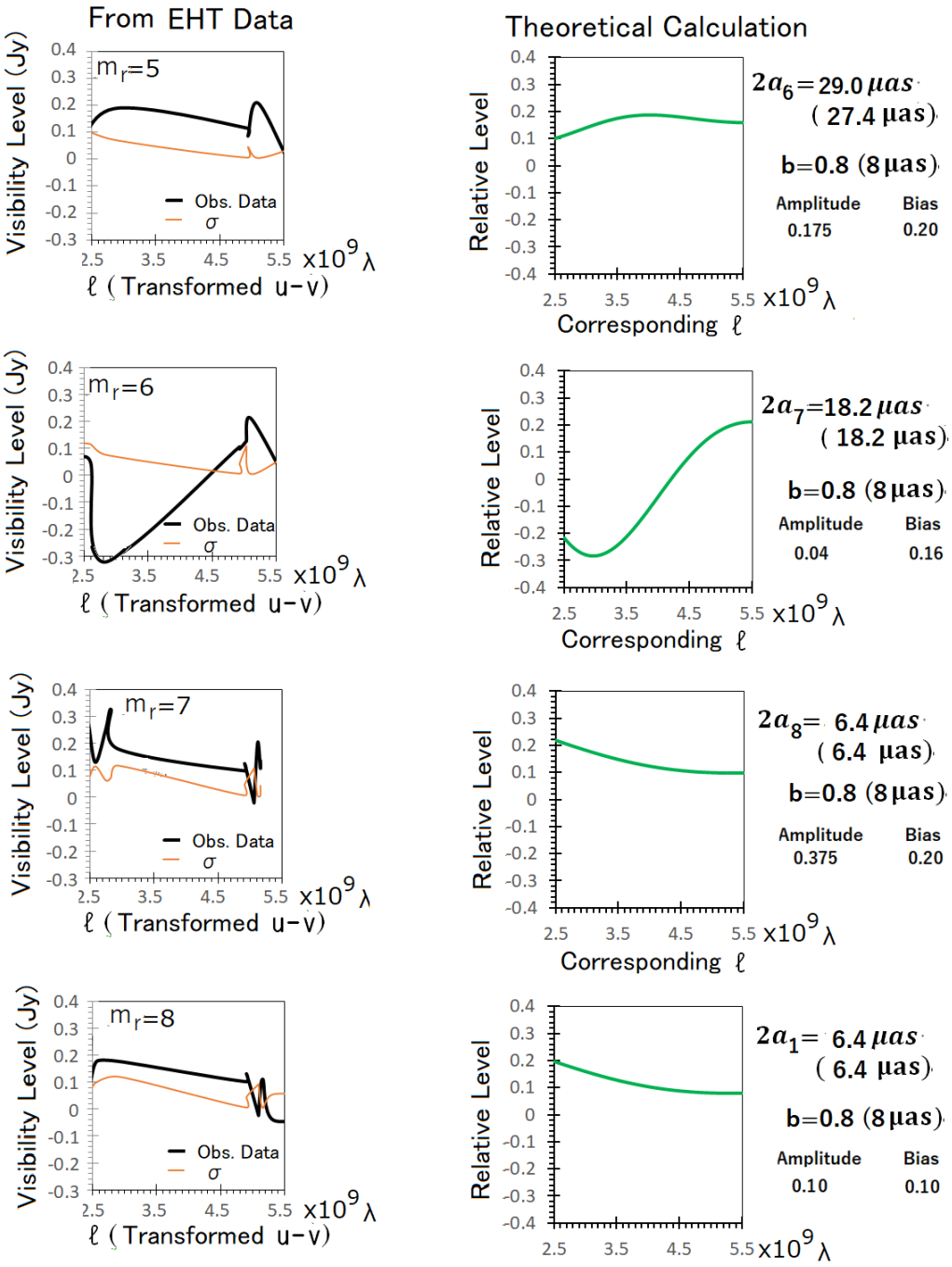


**Figure 17 (B).** Same with Figure 17 (A) for cases of $m_r$=5-8.

on the effective range of ℓ from $2.5\times10^9\lambda$ to $5.5\times10^9\lambda$, given in the left column with black curves, T-LVs calculated for b=0.8 following eq.(4.5) are aligned in the right column, with green curves. The indicated pair of LVs in the left column for the E-LV and in the right column for the T-LV are identified as belonging to the same parameter $a_m$, where $2a_m(\times10\mu as)$ indicates the distance between the two BHs of ECB-SMBH.

Comparing with the case of the narrow zone condition with b=0.4, the theoretically fitting amplitude and bias values increase, as directly indicated to compare with Table 5 for narrow b. There are also differences in the decided $a_m$ values for the same E-LV between the results given by Figures 14 (A), 14 (B), and Figures 17 (A), 17 (B). For this difference, we consider both results to be acceptable, reflecting the effects of the selected width of the radio emission zones surrounding ECB-SMBH. Because the cases of b=0.8 still show reasonable results for the movement of ECB-SMBH, we will proceed to obtain the image of ECB-SMBH for these wide emission zones in the next Subsection 4.6.

### 4.5 Image of Orbiting ECB-SMBH Deduced from EHT Data of SgrA*

Summarizing the current work to confirm the existence of ECB-SMBH, originally proposed based on the observation of decameter radio wave pulses caused by spinning Kerr black holes [14], through comparison with 1.3 mm VLBI observation data [27], including EHT data [30], we construct images of ECB-SMBH at the center of SgrA*. The image formation is carried out for radio wave emissions at 1.3 mm, $S(p,q)$, as given by:

$$S(p,q) = \mathrm{A}(p-a)\cdot\cos\left[\frac{\pi(p-a)}{2b}\right]$$

$$+\mathrm{A}(p+a)\cdot\cos\left[\frac{\pi(p+a)}{2b}\right] + Bias. \qquad (4.10)$$

where

$$\mathrm{A}(p\pm a) = \begin{cases} A_0 : Const\ for\ (p\pm a)^2 + q^2 < b^2 \\ 0 \qquad\quad for\ (p\pm a)^2 + q^2 > b^2 \end{cases}$$

and $0.8 \geq b > 0$.

About eq.(4.10) we have already investigated as case of q=0, where the radio emission sources along the linearly observable orbit of ECB-SMBH, by finding the T-LV, through calculating the Fourier transformation to focus on the linear baseline component ℓ. Through studies described in Subsections 4.1 to 4.4, the theoretical basis for using S(p,0) has been verified by finding a coincidence between E-LV from EHT data and T-LV resulting from the Fourier transformation of S(p,0).

From the validated radio wave emission model S(p,0), we proceed to expand the emission zone associated with the moving ECB-SMBH, assuming a circular region for the emission zones. This is achieved by introducing A($p\pm a$) functions, which define circular regions

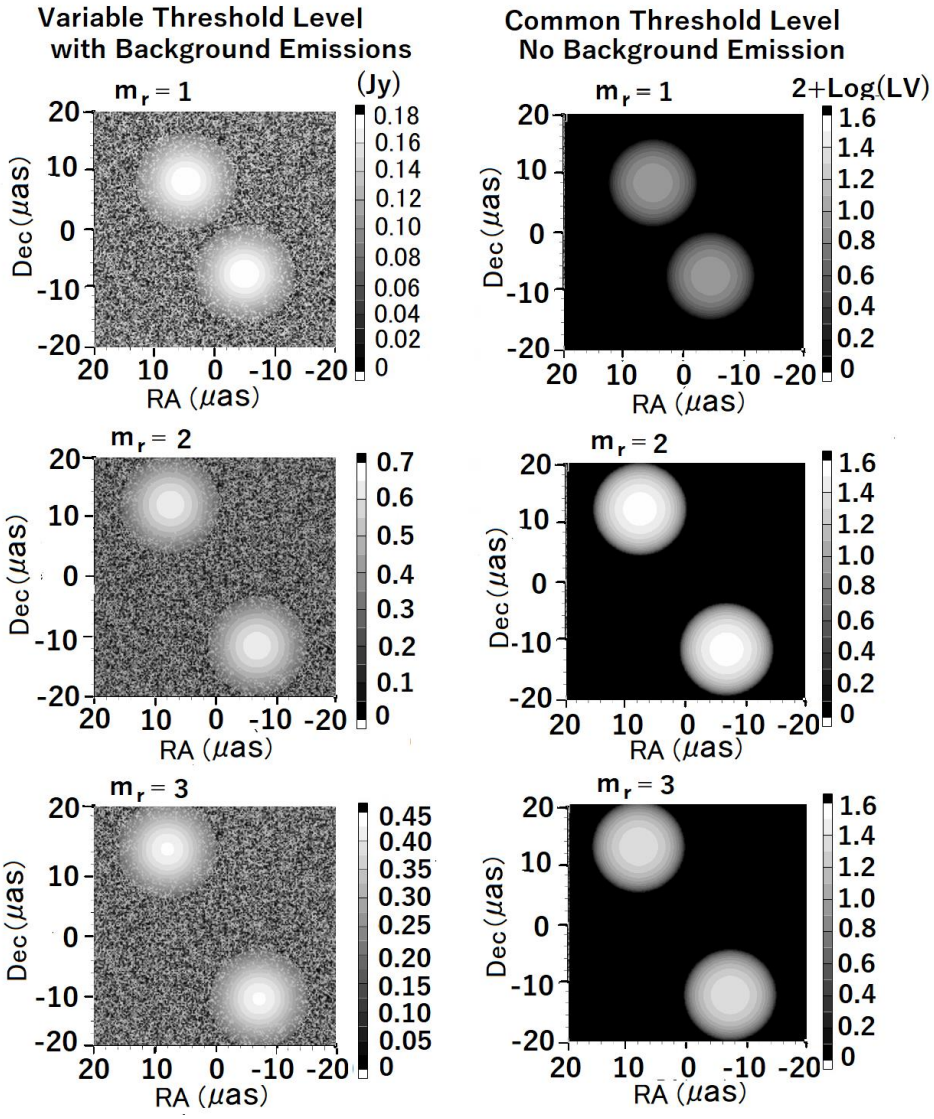

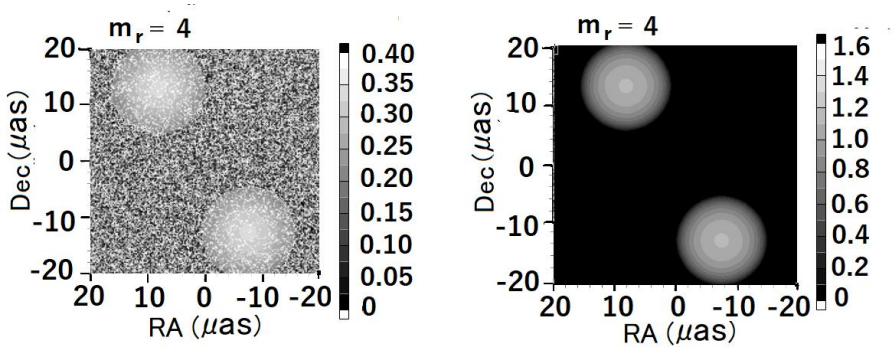


**Figure 18 (A).** Formed images of ECB-SMBH at the center of SgrA* based on eq.(4.10) which is endorsed by comparison of E-LV and T-LV as the consequence of the EHT observation data of the 96-Hi CASA. Images are displayed for the four sequences of movement corresponding to the data stacking timing from $m_r$=1 to $m_r$=4. The images of the moving ECB-SMBH, are displayed in two ways as given in the left column where the resulting images are indicated with variable threshold of the gray code whose representing levels change in image by image to make the most suitable viewing threshold level of the resulting picture; in the right column, the radio wave intensity R is given by 2+log(R) with constant threshold of the gray code. whose representing levels are same throughout all images to visualize the relative brightness or darkness of the radio emissions clear.

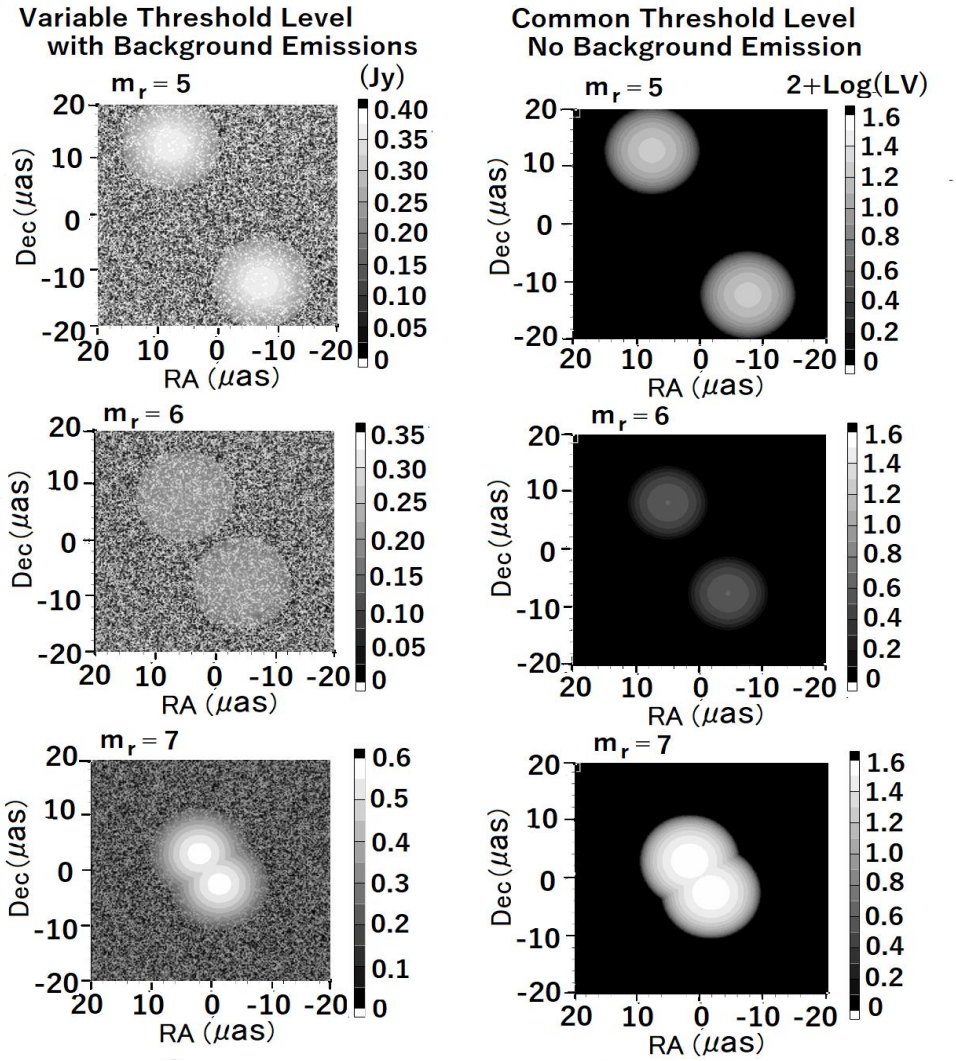

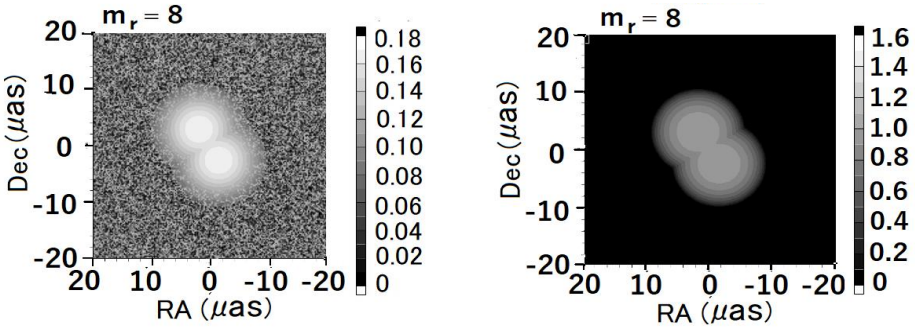


**Figure 18 (B).** Same with Figure 18 (A) for the sequence of phase $m_r$=5 *to* 8.

controlled by the radius b (0.8≥$b$>0). For this parameter b we opt for a wider case of 0.8 (8 $\mu as$) to reconstruct the images of ECB-SMBH as detailed in Subsection 4.4. The necessary amplitude $A_0$ and Bias are provided in Figures 17 (A) and 17 (B) in Subsection 4.4, indicating that the resulting images of ECB-SMBH are not merely simplistic model outputs but rather reflect the actual situation of SgrA* as observed through EHT 96 Hi CASA data.

In Figures 18 (A) and 18 (B), we display the constructed images of ECB-SMBH at the center of SgrA*, based on eq.(4.10) and supported by the comparison of E-LV and T-LV as a result of analyzing the EHT data of 96 Hi CASA. These images correspond to the eight phases of data stacking timing from $m_r$=1 to $m_r$=8, with the comparison process of E-LV and T-LV detailed in relation to Figures 17 (A) and 17 (B). The images showcase the moving ECB-SMBH in two formats: one in the left column with a variable threshold for gray coding to optimize the contrast of each image, and another in the right column with a consistent threshold for gray coding across all images to highlight the relative brightness or darkness of the radio emissions, by applying the logarithmic function. The impact of background radio wave emissions is significant for discussing the signal to noise ratio from the VLBI observations perspective.

Noises are incorporated based on the bias level indicated in Figures 17 (A) and 17 (B), as seen in the images in the left panel. By averaging a sufficient number of noise cases, a constant level emerges, allowing us to differentiate and subtract the noise level from the signal. Consequently, images in the right hand column display the radio wave emissions surrounding the moving ECB -SMBH without noise interference.

Throughout the eight phases of data stacking for E-LV and the corresponding T-LV, the movement of ECB-SMBH, along with its associated radio wave emission zones approximately 3.3 times the diameter of the Kerr event horizon of the BHs, is evident. Between phases $m_r$=7 and $m_r$=8, where the observational distances between the two BHs are 6.4 $\mu as$, a full eclipse phenomenon is expected, with one member of the binary transitioning from the left side of the image to the right, vice versa.

The change in image brightness between phases $m_r$=7 and $m_r$=8 remains unclear; it may result from a partial overlap of intrinsic data levels in neighboring phases. Although much more accurate determination of the orbiting period is deferred for future research, the existence of ECB-SMBH is corroborated by the images in Figures 18 (A) and 18 (B), which demonstrate the consistent movement of ECB-SMBH.

## 5. Extension of Concept of ECB-SMBH to M87*

### 5.1 Brief Review of Published Image of M87*

In Section 4, we have elucidated that the radio wave images of mm radio waves of ECB-SMBH at SgrA* feature bright zones surrounding BHs over the event horizon radius of each ECB-SMBH member. Unlike the intricate structures of emission intensity, such as rings or shadows, originally proposed under the geometrically thin and optically thick accreting disk condition that allows to consider fine effects of GR space time for the trace of the ray paths of radiated waves, these images eliminate detailed structural emission intensity. This difference may be caused by geometrically thick and optically thin accreting disk in the case of ECB-SMBH. Given the shared physics underlying the imaging of radio wave sources around SMBHs at SgrA* and M87*(the core SMBH at the center of galaxy M87), we reinvestigate the images of SMBH M87* in this section.

Current research on emissions from BHs predominantly focuses on scenarios where the BH is enveloped by a geometrically thin and optically thick accretion disk. This configuration yields compelling radiation source images surrounding SMBHs that facilitate lensing, bending, and photon capture processes, resulting in the emergence of a shadow alongside a bright emission ring [35, 36]. VLBI observations are heralded as a promising approach to directly verify the existence of SMBHs, clarifying these effects [37−41].

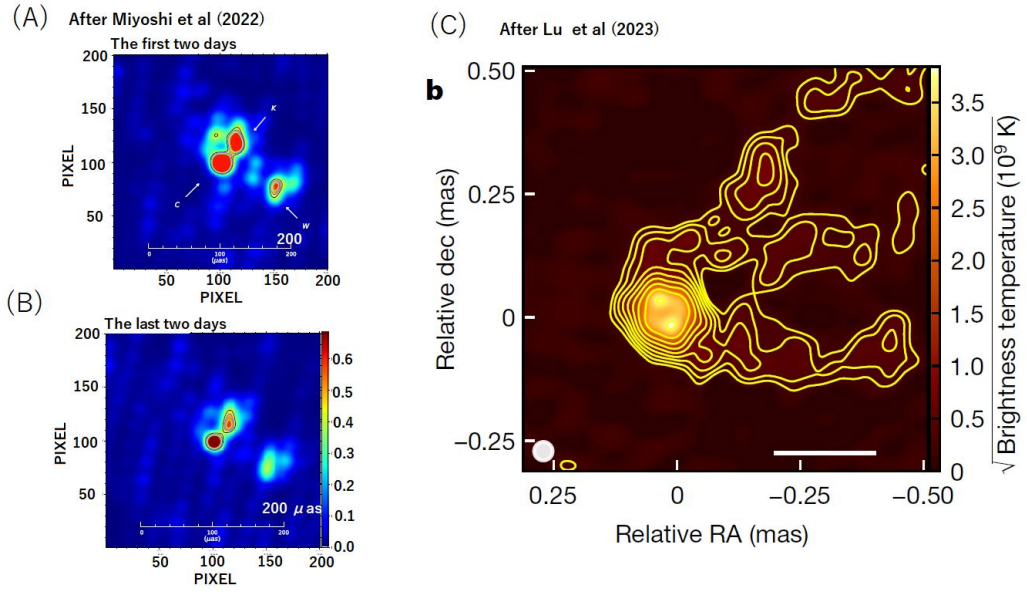


**Figure 19.** Radio wave images of M87* resulted by Miyoshi et al. [20] based on the EHT data observed in 2017 by 1.3 mm VLBI (A and B panels), and resulted by Lu et al. [31], based on GMVA observations, in 2018 by 3.5 mm VLBI.

The EHT collaboration's campaign for VLBI observation of SgrA* and M87* represented one of the most ambitious approach. However, due to the time dependent variations in detected visibilities, the report of the Sgr A* image was delayed until 2022, while the M87* image was released in 2019, depicting the BH shadow encircled by a bright ring.

In 2022, Miyoshi et al. published [20] the radio wave image of M87*, criticizing the 2019 EHT collaboration's depiction of M87* as flawed. They attributed the error to inadequate data covering the u v range of the visibility corresponding to an observation angle approximately 40 $\mu as$ and the erroneous selection of the central object at the outset of the hybrid mapping process for forming the radio source image, referring to the gap in data shifted from the center as the shadow‖ anticipated from their BH. In their paper, Miyoshi et al. [20] presented an alternative image (hereafter M Image), as shown in Figure 19, Panels (A) and (B), excerpting an essential part from their Figure 8, relevant to the subjects of the present work. They identified two notably intense sources as the core and knot in the source area of the jet without specifying the SMBH's location (Miyoshi et al presented their interpretation afterwards negating the relation to the potential super massive black hole [49].)

In 2023, Lu et al. released the image of M87* (hereafter L Image) based on the Global Millimeter VLBI Array (GMVA) observation campaign conducted at 3.5 mm wavelength on April 14 to 15, 2018, with the addition of the Atacama large millimeter/submillimeter array (ALMA) and the Greenland telescope (GLT). In Figure 19, panel (C), a copy of the published image is displayed, selected from their Figure 1 panel (b). Lu et al. noted that, within the

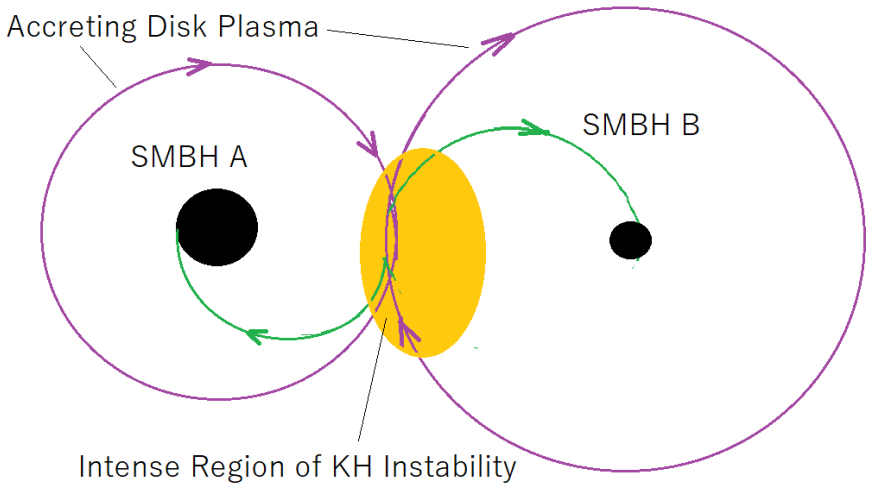


**Figure 20.** Configuration of accreting paths of plasmas surrounding ECB-SMBH.

Element particles of accreting plasmas with a common rotation sense form counter streams, in the center portion, that cause KH instabilities.

resolution limit, the core region of M87* harbors a ring approximately 50% larger in diameter than the ring image reported by EHT at 1.3 mm wavelength, with two bright sections overlapping the detected faint ring.

### 5.2 Interpretation of Reported Images of M87* as ECB-SMBH

In the current paradigm regarding the possible generation of gravitational waves from BHs, no proposal of a binary system has been made about the central BH at the core of the Galaxy. However, we have currently concluded the existence of the extreme central binary of SMBH (ECB-SMBH) for SgrA* [14], based on the results of the decameter radio wave pulses with a theoretical assertion that "No gravitational waves are emitted from the SMBH" [19]. At this juncture, we employ the concept of ECB-SMBH to interpret the images reported by Miyoshi et al. and Lu et al. (hereafter referred to as ML Images). In this context, Sgr A* as ECB-SMBH exhibits simple bright zones surrounding the orbiting SMBHs, indicative of a thick accretion disk. Due to the binary configuration, accreting plasmas may effectively lose angular momentum in the central area between the two BHs, where plasma flows circulating each BH meet, forming counter streams (see Figure 20). This large area is likely subject to Kelvin Helmholtz instabilities caused by the counter streams of the accreting flows. Consequently, plasmas migrating from distant regions with significant angular momentum can fall into the BHs more effectively after losing angular momentum under the intense gravitational effects of ECB-SMBH, without significant counteraction from centrifugal forces due to the reduction in angular momentum of the circulating plasma.

Therefore, we identify SMBHs at the center of the bright spots presented by the M L Images; naturally, we conclude the existence of ECB-SMBH corresponding to the two spots in the M L Images. To verify the existence of ECB-SMBH at M87*, we need to determine the parameters of the orbiting members, which we subsequently refer to as M87*-A and M87*-B. This requires efforts from two perspectives: one is the geometrical aspect, which can be addressed within the framework of the image analysis, and the other is the dynamics in the real physical state.

#### a) Geometrical Side Approach

The goal of this approach is to determine the orbit configurations. Initially, we assume circular orbits for both M87*-A and M87*-B, which are generally observed as ellipses due to the inclination of the orbital plane, though we lack precise information about the inclination angle. However, we can establish the radii of the circular orbits from the observable major axes of the ellipses, independent of the orbital plane's inclination. Therefore, we aim to identify ellipses that pass through the center of the two spots in both the M Image and L Image. Considering that the positions of M87*-A and M87*-B in both images are fixed, we must determine eight coordinates in this two dimensional configuration. Since these two images are described with relative coordinates, the relationship between the coordinate centers of the M Image and L Image is adjustable, providing two (due to the two dimensional constraint) free parameters. We use the frame of the Lu et al. image, where two spots are already established as the fixed base, and align the M Image using the same observational angle (measured in $\mu as$) to match the fixed mutual relation of the two spots in the M Image. With six fixed coordinate parameters, we can search for two unknown coordinates that define the center position of the two ellipses. To establish the two ellipses passing through the four center positions of M87*-A and M87*-B in the M Image and L Image, we require a parameter for the common direction of the major axis of both ellipses, two for the lengths of the major axes, and one for the common eccentricity.

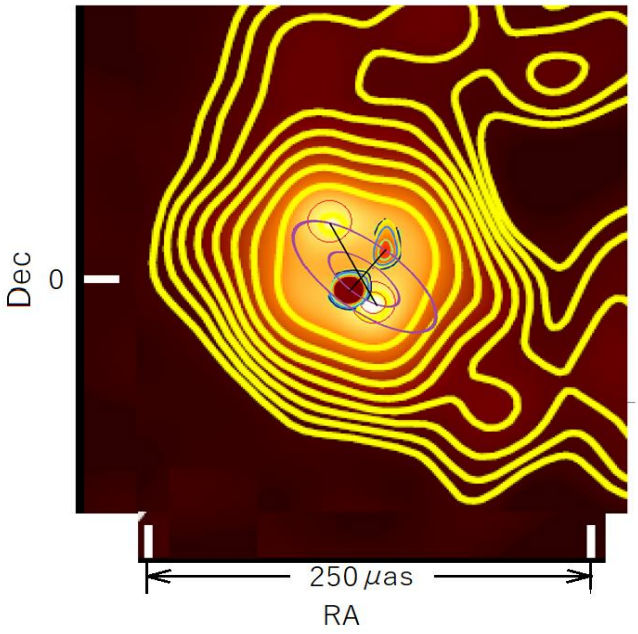


**Figure 21.** Graphical solutions to find the orbits of possible ECB-SMBH at M87*. To search for the possibility to find the solutions to connect two bright spots provided by M Image and L Image two common circular orbits which are observable as ellipses are depicted.

Therefore, including the unknown center coordinates, we have 6 unknown parameters alongside 6 known parameters (the given coordinates of the 4 center positions of M87*-A and M87*-B, excluding the two degrees of freedom to fix the centers of the M Image and L Image). Thus, theoretically, we can solve for the two ellipses numerically.

As an initial approach, we have depicted the ellipses on the combined M L Image, as shown in Figure 21. Starting from this preliminary depiction, we aim to determine accurate orbits using analytical methods. For the coordinates of right ascension X and declination Y, we define the coordinate system $(\xi,\eta)$ where the unit vector $\hat{\xi}$ is parallel to the direction of the major axis of the two orbits, and the unit vector $\eta$ is set perpendicular to $\hat{\xi}$ (refer to Subsection 5.4). Consequently, we establish relationships between the coordinate systems, as

$$\xi = -X\cos\theta - Y\cos\theta$$

$$\eta = -X\sin\theta + Y\cos\theta \tag{5.1}$$

where θ is the angle between the direction of right ascension and major axis of the ellipses for the orbits of M87*-A and M87*-B. Instead of directly solving the equations required to define the ellipses, we sought the best solutions for fixing the ellipses for the lengths of the major semiaxis $a_A$ and $a_B$, respectively for M87*-A and M87*-B, as well as for the lengths of the minor semiaxis $b_A$ and $b_B$, respectively. We did this by creating a decision function $D(a_A,a_B,b_A,b_B,\theta)$, the minimum point of which provides the solution in the (X, Y) plane, coupled with eq.(5.1). This involves:

$$D(a_A, b_A\,\kappa,\alpha,\beta,\theta) = \sum_{m=1}^{2}\left[\left(\frac{\xi_{m1}}{a_A}\right)^2 + \left(\frac{\eta_{m1}}{\kappa a_A}\right)^2 - 1\right]^2 + \sum_{m=1}^{2}\left[\left(\frac{\xi_{m2}}{a_B}\right)^2 + \left(\frac{\eta_{m2}}{\kappa a_B}\right)^2 - 1\right]^2. \tag{5.2}$$

where $\kappa = b_A/a_A = b_B/a_B$; and $\xi_{1n}, \eta_{1n}, \xi_{2n}$, and $\eta_{2n}$ (n=1 and 2) are given as

$$\xi_{1n} = -X_{1n}\cos\theta - Y_{1n}\cos\theta,$$
$$\eta_{1n} = -X_{1n}\sin\theta + Y_{1n}\cos\theta,$$
$$\xi_{2n} = -X_{2n}\cos\theta - Y_{2n}\cos\theta + \alpha,$$

and

$$\eta_{2n} = -X_{2n}\sin\theta + Y_{2n}\cos\theta + \beta \tag{5.3}$$

with α and β representing the adjustment of center coordinates for relative right ascensions and declination.In eq.(5.3), $X_{m1}$, *and* $Y_{m1}$ are right ascension and declination , respectively of M87*-A with m=1 for the L Image data (L:A), and m=2 for the M Image data(M:A); further $X_{m2}$ and $Y_{m2}$ are right ascension and declination , respectively of M87*-B with m=1 for the L Image data (L:B), and m=2 for the M Image data (M:B).

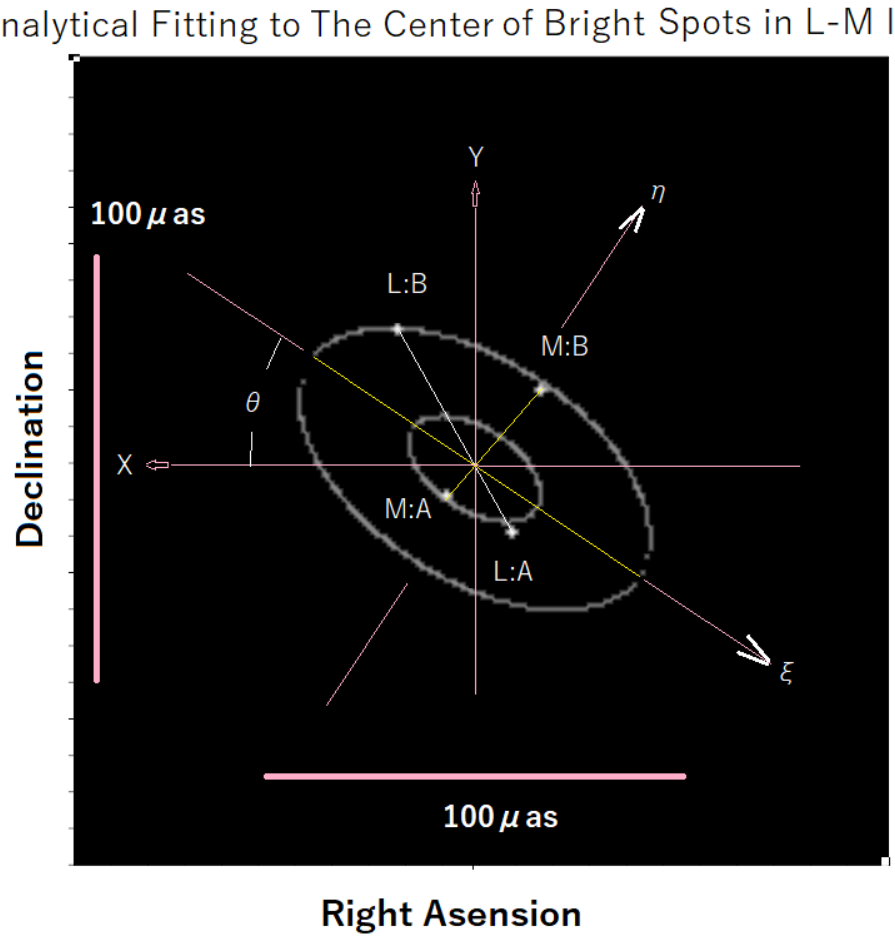


**Figure 22.** The decided two orbits of proposed ECB-SMBH at M87*. The decision of the central coordinate, axes directions and length and eccentricity are resulted by solving eq.(5.2) finding the minimum point for D value.

The results of the analytical fitting described here are given in Figure 22 where the centers of each bright spot in the L M Images are marked as L:A and L:B respectively for M87*-A and M87*-B in the L Image, and M:A and M:B for M87*- A and M87*- B in the M Image, respectively. It is observed that all four centers of the bright spots are situated close to the identified ellipses, except for L:A, which deviates from its orbit more than the other three cases. However, considering that there is an error margin of ±5% in determining the center position of the bright spots within the broadly expanded bright disk in the L M Image, we deem the deviation of L: A from its ideal position to be within an acceptable range at this stage. The results are summarized in Table 6, where the widths of the visible angles are denoted in $\mu as$.

Table 6 Fitting Results of Ellipse Orbits for Bright Spots in L- M Image (unit: $\mu$as)

| Orbit of M87*-A | | Orbit of M87*-B | |
|---|---|---|---|
| Semi-Major Axis | Semi-Minor Axis | Semi-Major Axis | Semi-Minor Axis |
| 17.4 | 8.7 | 46.5 | 23.2 |

### b) Physics Side Approach

From the geometrically determined elliptical orbits of M87*-A and M87*-B, we can deduce the physics of ECB-SMBH at M87* by knowing the distance, to M87*,that provides the actual sizes of the radii $r_A$ and $r_B$ for the orbits of M87*-A and M87*-B, respectively based on the observing angles of the semi major axes of the ellipse as listed in Table 6. As a key timeframe, we note that the shift in positions of ECB-SMBH between the M Image and L Image indicates the orbital motion of ECB-SMBH over 369 d, corresponding to the interval between April 10 and 11, 2017 (when the EHT observation for the M Image was made), and April 14 and 15, 2018 (when the data for the L Image was observed). Then, we can establish equations in the frame of Newtonian dynamics with the mases $M_A$ and $M_B$ of ECB-SMBH components M87*-A and 87*- B, respectively, as

$$r_A\left(\frac{2\pi}{T}\right)^2 = \frac{GM_B}{(r_A + r_B)^2},$$

and

$$r_B \left(\frac{2\pi}{T}\right)^2 = \frac{GM_A}{(r_A + r_B)^2} \tag{5.4}$$

where T and G are the orbiting period and gravitational constant, respectively. From the two equations of eq.(5.4) we have Kepler's law for the binary, as

$$\left(\frac{2\pi}{T}\right)^2 = \frac{G(M_A + M_B)}{(r_A + r_B)^3}\,. \tag{5.5}$$

And it also follows that

$$\frac{r_A}{r_B} = \frac{M_B}{M_A}\,. \tag{5.6}$$

When we introduce $\kappa_R$ as $\kappa_R \equiv r_A / r_B$ , and the total mass $M_T (=M_A+M_B)$, it follows that

$$M_A = M_T/(1+\kappa_R)\,, \qquad and \qquad M_B = \kappa_R \cdot M_T/(1+\kappa_R)\,. \tag{5.7}$$

The current estimates of distance and mass for M87* are not unified but vary around certain average values; for distance, these include 16.4± 0.5 Mpc [42],$16.67^{+1.02}_{-0.96}$Mpc [43], 16.8 Mpc [31] 17.0±0.4 Mpc [44], and 17.9Mpc [45]. For the total mass estimates are $6.5\times10^9 M_\odot$ [31], $(6.5\pm0.7)\times10^9 M_\odot$ [21], and $(6.6\pm0.4)\times10^9 M_\odot$ [42]. Among these, the distance of M87* seems to be converging approximately 16.8 Mpc, which is also the figure employed in the EHTC paper. The mass of M87* has been extensively derived by Gebhardt et al. [45] from stellar dynamics; however, they assumed a distance of 17.9 Mpc for M87*. Following their assertion that the deduced value of the mass scales linearly with the assumed distance, we can adjust the mass to $(6.2\pm0.4)\times10^9 M_\odot$,corresponding to the distance 16.8±0.8 Mpc. We decided to use this value as the total mass of M87* in the present work, as it is the median value cited in the EHTC paper.

### 5.3 Deduced Parameters of ECB-SMBH at M87*

Based on the relations from eqs.(5.4) to (5.7), we estimate the parameters for the proposed ECB-SMBH, M87*-A, and M87*-B, starting from the visual angles of the semi major axis lengths listed in Table 6. In concert with the distance of M87*, as crucial factor for calculating physical parameters from visual angles, we account for a scaling error of ±5% for the semi major axis lengths. Therefore, we calculate parameters for 9 scenarios resulting from combinations of three cases each for the upper limit, middle value, and lower limit for the M87* distance, and for the scaling error of the visual angle.

Table 7

Orbit radius of M87*-A ($r_A$) and M87*-B ($r_B$) (Unit:$10^{15}$ cm)

| $\mathbf{r_A}$ | | | | $\mathbf{r_B}$ | | | |
|---|---|---|---|---|---|---|---|
| | Distance | | | | Distance | | |
| Error | 17.6Mpc | 16.8Mpc | 16.0Mpc | Error | 17.6Mpc | 16.8Mpc | 16.0Mpc |
| 5% | 4.81 | 4.59 | 4.37 | 5% | 12.84 | 12.26 | 11.68 |
| 0% | 4.58 | 4.37 | 4.16 | 0% | 12.24 | 11.68 | 11.13 |
| -5% | 4.35 | 4.15 | 3.95 | -5% | 11.63 | 11.10 | 10.58 |

In Table 7, the orbital radii $r_A$ of M87*- A and $r_B$ of M87*- B, derived from the semi major angles listed in Table 6 by multiplying by the M87* distance 16.8 Mpc, are summarized as follows: for $r_A$ as $4.37^{-0.44}_{+0.42}\times10^{15}$ cm, and $r_B$ as $1.16^{+0.12}_{-0.10}\times10^{16}$ cm.

Table 8

Mass of M87*-A ($M_A$) and M87*-B ($M_B$) (Unit:$10^9$ $M_\odot$)

| $M_A$ | | | | $M_B$ | | | |
|---|---|---|---|---|---|---|---|
| | Distance | | | | Distance | | |
| Error | 17.6Mpc | 16.8Mpc | 16.0Mpc | Error | 17.6Mpc | 16.8Mpc | 16.0Mpc |
| 5% | 4.72 | 4.57 | 4.40 | 5% | 1.76 | 1.62 | 1.49 |
| 0% | 4.65 | 4.51 | 4.35 | 0% | 1.82 | 1.68 | 1.54 |
| -5% | 4.59 | 4.44 | 4.29 | -5% | 1.89 | 1.74 | 1.60 |

In Table 8, the masses $M_A$ of M87*-A and $M_B$ of M87*-B are presented as results of calculations using eqs.(5.6) and (5.7). We conclude that $M_A$ is $4.51^{+0.21}_{-0.22}$ $\times 10^9 M_\odot$; and $M_B$ is $(1.68\pm0.08)\times 10^9 M_\odot$. Based on the deduced orbiting radii and masses, the orbiting period T (in days) is calculated as shown in Table 9, where the shift angle of the binary positions after 369 d corresponds to the times between the EHT observation (M Image) and GMVA observation (L Image).

Table 9

Orbiting Period And Shift Angle

| T (day) | | | | Shift Angle (deg) | | | |
|---|---|---|---|---|---|---|---|
| | Distance | | | | Distance | | |
| Error | 17.6Mpc | 16.8Mpc | 16.0Mpc | Error | 17.6Mpc | 16.8Mpc | 16.0Mpc |
| 5% | 183.2 | 174.8 | 166.6 | 5% | 5.8 | 39.1 | 75.6 |
| 0% | 170.4 | 162.5 | 154.9 | 0% | 61.2 | 95.2 | 137.0 |
| -5% | 157.8 | 150.5 | 143.5 | -5% | 120.8 | 160.2 | 203.1 |

In Figure 22, each shift angle of M87*-A and of M87*-B between L image and M image is indicated to be $68^0$; this requires a constraint on the T values listed in Table 9, ranging from 143.5 d to 183.2 d. That is, for the case of counterclockwise orbiting motion, the following should be satisfied,

$$2T + \frac{68}{360}T = 369, \qquad (5.8)$$

that gives result, T=168.6 d as the required median period. Then, we can conclude that $T$=168.6± 2.0 d, referring to Table 9, where the case of T=170.4 d (0.2 s lower than the upper limit) corresponds to a shift angle of 61.2°(lower than 68° by 6.8°), and the case of T=166.6 d coincides with the lower limit with a shift angle of 75.6°, which is also close to 68°.

The orbital velocities of M87*-A and M87*-B, deduced from $r_A\cdot(2\pi/T)$ and $r_B\cdot(2\pi/T)$ are $(1.88\pm0.17)\times10^9$ cm/s and $(5.04\pm0.42)\times10^9$ cm/s, respectively. These velocities are (6.28±0.54)% of the speed of light for the M87*-A orbiting motion and (16.7±1.5)% of the speed of light for the M87*-B orbiting motion, indicating that these are indeed ECB-SMBH, similar to the case of Sgr A*, where the binary Gaa and Gab are moving at velocities of 16% and 21% of the speed of light, respectively [14]. In this proposed case of ECB-SMBH of M87*, it is also essential, as in the case of Sgr A*, that no gravitational waves are radiated from the supermassive BH binary system [19]. That is, if gravitational waves are radiated from the M87*-A and M87*-B binary system, they would merge within approximately 9 yr, following the estimation by Landau Lifshits [46] of orbit shrinkage caused by energy consumption due to radiation of the gravitational waves.

## 6. Discussion

### 6.1 Brief Review on No Gravitational Waves from ECB-SMBH

The proposal of the existence of ECB-SMBH is intrinsically linked to the assertion that gravitational waves are not generated by this system of supermassive black hole binaries. This concept was articulated by Oya in 2023 [19], stating, "No gravitational wave from orbiting supermassive Kerr black hole". The fundamental principle of this theory rests on the significant difference in internal mass density between supermassive black holes and those of stellar mass compact stars. The radius of the event horizon is directly proportional to the mass, while the volume within the event horizon scales cubically with mass, leading to extremely low average material densities within the event horizon as a function of the inverse square of the total mass.

Table 10. Average internal material density of ECB-SMBH.

| Member BH | Sgr A* | | M87* | | Assumed OJ287 Primary | |
|---|---|---|---|---|---|---|
| | Mass $(M_\odot)$ | Aver.Dens. g/cc | Mass $(M_\odot)$ | Aver.Dens. g/cc | Mass $(M_\odot)$ | Aver.Dens. g/cc |
| A | 2.20E+06 | 3.05E+04 | 4.51E+09 | 7.25E-03 | 9.15E+09 | 1.76E-03 |
| B | 1.97E+06 | 3.80E+04 | 1.68E+09 | 5.22E-02 | 9.15E+09 | 1.76E-03 |

For examples, we list the average internal material density of ECB-SMBH for three scenarios: Sgr A*, M87*, and the hypothesized case of OJ287, in Table 10. In all instances, we presume the maximum rotation for the Kerr BH, where the event horizon radius is half that of the Schwarzschild radius. Even in the case of Sgr A*, which exhibits relatively high density compared to other more massive cases, the internal densities are still exceedingly low compared to those of stellar mass BH, exemplified by a solar mass black hole at $1.84\times10^{16}$g/cc.

In the published theory, it is highlighted that these sparse materials, which adhere to classical physics, are not uniformly distributed inside the event horizon but are condensed into a compact core according to post Newtonian dynamics derived from the Einstein equation for observations transformed into coordinates that form a weak field condition. Consequently, we confirmed a scenario where the material within the event horizon is condensed into a compact region with a radius of 1/50 of the event horizon, leaving a vast empty space inside the supermassive Kerr BH through which generated gravitational waves could propagate. The publication [19]. explains how the propagation of gravitational waves ceases imposed by Kerr spacetime while propagating inside of the event horizon.

In Figure 23, we depict the internal mechanics of GW generation and propagation, as illustrated in Figure 13 of the original paper. This figure portrays one of BH of ECB-SMBH moving along binary orbits, forming quadrupole sources with its pair BH, thus potentially generating GWs. As detailed in the original publication, the generated GW propagate through the interior Kerr spacetime with velocity $V(t_{ob},r,\theta)$, as described by:

$$V(t_{ob},r,\theta) = cF\sqrt{\frac{\Delta}{\Sigma}}, \qquad (6.1)$$

where $t_{ob}$,r,and θ are the observation time, the radial distance with its origin at the center of the source material (see Figure 23), and the polar angle with its origin also set at the center of the inner material, respectively. The coordinate system depicted in Figure 23 is thus given by a polar coordinate system, which rotates in the azimuthal direction with the spin angular velocity Ω of the BH. In eq.(6.1), Δ and Σ are functions that express the Kerr spacetime, further defined by imposing the rotational constraint "a" with angular velocity $\Omega=d\varphi/dt$, with respect to the azimuthal angle φ; that is:

$$ds^2 = -\left\{\left(1-\frac{rr_g}{\Sigma}\right)+\frac{2carr_g\sin^2\theta}{\Sigma}\left(\frac{\Omega}{c}\right)-\left(r^2+a^2+\frac{a^2rr_g\sin^2\theta}{\Sigma}\right)\sin^2\theta\left(\frac{\Omega}{c}\right)^2\right\}c^2dt^2$$
$$+\frac{\Sigma}{\Delta}dr^2+\Sigma d\theta^2, \qquad (6.2)$$

where $\Delta=r^2-rr_g+a^2$ and $=r^2+a^2cos^2\theta$; $r_g=2GM/c^2$ and $a=J/M$ with respect to the gravitational constant $G$, the speed of light c, the black hole mass $M$, and the angular momentum of the Kerr black hole $J$. Consequently, the F value in eq.(6.1) is defined by:

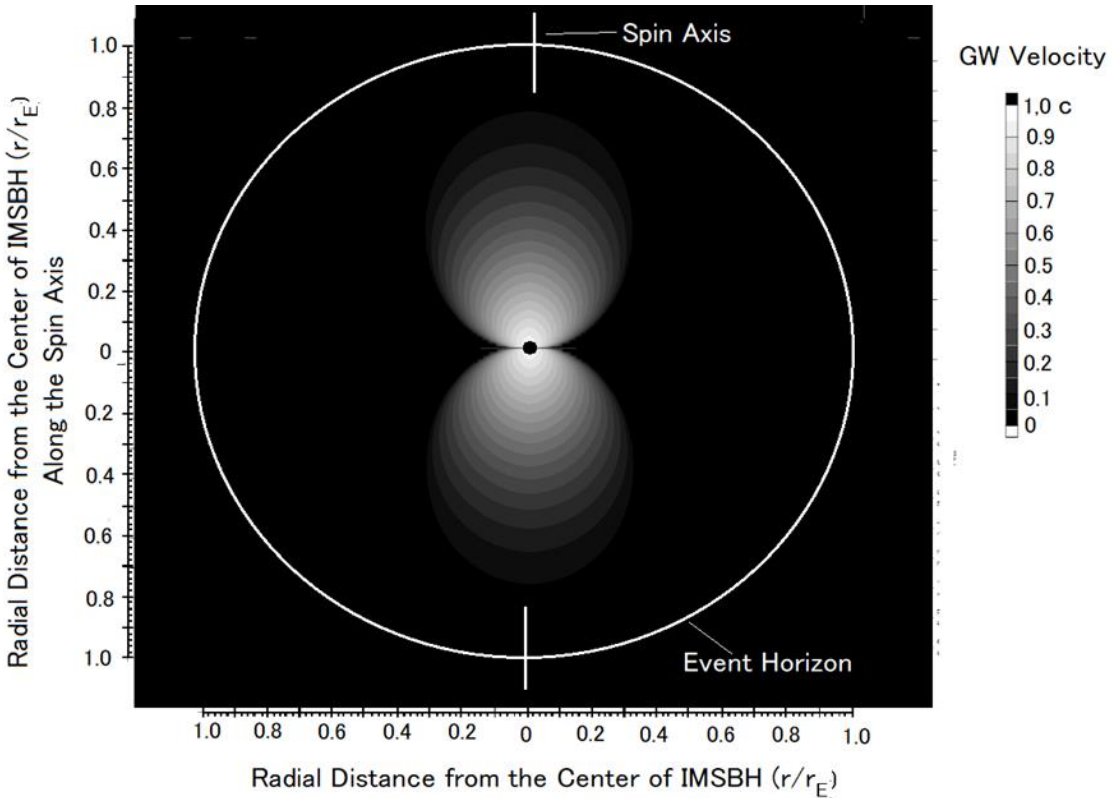


**Figure 23.** Calculated velocity of GW propagating in the interior region of Kerr BH. Results are given in $r$ - $\theta$ cross section, including spin axis for $A\Omega$= 8 (see Eq. (6.17) and Figure 13 in the original paper ), with SMBH radius $r_{Mc}/r_E$=1/50. The GW velocity is indicated as gray code, from pure white for light velocity to pure black for null velocity. The GWs that propagate radially in the direction of the polar angle $\theta$ cease to propagate at ($r_F$, $\theta_F$), corresponding to $F^2$=0 (see eq.(6.3)) before arriving at event horizon. (After Oya,[19])

$$F^2 = \left(1 - \frac{rr_g}{\Sigma}\right) + \frac{2carr_g\sin^2\theta}{\Sigma}\left(\frac{\Omega}{c}\right) - \left(r^2 + a^2 + \frac{a^2rr_g\sin^2\theta}{\Sigma}\right)\sin^2\theta\left(\frac{\Omega}{c}\right)^2. \qquad (6.3)$$

Following this, under a given spin condition with Ω, the generated GWs cease to propagate at points ($r_F$,$\theta_F$) where $F^2$=0, as outlined in eq.(6.1). These results are clearly indicated in Figure 23.

The GWs encountering the F zero point revert toward their starting points, associated with the initial phase; the returning and forwarding GWs interact to form standing waves at each encounter point. Thus, within the interior region of the Kerr BH, GWs are unable to transport energy away from the source. Thus, for supermassive BH systems, a model can be established in which generated GWs are not radiated outside the event horizon and do not disturb the orbital motion, even in the case of extremely close binaries.

### 6.2 Gravitational wave problem of OJ287

#### 6.2.1 Brief summary of research results

The blazar OJ287, recognized as an exemplary candidate for an active galactic nucleus (AGN) with a distance of z=0.3 (equivalent to 3.5 billion light years), has garnered significant interest from AGN researchers. This surge in studies includes pivotal works by Valtonen et al., [47] and Britzen et al., [48], published in 2018, which are directly relevant to the ongoing discourse.

The OJ287 features a binary system composed of primary BH with a mass of $1.835\times10^{10}M_{\odot}$ and secondary BH with a mass of $1.50\times10^{8}M_{\odot}$ , [47]. The secondary BH, which orbits the primary BH on an elliptical path with an eccentricity of 0.657 and a major axis length of approximately $10^4$ AU, is estimated to approach the peri primary BH region every 12 yr. This behavior is in a figure raising thought that the secondary is in an in spiral phase due to gravitational wave radiation ,[47, 48]. Valtonen et al.'s methodology for analyzing the quasi Keplerian orbit dynamics of the OJ287 binary system incorporates post Newtonian approximations for gravitational wave effects on orbital dynamics. Their model, which requires nine parameters, is refined by constraints derived from the timing of the secondary BH's approach, as indicated by V band light flares resulting from interactions with the primary BH's accretion disk (hereafter referred to as the Valtonen Model). With increasing chances of observations of OJ287's flares, the number of constraints up to 16, allow for a highly accurate solution to determine unknown parameters. Among the significant findings, it is reported that

the binary's orbital period of 12.062 yr, is decreasing by 38 d per century due to gravitational wave radiation. This implies that the OJ287 binary is on a trajectory toward merging within a timeframe not exceeding 10,000 yr.

Considering the broader context of confirming the existence of ECB-SMBH of the present work, the gravitational phenomena described here pose contradictions that necessitates a through re investigation of the gravitational wave aspects from foundational principles.

### 6.2.2 Fourier analyses of published historical light curve of OJ287

#### a) Fourier Analyses of historical v band data

To elucidate the period variation within the Valtonen Model, we reanalyzed the light curve data presented by the authors. Recognizing the essence of a flare as the moment of peak brightness, our analysis focused on identifying the maximum point on the light curve for each observational year.

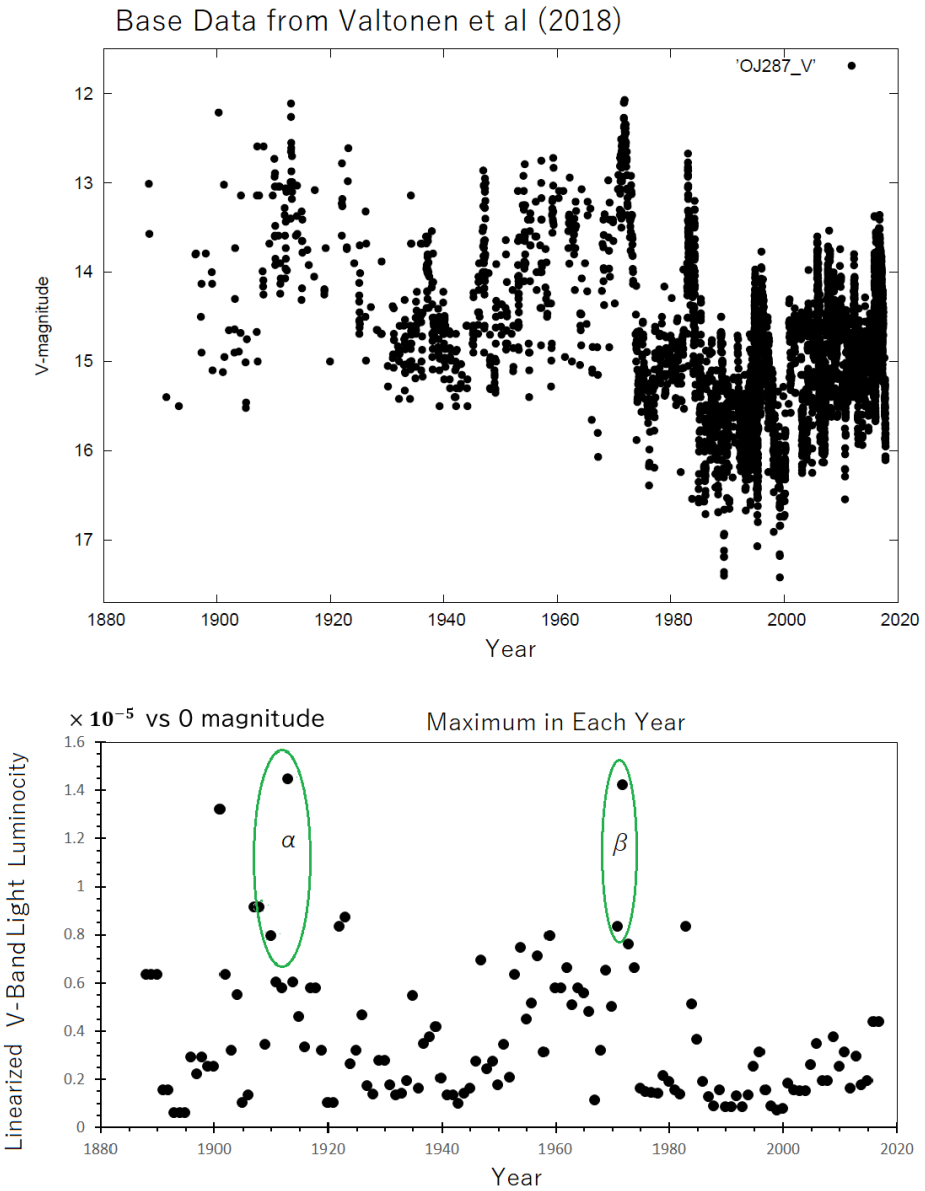


**Figure 24.** Historical light curve of OJ287 from Valtonen et al. publication [47] for V band with scale of magnitude (top panel) and selected maximum level in each year of observation interval with linearized scale of luminosity taking zero magnitude as unity (bottom panel). Two remarkable burst events marked by $\alpha$ and $\beta$ are discussed in main text relating to proposal of ECB-SMBH for primary BH.

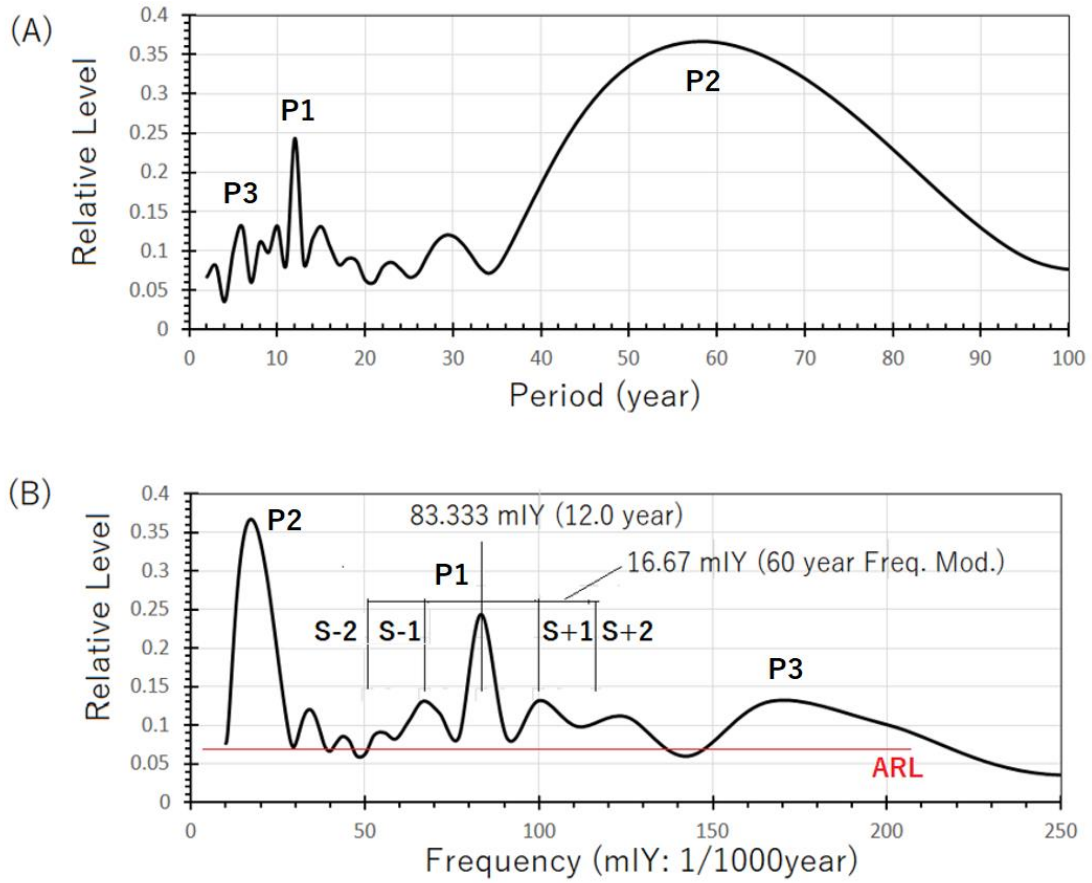


**Figure 25.** Results of the Fourier transformation for the time variations of V band light given as the linearized luminosity. In panel (A) the results are given as the function of the periods with unit of yr while the results are expressed as function of the frequency with the unit of the mIY (milli inverse year) which is defined, in the present study, as 1/(1000yr). ARL indicates average of the Fourier transformation of the random signal level. Remarkable peaks P1, P2 and P3 of the spectra are detailed in the main text.

In the bottom panel of Figure 24, we converted the luminosity of V band light from magnitude to linear luminosity. This transformation aims to achieve uniform sensitivity in Fourier transform functions for detecting occurrence periods. Figure 25 presents the outcomes of the Fourier transformation applied to the time variations of V band luminosity, linearized for analysis. In Panel (A), the results are depicted as functions of periods, with the unit of yr, while the results are expressed as a function of frequency, in panel (B), utilizing the unit milli inverse year (mIY), defined in this study as 1/(1000yr).

### b) General scope for understanding peaks of spectra seeking for the origin of the formation

For understanding peaks of spectra seeking for the origin of the peak formation, we opt a generalized formulation which represent the interaction of the secondary BH with accreting disk of the primary BH in occasions passing the peri primary BH region with the period of 12 yr, that is:

$$W_f = a_f \left\{1 + K_f cos\left[\int_{t_0}^{t} \omega_{orb}(t)dt + \Phi_f(t)\right]\right\} \cdot cos\left[\int_{t_0}^{t} \omega_{orb}(t)dt\right]. \qquad (6.4)$$

where $W_f$ is a model of radiated power of flares raised every recurrences of the secondary BH given by the last term , $cos\left[\int_{t_0}^{t} \omega_{orb}(t)dt\right]$ that is expressed using WKB approximation form for the orbiting angular frequency $\omega_{orb}(t)$ generalized to describe the time dependent variation of the orbiting period. This eq.(6.4) shows that the radiated power of flare $W_f$ caused by the encounter of the secondary BH with the primary BH's accreting disk is largely controlled by the form of the amplitude modulation $I_f$ that is given, by

$$I_f = a_f \left\{1 + K_f cos\left[\int_{t_0}^{t} \omega_{orb}(t)dt + \Phi_f(t)\right]\right\}. \qquad (6.5)$$

where $a_f$ and $K_f$ are constant to express the flare intensity as model; $\Phi_f(t)$ is phase function corresponding to the time shift between the occurrence of the flares and the passage of the secondary BH crossing the peri primary BH point. By this equation, we can express the raised flare intensity depending on the positions, of encounter of the secondary BH with accreting

disk of the primary BH, which is intrinsically function of relative phase angle $\int_{t_0}^{t}\omega_{orb}(t)dt+\Phi_f(t)$ of the concerning BHs. By rewriting eq.(6.4) after mathematical manipulation, we have the expression, as

$$W_f = a_f cos\left[\int_{t_0}^{t}\omega_{orb}(t)dt\right]+\frac{a_f K_f}{2}cos\left[\Phi_f(t)\right] + \frac{a_f K_f}{2}cos\left[2\int_{t_0}^{t}\omega_{orb}(t)dt+\Phi_f(t)\right]. \quad (6.6)$$

The three terms in the right hand side of above eq.(6.6) are correspond to the principal peaks labeled in the Fourier analyzed historical V band data given in Figure 25; the peaks P1, P2 and P3 given in Figure 25 in panels (A) and (B) correspond to the first, second and third terms, respectively, in the right hand side of eqs.(6.6).

### c) Frequency modulation on the orbital period of the secondary BH

The spectrum peak, P1 is one of the remarkable peaks at the periods 12 yr which is identified as same with peaks established through the current studies on the secondary BH orbiting motion in the OJ287. The point of P1peak attracting our notice is the existence of the side bands with a given frequency gaps corresponding to the period around 56 to 60yr. If $\omega_{orb}(t)$=$const$ in the first term of right hand side of eq(6.6), the peak should appear as a single peak reflecting $a_f\ cos$,[$\omega_{orb}t$]; though there exists errors caused by background noises, we cannot negate associated four side bands with constant intervals of frequency of about 16mIY (around 60yr) centered at the principal frequency of 83.333 mIY(12yr). Here we should take $\omega_{orb}(t)$ as time dependent function. As details are described in **Appendix E,** we realize that the orbiting period $T_{os}$ of the secondary BH is frequency modulated as,

$$T_{os} \approx T_0\left[1-\zeta cos\left(\frac{2\pi}{60}t\right)\right]. \quad (6.7)$$

where $T_0$ is the intrinsic orbiting period; and $\zeta$ is the modulation rate of the period variation.

In **Appendix E,** with the rewritten parameters $\omega_{0S}\equiv 2\pi/T_{0S}$,$p_{0S}\equiv 2\pi/60$,$and\ \xi_{0S}\equiv(2\pi/T_0)\cdot\zeta$.($see\ eq.(E3)$), the time varying function with frequency modulation of eq.(6.7), described in years, is expressed as follows:

$$\begin{aligned} f(t) = A\{&J_0(\xi_{0S}/p_{0S})cos(\omega_{0S}t-\theta_{0S})+J_1(\xi_{0S}/p_{0S})cos[(\omega_{0S}+p_{0S})t-\theta_{0S}] \\ &-J_1(\xi_{0S}/p_{0S})cos[(\omega_{0S}-p_{0S})t-\theta_{0S}] \\ &+J_2(\xi_{0S}/p_{0S})cos[(\omega_{0S}+2p_{0S})t-\theta_{0S}] \\ &+J_2(\xi_{0S}/p_{0S})cos[(\omega_{0S}-2p_{0S})t-\theta_{0S}]+\cdots\cdots\cdots\}. \end{aligned} \quad (6.8)$$

where A denotes an arbitrary constant; and $\theta_{0S}$ represents a constant phase angle, determined at the starting time $t_0$ as

$$\theta_{0S} = \omega_{0S}t_0+\frac{\xi_{0S}}{p_{0S}}sin(p_{0S}t)t_0. \quad (6.9)$$

As detailed in Appendix E through Fourier transformation analysis, we observe spectral peaks at the angular frequencies $\omega_{0S}-2p_{0S}$ with amplitude $J_2(\xi_{0S}/p_{0S})$, derived by the second order Bessel function of the first kind. Similarly, peaks are noted at $\omega_{0S}-p_{0S}$,$\omega_{0S}$, $\omega_{0S}+p_{0S}$,and $\omega_{0S}+2p_{0S}$ with amplitudes $J_1(\xi_{0S}/p_{0S})J_0(\xi_{0S}/p_{0S})$,$J_1(\xi_{0S}/p_{0S})$ and $J_2(\xi_{0S}/p_{0S})$, respectively. In Table 11, we have cataloged spectral peaks, comparing those detected from the historical record of OJ287 flares with theoretical predictions from eqs.(6.7) to eq.(6.9). As illustrated in Figure 24, both period and frequency expressions of the spectra coincide with a constant bias level of approximately 0.072, in terms of relative spectral value. This bias level, termed the ARL results from averaging spectral data related to random phenomena associated with the original events. Rather than considering this random component as an error, we recognize that the original light records consist of two components: one related to apparent periodic phenomena and the other to random emissive phenomena. Given that the spectra are derived from averaging 30 Fourier transformed functions, the random characteristic tends to stabilize, independent of the analyzed period or frequency. Consequently, we can exclude this component to focus on the periodic components. In Table 11, we present three cases of ARL subtraction, considering potential error to scale the displayed diagrams (see Table 11).

Table 11. Comparison of detected 83.333 mIY (12 yr period) spectra associated with sidebands with theoretical values.

| Side Bands | Relative Spectra Level | Ratio | ARL 0.0760 Case | ARL 0.0767 Case | ARL 0.0773 Case | Ratio | Argument of Bessel Function 0.61 | 0.62 | 0.63 | 0.64 | 0.65 |
|---|---|---|---|---|---|---|---|---|---|---|---|
| S-2 | 0.084 | S-2/C | 0.053 | 0.049 | 0.045 | $J_2/J_0$ | 0.0495 | 0.0513 | 0.0531 | 0.0549 | 0.0568 |
| S-1 | 0.130 | S-1/C | 0.323 | 0.320 | 0.318 | $J_1/J_0$ | 0.3201 | 0.3259 | 0.3317 | 0.3375 | 0.3434 |
| Center | 0.243 | C/C | 1.000 | 1.000 | 1.000 | $J_0/J_0$ | 1.000 | 1.000 | 1.000 | 1.000 | 1.000 |
| S+1 | 0.133 | S+1/C | 0.344 | 0.341 | 0.338 | $J_1/J_0$ | 0.3201 | 0.3259 | 0.3317 | 0.3375 | 0.3434 |
| S+2 | 0.095 | S+2/C | 0.118 | 0.115 | 0.111 | $J_2/J_0$ | 0.0495 | 0.0513 | 0.0531 | 0.0549 | 0.0568 |

The analysis of the detected spectra shows that the second sidebands, corresponding to the theoretical $J_2$ functions, align closely with the analytical limits set by reading errors and existing noise. However, the first sidebands, associated with the theoretical $J_1$ functions, exhibit discernible levels in terms of their ratio to the central peak level. Based on the results in Table 11, we infer that $\xi_{0S}/p_{0S}$=0.63±0.2. Consequently, the modulation rate $\zeta$ in eq.(6.4) equals (0.63±0.2)($T_0$/60). For an intrinsic orbital period $T_0$ of 12 yr, the rate of variation in the flare occurrence period is 0.126±0.04yr. This implies that the flare occurrence period, influenced by the secondary BH, oscillates between a maximum of (13.5±0.48) $yr$ and a minimum of (10.5±0.48)$yr$, showing sinusoidal variation over a cycle of58±1 yr.

Thus, we may consider the time interval when the orbiting period $T_{os}$ is in the 30 years of the decreasing phase; and we will meet the time interval during 30 years in future when the orbiting period enters in increasing phase. From this perspective, the results of the decreasing of the orbital period pointed out by Valtonen model cannot take as permanent nature as their proposal of gravitational wave generation model.

### 6.2.3 Possibility of ECB-SMBH as Primary BH

#### a) Necessity of requirement of another binary system alternative to Primary BH

Regarding the evidence of the oscillating period of flare occurrence discussed in Subsection 6.2.2, we investigate the possibility of ECB-SMBH system as an alternative to the traditional concept of the primary BH being a single SMBH, as currently assumed in all studies. This alternative ECB-SMBH concept suggests that the oscillation in the encounter period of the secondary BH with the accretion disk of the primary BH is not solely attributable to the precession of the secondary BH orbit. Instead, it includes the variation effects of the gravitational force in the peri primary BH region, which fluctuates depending on the mutual configuration of the three bodies (as illustrated in Figure 26). This implies that the configuration periodically repeats, combining the secondary BH's orbiting period.

#### b) Orbiting parameters of ECB-SMBH given as alternative of primary BH

Before delving into the dynamics to clarify the variation in the orbital period of the secondary BH, we explore the relationship between the assumed orbiting characteristics of ECB-SMBH system and the pericenter passage of the secondary BH. As illustrated in Figure 26, we define an angle, Φ (radian) between the direction of the radial vector of the secondary BH and the vector direction connecting the member BHs temporarily named EA and EB, of the ECB-SMBH system, For this case, Φ is expressed by:

$$\Phi = \left(\frac{2\pi}{\pm T_E}\right) T_{orb} - \frac{T_{orb}}{12}\left(\frac{38.7}{180}\right)\pi. \qquad (6.10)$$

where± $T_E$ and $T_{orb}$ represent the orbiting periods of the ECB-SMBH and the secondary BH, respectively. We choose + $T_E$ for the case where the ECB-SMBH and the secondary BH rotate in the same sense, and $T_E$ for the scenario where they rotate in opposite senses. Drawing from the historical records of OJ287 flares [47], we recognize the need for recurrences in the mutual relationships of

**Table 12.** Calculated orbiting peri od of ECB-SMBH (unit; yr),

| N | Recurrence Period 56 yr s.s. | 56 yr a.s | 58 yr s.s. | 58 yr a.s | 60 yr s.s. | 60 yr a.s |
|---|---|---|---|---|---|---|
| 35 | 1.577 | 1.623 | 1.633 | 1.682 | 1.688 | 1.741 |
| 36 | 1.534 | 1.578 | 1.588 | 1.635 | 1.642 | 1.692 |
| 37 | 1.493 | 1.534 | 1.546 | 1.59 | 1.598 | 1.646 |
| 38 | 1.454 | 1.493 | 1.506 | 1.547 | 1.557 | 1.602 |
| 39 | 1.418 | 1.455 | 1.468 | 1.507 | 1.518 | 1.56 |
| 40 | 1.383 | 1.418 | 1.431 | 1.469 | 1.48 | 1.52 |

s.s. Same Orbiting Sense  a.s Counter Orbiting Sense

three BHs with a period of $5T_{orb}$, which imposes a constraint on eq.(6.10) as follows:

$$\pm 2\pi N = \sum_{i=1}^{5}\left[\left(\pm\frac{2\pi}{T_E}\right) - \frac{\pi}{12}\left(\frac{38.7}{180}\right)\right]T_i. \qquad (6.11)$$

where N is an arbitrary integer, $T_i$ corresponds to $T_{orb}$ in eq.(6.10) for the i th rotation interval of the second BH's orbiting motion. The calculated orbiting periods of ECB-SMBH are presented in Table 12, where the $T_E$ values are provided in years, following eq.(6.11), for the N range from 35 to 40, across three cases of $\Sigma T_i$.

The current results from VLBI observations of the OJ287 jet [48] reveal a time variation in the structure. Notably, the analysis of the jet structure by Britzen et al. [48], based on VLBI observation data at 4.8, 8.0, and 14.5 GHz, identified the presession of the jet with a period of 27±5 yr. A significant result relevant to this work is the confirmed presence of clear nutation, associated with the presession, displaying a period of 1.6±0.1yr. As the source of this nutation effect on the twisting jet, we postulate that the orbital motions of the ECB-SMBH, as an alternative to the primary BH, might supply ample energy through possible electromagnetic dynamics, leading to the rapid movement of plasma as jets at sub light velocity. In this context, Table 12 includes the recurrence period of 58 yr with N=37 showing a 1.59 yr period of ECB-SMBH for counter rotation, and a recurrence period of 60 yr for a 1.598 yr period (at N=37) for corotation and a 1.602 yr period (at N=38) for counter rotation of the ECB-SMBH orbiting motion.

**Table 13.** Parameters of EA and EB of ECB-SMBH as Alternative of The Primary BH of OJ287

| Mass Ratio | Mass ( ◉ ) | | Orbit Radius (AU) | | Velocity Rate | |
|---|---|---|---|---|---|---|
| $M_B/M_A$ | $M_A$ | $M_B$ | $r_A$ | $r_B$ | $v_A/c$ | $v_B/c$ |
| 0.1 | 1.66 E+10 | 1.66 E+09 | 327 | 3276 | 0.02 | 0.203 |
| 0.2 | 1.52 E+10 | 3.05 E+09 | 600 | 3003 | 0.037 | 0.186 |
| 0.3 | 1.40 E+10 | 4.22 E+09 | 831 | 2772 | 0.051 | 0.172 |
| 0.4 | 1.30 E+10 | 5.22 E+09 | 1029 | 2574 | 0.063 | 0.159 |
| 0.5 | 1.22 E+10 | 6.10 E+09 | 1201 | 2402 | 0.074 | 0.149 |
| 0.6 | 1.14 E+10 | 6.86 E+09 | 1351 | 2252 | 0.083 | 0.139 |
| 0.7 | 1.07 E+10 | 7.53 E+09 | 1483 | 2120 | 0.092 | 0.131 |
| 0.8 | 1.01 E+10 | 8.13 E+09 | 1601 | 2002 | 0.099 | 0.124 |
| 0.9 | 9.63 E+09 | 8.66 E+09 | 1706 | 1897 | 0.106 | 0.117 |
| 1 | 9.15 E+09 | 9.15 E+09 | 1801 | 1802 | 0.111 | 0.111 |

Considering the period range, we can apply the Keplerian relationship based on Newtonian dynamics to describe the orbit size of the proposed ECB-SMBH using the same equations from eqs.(5.4) to (5.7), which are applied to the case of ECB -SMBH of M87*. Assuming a circular orbit and defining the masses as $M_A$ and $M_B$ respectively for EA-BH and EB-H of the ECB-SMBH as an alternative to the OJ287 primary BH, and defining the orbit radii as $r_A$ and $r_B$, respectively for EA-BH and EB-BH, with mass ratio $\kappa_{0J}=M_B/M_A$,we can estimate, that $M_A=1.835\times10^{10}M_{\odot}/(1+\kappa_{0J})$,$M_B=1.835\times10^{10}M_{\odot}\times\kappa_{0J}/(1+\kappa_{0J})$, $r_A=5.40\times10^{16}\times\kappa_{0J}/(1+\kappa_{0J})$ cm, and $r_B=5.40\times10^{16}/(1+\kappa_{0J})$ cm. The orbiting velocities are then estimated as $0.222c\times\kappa_{0J}/(1+\kappa_{0J})$and $0.222c/(1+\kappa_{0J})$, respectively for EA-BH and EB-BH. This reveals that the proposed ECB-SMBH, is analogous in term of moving velocities, proposed for Sgr A* and M87*. In Table 13, we see examples of masses, orbiting radii and orbital velocities of the member BH of ECB-SMBH for ten cases of the mass ratio.

### 6.2.4 Time variations of flare occurrences associated with secondary BH interacting with accretion disks of ECB-SMBH

#### (a) P2 effects

In the Panel (A), of Figure 25, we observe spectral peaks P2 around 58±1 yr, that is represented by the second terms of the right hand side of the interaction model equation eq.(6.6) , $(a_f K_f/2)cos\,[\Phi_f(t)]$ where $\Phi_f(t)$ is the phase function (see eq.(6.5)) corresponding to the time shift to the encounter of the secondary BH with the primary BH's accretion disc. We rewrite for the case of the proposed ECB-SMBH, considering eqs.(6.10) and (6.11) , as

$$\Phi_f(t) = 2\pi\left[\left(\frac{1}{\pm T_E}\right) - \frac{1}{24}\left(\frac{38.7}{180}\right)\right]t. \qquad (6.12)$$

In addition to the secondary BH orbital period of 12 yr, the Valtonen Model highlights a periodic variation affected by the significant presession of the secondary BH, attributed to the effects of general relativity near the peri primary BH. According to the Valtonen Model, with each peri primary passage, the precession angle accumulates by 38.7°, causing the ellipse's axis to rotate 180°with 56 yr period. For this context we take the effect of the pression of GR effect in Valtonen Model significant

as given in eqs, (6.10)~(6.12).

With respective to the P2 peak of spectra in Figure 25, the 56yr period expected by the Valtonen Model is not necessarily remarkable, there is a noticeable spread in the spectra around the 58 yr peak, ranging from 56 to 60 yr. At this stage, we are required to investigate whether the observed frequency modulation has relation to the precession of the secondary BH or not. A critical aspect of this inquiry is encapsulated in the expression for the frequency modulation, as:

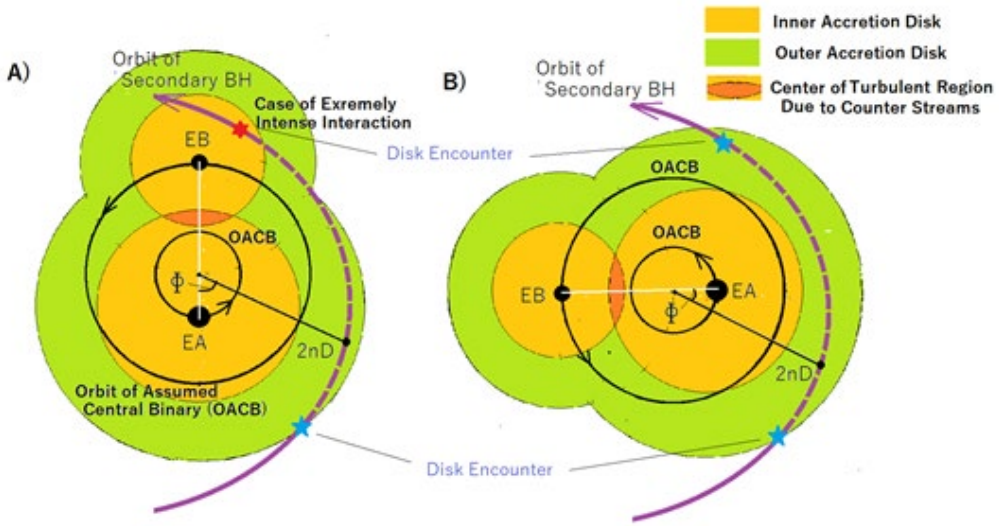


**Figure 26.** Qualitative configuration of the three BHs orbits at the center region of OJ287 .
The secondary BH passes through the two accreting disks associated with the ECB-SMBH proposed as alternative to the single primary BH ; depending on the geometrical relation of the secondary BH between the ECB-SMBH whose orbiting positions are represented by the white line which connects EA-BH and EB-BH of the ECB-SMBH, occurrences of the flares raised by accreting disk encounter of the secondary BH change features as function of the thickness and density (simply expressed by two grades as Inner and Outer Accretion Disks) of the accreting disks of the member BHs of ECB-SMBH. Angle Φ is defined between the direction of the connection line of orbiting BHs of ECB-SMBH and the direction of the position vector of the secondary BH at the peri-center of the secondary BH's orbit given by 2nD. In Panel (A) the case of asymmetrical disk encounters (corresponding to the cases of α and β in the historical records given in Figure 24 ,from the qualitative perspective) is indicated ; after the first encounter passing through the relatively tenuous plasma disk , the secondary BH encounters thick and dens accreting disk taking a close path to EB- BH of ECB-SMBH where the large flare takes place in the occasion of second encounter. Panel B shows the case of the encounters of the secondary BH with relatively tenuous accreting disks of ECB-SMBH causing flares of almost equal intensities in a medium range for twice encounters . In both Panels (A) and (B), orbits of ECB-SMBH are expressed by OACB both for EA-BH and EB-BH of ECB-SMBH.

$$f(t) = A\cos\left(\int_{t_0}^{t}\frac{2\pi}{T_{os}}dt\right) = A\cos\left[\int_{t_0}^{t}\frac{2\pi}{T_0}\left(1+\zeta\cos\left(\frac{2\pi}{60}\right)t\right)dt\right] . \qquad (6.13)$$

When we denote the timing of the accretion disk crossing for the m time as $t_m$, the crossing time can be expressed as a time shift from the peri primary BH passage, resulting in the function as follows:

$$f(t\pm\Delta t) = A\cos\left(\int_{t_0}^{t\pm\Delta t}\frac{2\pi}{T_{os}}dt\right) = A\cos\left(\int_{t_0}^{t}\frac{2\pi}{T_{os}}dt \pm \frac{2\pi}{T_{os}}\Delta t\right). \qquad (6.14)$$

where $\Delta t$ represents the time shift necessary for the encounter with the accreting disk to occur after passing the peri primary BH point, thus $t_m = t+\Delta t$. Comparing eqs.(6.13) and (6.14), we can apply a well established mathematical relationship for Fourier transformation, as

$$\left|\int_{-\infty}^{\infty}\cos(\omega t)e^{-i\omega t}dt\right| = \left|\int_{-\infty}^{\infty}\cos(\omega t+\Phi_m)e^{-i\omega t}dt\right|. \qquad (6.15)$$

where $\Phi_m$ represents the phase shift angle $\pm 2\pi\Delta t/T_{os}$ representing the m th time crossing of the accretion disk of the primary BH; the periodic recurrence of the secondary BH is modeled by a simple cosine function. Consequently, we deduce that the

variation in flare occurrence timing, driven by the encounters of the secondary BH with the accretion disk and a precession angle of 38.7°per pericenter passage, does not induce frequency modulation on the orbital period of the secondary BH around the primary BH.

Then from perspective to consider the ECB-SMBH as alternative of the single primary BH we have investigated the recurrency of the phase $\Phi_f(t)$ given by eq.(6.12) with the frequency modulated orbiting period of the secondary BH, that is given by

$$T_{os} = T_0\left[1 + 0.126 \cdot cos\left(\frac{2\pi}{60}t + \frac{2\pi}{5}\right)\right]. \qquad (6.16)$$

The results show that the configuration formed by three BHs recures within period range from 56yr to 60yr centered at 58yr in the case of counter sense of orbiting motion between the orbiting sense of ECB-SMBH and the orbiting sense of the secondary BH.

### (b) P3 peaks in the analyzed spectra

As effects of the occurrence of the flare caused by the encounter of the secondary BH with the ECB-SMBH, alternative primary BH, the P3 peaks corresponding to the third term of the right hand side of eq.(6.6) is revealed principally around half period (twice frequency) of the orbital period as given in panel (B) of Figure 25 that is, $(a_f K_f/2)\cdot cos(2\int^{t}_{t_0}\omega_{orb}(t)dt+\Phi_f(t))$. Because of time dependent phase $\Phi_f(t)$ and frequency modulation in $\omega_{orb}(t)$ the shape of spectra is spread widely around 166 mIY (6yr).

### c) ECB-SMBH effects

It is naturally thought by proposal of the ECB-SMBH that the configuration of the accreting disk where the secondary BH encounters in the periods of peri center region passage, changes asymmetrically depending on orbital motion of the member BH of ECB-SMBH as depicted in Figure 26 by Panel (A) and Panel(B). Therefore the timing of the encounter of secondary BH with accretion disks of ECB-SMBH and intensities of caused flares at the encounter time largely affected by the angle $\Phi_S$ ,i.e., the positions of the member of the central binary. (see Figure 26). The case of Panel (B) represents the usual time of occurrence of flare levels in historical records where the difference of intensities between two accretion disks crossing is not so large. On the other hand, we see the case given in the panel (A), of Figure 26, where a qualitative image of the configuration of three BHs which shows the inhomogeneous state of the accretion disk surrounding the ECB-SMBH is depicted. The first encounter of primary BH occurs with tenuous state of the disk while the returning encounter takes place in the thick disk which can be expected to radiate more intense emissions than the first case. As applicable cases of this asymmetrical flare occurrences, we see in Bottom Panel of Figure 24, where two cases of the remarkable flare of light emissions are picked up with notes α and β from the historical records of V Band emissions. What we making notice especially in these phenomena is the 58±0.3 yr interval, of occurrence, when the same mutual configurations of the triple BH had possibly taken place.

### 6.3 Summary on OJ287 ECB-SMBH

The suggestion of ECB-SMBH as an essential subject, aligning with the study results for Sgr A* and M87* to ensure the condition of no gravitational wave emission from supermassive BHs, looks presenting contradictory issue against current interpretations of the historical records of V band flares from OJ287. However, detailed analyses of the flare occurrence of OJ287 reveal that there is evidence of the periodical variation (frequency modulation) on the orbital period of the secondary BH orbiting around the primary BH. As the most plausible candidate to result the periodic modulation on the second BH's orbiting period, we present the proposal of ECB-SMBH as an alternative to the primary BH of OJ287.

However, it is significant that we investigate whether there remain rooms which strengthen or newly present subjects in current established knowledge of OJ287 system or not. For these matters, we have four subjects given as follows.

1) The interpretation of the extraordinary large flares in 1913 and 1972 (as shown in Figure 24 marked by $\alpha$ and $\beta$)

These unique instances of accretion disk crossing by the secondary BH, occurring only twice with an interval of 58±0.3 yr, cannot be explained by a single rotating BH for the primary, surrounded by a rotationally symmetrical configuration of the accretion disk (see Figure 26). Such a model does not account for the special enhancement of intensity from the disk encounter of the secondary BH due to simple geometric changes from orbital presession. Instead, an extraordinarily asymmetrical configuration of the accretion disk (see Figure 26), as proposed for the ECB- SMBH, can satisfy the required asymmetry and explain these special encounters.

2) The recurrence interval of flare occurrences in the OJ287 system is closer to 58 yr rather than 56 yr.

As the main cause of flare recurrence in the OJ287 system, current understanding, as represented by the Valtonen Model, highlights the effects of the secondary BH's precession in the pericenter region. This model considers no ECB-SMBH effect, and with eq.(6.11) and rotational symmetry with $N$=1/2, it follows that:

$$1 = \sum_{i=1}^{5}\frac{1}{12}\left(\frac{38.7}{180}\right)T_i, \qquad (6.17)$$

where $T_i$ is thought as constant in Valtonen Model, giving $5T_i \approx 56$. However, as noted in relation to Figure 25, Panel (A), the 56 yr peak is not distinctly marked but falls within a higher level period range associated with spectral peak at 58 yr, indicating significant relevance in the ECB-SMBH model. We propose that eq.(6.11), supported by observational results, offers a more accurate description of the recurrence configuration related to light outbursts associated with accretion disk encounters than does eq.(6.17).

3) Interpretation of cause of the nutation of the jet

The nutation of the jet, originating from periodic rotational phenomena with a period of 1.6±0.1 $y_r$, is naturally explained by the presence of an ECB-SMBH. Its orbiting period aligns with the oscillation period of the observed jet structure's nutation detected by radio waves. This nutation period is significantly different from the spin period of a single BH, which would not exceed 5 h per rotation.

4) Observation chance in case of gravitational wave radiation from OJ287

An often overlooked consideration is the likelihood of detecting the end stage phenomena, especially when the remnant cannot be observed. The theory that allows for gravitational wave generation suggests the merger timing of the OJ287 system to be no more than 10,000 yr in the future, within a potential total lifetime ranging from $10^9$ to $10^{10}$ yr. This implies we are currently witnessing an extremely rare event, with probabilities ranging from $10^{-5}$ to $10^{-6}$. Therefore, we consider the model that accounts for gravitational wave generation for OJ287 to be observing a miraculous event, rather than witnessing effects indicative of an ECB-SMBH existing under the premise of no gravitational waves from the SMBH.

## 7. Conclusion

Based on observations of decameter wavelength radio wave pulses from Sgr A* at 21.86 MHz, we have concluded the existence of the extreme central binary of the super massive black hole (ECB-SMBH) at the center of the Milky Way Galaxy. The system consists of SMBHs with masses $2.27\times10^6 M_\odot$ and $1.94\times10^6 M_\odot$, orbiting each other at a mutual distance of $4.1\times10^{12}$ cm a period of 2200±50 s. The orbiting velocities are 18% and 22% of the speed of light, respectively [14]. The existence of ECB-SMBH is contingent upon a physical scenario where no gravitational waves are radiated from these supermassive black holes [19]. The primary goal of this work is to confirm the existence of ECB-SMBH at Sgr A*. Following this confirmation, opportunities arise to search for evidence of ECB-SMBH in M87* and further in the blazar OJ287, as part of a broader effort to identify existing ECB-SMBHs orbiting at the centers of galaxies at sub light velocities and an extremely close mutual distances, on the order of a few to several ten times the radius of the event horizon of the supermassive Kerr BH.

### 7.1 Case of Sgr A*

We have performed the confirmation of the existence of ECB-SMBH through a comparison of the constructed ECB-SMBH model, based on decameter radio wave pulse observations, with publicly released VLBI data observed by Event Horizon Telescope Collaboration (EHTC). The results revealed 1.3 mm radio wave emissions with a definitive periodic component at Sgr A*, where the observed EHT visibilities closely match the model visibilities with a period of 2193±27 s [29]. Using this period as a starting point, we aim to visualize ECB-SMBH from the observed visibilities provided by EHTC in the present work. Given the previous work's conclusion [29] that the orbit plane of the possible ECB-SMBH is nearly parallel to the Galactic equator and observable as a one dimensional line inclined by 58°with respect to the right ascension line, we adopt an approximation method in our one dimensional analysis to construct the radio source structure along the orbiting line of interest. We then formed a one dimensional visibility, focusing on the orbital line from the EHT visibility data, termed the linearized visibility (LV), where EHT visibility data in the (u, v) plane are transformed into visibilities in the $(\ell,\tilde{t})$ coordinate; here, $\ell$ axis aligns with the ECB-SMBH orbiting line. The LVs are formed selecting visibility data along $\ell$ within a fan shaped zone with an open angle of ±39°along $\ell$ (the orbit line). Data with $(\ell,\tilde{t})$ coordinates outside the defined fan shape are discarded as unrelated to the orbital motion.

This LV is particularly characterized by time dependent data, unlike typical VLBI work where data are considered essentially static with only random noise oscillations. Therefore, we selected specific timings to collect visibility data at fixed phases in the orbiting period to track the periodic movement of radio wave sources. Since the radio wave sources from regions surrounding the black holes move along orbits observable as a line, these sources exhibit back and forth motions, crossing at the eclipse phase in the middle of the orbit. We set eight phases for half of the orbiting period of ECB-SMBH, assuming symmetry for simplicity; this assumption means the processes of the sources' back and forth movement are repeated within half of the orbiting period. The most significant parameter for accurately stacking data for each phase bin is the orbital period. Although we started with 2193±27 s as the orbiting period for data stacking, the results find a smooth continuation of the ECB-SMBH movement at 2153 ±5 s. This period closely aligns with the value of 2150±2.5 s from our previous study [28], which was deduced from the comparison of decameter radio wave pulse results with 1.3 mm VLBI observations reported by Fish et al. [27].

The linearized visibility of the EHT data, referred to as phase stacking data, has clearly indicated different functions of LV versus $\ell$ at a level significantly higher than the observational errors. This reveals the apparent feature of the periodic movement of the sources. The obtained LV, sorted into eight bins corresponding to the eight phases, is used to trace the movements of radio wave sources. These are compared with calculated visibilities formed via the Fourier transformation of binary sources moving back and forth along their orbital lines. This comparison shows sufficient accuracy to confirm coincidence in the $\ell$range from 2.5 Gλ to 5.5 Gλ, corresponding to a visible angle of 10 to $34\mu as$(equivalent to $10^{12}$~$4\times10^{12}$ cm at Sgr A∗), thus successfully confirming the existence of ECB -SMBH from the VLBI data provided by EHTC. We utilized the data of observation cases on April 6, 2017, for two data series: 96 Hi CASA and 96 Lo HOPS. In cases of these series data

observed on April 7 (97 day), the original EHT visibility data do not provide a sufficient number of data points along the ℓ axis when transforming the visibility data from the original (u, v) plane to the $(\ell,\tilde{t})$ plane.

The results of the recovered image of the moving ECB-SMBH indicate that the BHs are surrounded by bright zones of radio wave radiation; radii of these zones are 3 to 4 times wider than the radii of the event horizons of the host BHs. To recover the moving images of ECB-SMBH, we identified the brightness and associated background emissions from the coincidence of the theoretical LV (T-LV) and detected LV (E-LV). Investigating the brightness variation of the image as a function of the data stacking phase sequence number, we noticed some portions suddenly appear darker than neighboring phases; we consider this effect an artifact caused by a slight mismatch in the selected period between the actual ECB-SMBH period. The correction of this discrepancy is deferred to future work to achieve higher accuracy in determining the ECB-SMBH orbiting period.

### 7.2 Case of M87*

Regarding the two published radio wave images of M87* resulting from millimeter wavelength VLBI observation data [20,31], we have concluded that the two bright spots indicated in each image are manifestations of ECB-SMBH at the center of the M87 galaxy. This conclusion is based on the criteria established by our study on ECB-SMBH at Sgr A*, although the authors of the original images did not consider these spots to represent BH. Furthermore, we consider the single image of EHTC [21] to be out of scope, although its relation is discussed in Lu et al.'s paper [31], due to previous indications [20] of erroneous procedures in forming the M87* image from the EHT data. A significant point of the criteria obtained from our study on ECB-SMBH at Sgr A* is that the radio image of the BH is a continuous bright zone without any shadow or associated with inhomogeneous rings. This is attributed to the plasma environment around the binary, where the accretion disk becomes thick due to the effective reduction of angular momentum in the region of counter streams pervading around the center region of the two orbiting BHs.

For the four bright spots in two images that are mutually identified as the same two spots, we have temporarily named them M87*-A and M87*-B, considering them as member BH of ECB-SMBH. By fitting assumed circular orbits (observed as ellipses because of the viewing angle of the orbital plane) to all four spots in the published image, it is concluded that M87*A and M87*B are on orbits with radii of $4.37^{+0.44}_{-0.42}\times10^{15}$ cm and radius of $1.16^{+0.12}_{-0.10}\times10^{16}$ cm, respectively, assuming the distance of M87* to be 16.8±0.8 Mpc. Considering the extent of the orbit sizes, we apply Keplerian orbits under Newtonian dynamics to this binary system, yielding a mass ratio of M87*A and M87*B as a function of the corresponding orbit radii; the masses are calculated to be $4.51^{+0.21}_{-0.22}\times10^{9}M_{\odot}$ and $(1.68\pm0.08)\times10^{9}M_{\odot}$, respectively, for M87*A and M87*B. Given the time interval of 369 d between the two observations corresponding to the two images, which resulted in a 68° shift in the mutual orbital positions of each BH, the orbiting period of ECB-SMBH is decided to be 168.6± 2.0 d.

The orbital velocities deduced from the clarified angular velocity are (6.28±0.54)% of the speed of light for M87*-A and (16.7±1.5)% of the speed of light for M87*-B. These results reveal that M87* consists of an ECB- SMBH, scaling up approximately 1500 times in mass and 4000 times in orbit radii compared to the case of Sgr A*, where the binary BH Gaa and Gab are moving at speeds of 16% and 21% of the speed of light, respectively [14].

### 7.3 Case of OJ287

We have examined the blazar OJ287 from the perspective of gravitational wave radiation, addressing the critical issue of the potential negation of the existence of ECB-SMBH if the current description that the OJ287 binary system is already in the in spiral phase due to gravitational wave emission is accurate. To investigate the reality of gravitational wave effects, we have reviewed published historical records, as given in Subsection 6.2.2, primarily referring to two works by Valtonen [47] and Britzen [48]. The results of the Fourier analysis of the historical records, of the V band light luminosity[47], which show flares coinciding with the secondary BH's encounter with the accreting disk in the peri primary BH zone, clarify that the orbiting periods of the secondary BH periodically vary with an about 60 year cycle. We infer that the conclusion of shrinking orbital periods of the secondary BH, based on the last 30 yr of flare data, accidentally aligns with the orbiting period in the shrinking phase of its oscillating period.

From the perspective of ECB-SMBH, we postulate the existence of an ECB-SMBH that causes frequency modulation on the secondary BH's orbiting period at the center of the OJ287 as an alternative to a single primary BH with a mass of $1.835\times10^{10}$ $M_{\odot}$. Although detailed numerical analyses are reserved for future work, we preliminarily consider that the 60 yr period modulation on the secondary BH's orbit occurs with a 58~60 yr cycle repetition of the mutual configuration of the triple BH system (the secondary BH and two components of ECB-SMBH) in the region of the peri primary BH. To verify this concept, we have calculated the orbiting period of the proposed ECB-SMBH, consisting of member BH temporarily named A BH and B BH. From the constraint of the 58~60 yr repetition, 20 cases of possible periods ranging from 1.10 to 1.68 yr are identified. The results of Britzen et al., which indicated the existence of precession motion of the jet with a period of 27±5 yr, associated with clear nutation showing a period of 1.6±0.1 yr. This nutation could be generated in the source region of the jet, where intense electromagnetic processes actively accelerate the ambient plasma, drawing energy from the orbiting ECB-SMBH. We consider that the revealed nutation period is a manifestation of the orbiting period of the underlying ECB-SMBH in the core of OJ287. From the 20 candidates for the calculated period of ECB-SMBH for OJ287, we have selected a period of 1.59~1.60 yr. Using this period, other related parameters are deduced as given in Subsection 6.2.2(b); we then recognize that the binary BH is highly likely to be the ECB-SMBH which we have studied starting from the cases of Sgr A* via the case of M87*.

### Acknowledgment

The present research has been accomplished in the science

department of the graduate school of Tohoku University. The author is grateful to Prof. Y. Katoh, Dr. A. Kumamoto, for their interest and valuable discussions regarding the present work.

Financial support to continue the present work was provided with deep understanding of the standpoint of the present work. The author thanks President Y. Miyazawa and Executive Leader Mr. R, Hasuda of the Seisa Group and Former President of Seisa University, Mr. H. Inoue.

## References

1. Ghez, A. M., Duchêne, G., Matthews, K., Hornstein, S. D., Tanner, A., Larkin, J., ... & McLean, I. (2003). The first measurement of spectral lines in a short-period star bound to the Galaxy's central black hole: a paradox of youth. *The Astrophysical Journal, 586*, L127.
2. Eisenhauer, F., Genzel, R., Alexander, T., Abuter, R., Paumard, T., Ott, T., ... & Zucker, S. (2005). SINFONI in the galactic center: young stars and infrared flares in the central light-month. *The Astrophysical Journal, 628,* 246.
3. Gillessen, S., Eisenhauer, F., Trippe, S., Alexander, T., Genzel, R., Martins, F., & Ott, T. (2009). Monitoring stellar orbits around the massive black hole in the galactic center. *The Astrophysical Journal, 692*, 1075.
4. Genzel, R., Eisenhauer, F., & Gillessen, S. (2010). The galactic center massive black hole and nuclear star cluster. *Reviews of Modern Physics, 82,* 3121.
5. Gillessen, S., Plewa, P. M., Eisenhauer, F., Sari, R. E., Waisberg, I., Habibi, M., ... & Genzel, R. (2017). An update on monitoring stellar orbits in the galactic center. *The Astrophysical Journal, 837,* 30.
6. Fish, V. L., Johnson, M. D., Lu, R. S., Doeleman, S. S., Bouman, K. L., Zoran, D., ... & Vertatschitsch, L. E. (2014). Imaging an event horizon: mitigation of scattering toward Sagittarius A. *The Astrophysical Journal, 795*, 134.
7. Fish, V. L., Johnson, M. D., Doeleman, S. S., Broderick, A. E., Psaltis, D., Lu, R. S., ... & Ziurys, L. M. (2016). Persistent asymmetric structure of Sagittarius A* on event horizon scales. *The Astrophysical Journal, 820,* 90.
8. Event Horizon Telescope Collaboration; Akiyama,K., Alberdi,A.,Algaba,J.C.,Anantua,R., Asada,K., Azulay,R.,Bach,U., Baczko ,A-K.,Mislav Baloković,M., John Barrett, J.….& Zeballos,M.(2022). First Sagittarius A* event horizon telescope results. I. The shadow of the supermassive black hole in the center of the Milky Way, *The Astrophysical Journal Letters, 930*, L12
9. Event Horizon Telescope Collaboration; Akiyama, K., Alberdi, A., Alef, W., Algaba, J. C., Anantua, R., Asada, K., ... & Wouterloot, J.G.A. (2022). First Sagittarius A* event horizon telescope results. II. EHT and multiwavelength observations, data processing, and calibration. The Astrophysical Journal Letters, 930, L13.
10. Event Horizon Telescope Collaboration; Akiyama, K., Alberdi, A., Alef, W., Algaba, J. C., Anantua, R., Asada, K., ... & Zhao, S-S. (2022). First Sagittarius A* event horizon telescope results. III. Imaging of the galactic center supermassive black hole. The Astrophysical Journal Letters, 930, L14.
11. Event Horizon Telescope Collaboration; Akiyama, K., Alberdi, A., Alef, W., Algaba, J. C., Anantua, R., Asada, K., ... & Chang,D.O. (2022). First Sagittarius A* Event Horizon Telescope results. IV. Variability, morphology, and black hole mass. The Astrophysical Journal Letters, 930, L15.
12. Event Horizon Telescope Collaboration; Akiyama, K., Alberdi, A., Alef, W., Algaba, J. C., Anantua, R., Asada, K., ... & White, C. (2022). First Sagittarius A* event horizon telescope results. V. Testing astrophysical models of the galactic center black hole. The Astrophysical Journal Letters, 930, L16.
13. Event Horizon Telescope Collaboration; Akiyama, K., Alberdi, A., Alef, W., Algaba, J. C., Anantua, R., Asada, K., ... & Zhao, S-S. (2022). First Sagittarius A* event horizon telescope results. VI. Testing the black hole metric. The Astrophysical Journal Letters, 930, L17.
14. Oya, H. (2019). *Detection of decameter radio wave pulses from the center part of our galaxy suggesting sources at rotating super massive black hole binary.* TERRAPAB e-library,1-50. http://hdl.handle.net/10097/00126480
15. Abbott, B. P., Abbott, R., Abbott, T., Abernathy, M. R., Acernese, F., Ackley, K., ... & Cavalieri, R. (2016). Observation of gravitational waves from a binary black hole merger. *Physical review letters, 116,* 061102.
16. Abbott, B. P., Abbott, R., Abbott, T. D., Abernathy, M. R., Acernese, F., Ackley, K., ... & Chamberlin, S. J. (2016). GW151226: observation of gravitational waves from a 22-solar-mass binary black hole coalescence. *Physical review letters, 116,* 241103.
17. Abbott, B. P., Abbott, R., Abbott, T. D., Acernese, F., Ackley, K., ... & Cao, H. (2017). GW170104: observation of a 50-solar-mass binary black hole coalescence at redshift 0.2. *Physical review letters, 118,* 221101.
18. Abbott, B. P., Abbott, R., Abbott, T. D., Acernese, F., Ackley, K., Adams, C., ... & Callister, T. A. (2017). GW170814: a three-detector observation of gravitational waves from a binary black hole coalescence. *Physical review letters, 119*, 141101.
19. Oya. H. (2023). No gravitational wave from orbiting supermassive kerr black hole—a model of matter distribution and propagation of gravitational waves inside the event horizon. *Earth & Envi Scie Res & Rev 6*(1) 278-332. doi;10.33140/EESRR.06.01.01
20. Miyoshi, M., Kato, Y., & Makino, J. (2022). The jet and resolved features of the central supermassive black hole of M87 observed with the event horizon telescope (EHT). *The Astrophysical Journal, 933,* 36.
21. Event Horizon Telescope Collaboration; Akiyama,K., Alberdi, A. Alef,W., Asada, K., Azulay,R, Baczko,A.K.,Ball,D.,Baloković,M.,Barrett,J.,Bintley, D….& Ziurys, L. (2019). First M87 event horizon telescope results. I: The shadow of the supermassive black hole, *The Astrophysical Journal Letters. 875,* L1.
22. Event Horizon Telescope Collaboration; Akiyama,K., Alberdi, A. Alef,W., Asada, K., Azulay,R, Baczko,A. K., Ball,D., Baloković,M., Barrett,J., Bintley, D.,…& Ziurys, L. (2019). First M87 event horizon telescope results. II: array and instrumentation, *The Astrophysical Journal Letters, 875,* L2.
23. Event Horizon Telescope Collaboration; akiyama,k., al-

berdi, a. alef,w., asada, k., azulay,r ,baczko,a. k., ball,d.,baloković,m.,barrett,j.,bintley,d.,…& yamaguchi,p. (2019). First M87 event horizon telescope results. III. data processing and calibration,the astrophysical journal letters, 875, L3.
24. Event Horizon Telescope Collaboration; Akiyama,K., Alberdi, A., Alef, W., Asada, K., Azulay, R., Baczko, A. K., ... & Yamaguti, P. (2019). First M87 event horizon telescope results. IV. Imaging the central supermassive black hole. The Astrophysical Journal Letters, 875 L4.
25. Event Horizon Telescope Collaboration; Akiyama, K., Alberdi, A., Alef, W., Asada, K., Azulay, R., Baczko, A. K., ... & Zhang, S. (2019). First M87 event horizon telescope results. V. Physical origin of the asymmetric ring. The Astrophysical Journal Letters, 875, L5.
26. Event Horizon Telescope Collaboration; Akiyama, K., Alberdi, A., Alef, W., Asada, K., Azulay, R., Baczko, A. K., ... & Yamaguti, P. (2019). First M87 event horizon telescope results. VI. The shadow and mass of the central black hole. The Astrophysical Journal Letters, 875, L6.
27. Fish, V. L., Doeleman, S. S., Beaudoin, C., Blundell, R., Bolin, D. E., Bower, G. C., ... & Ziurys, L. M. (2011). The 1.3 mm wavelength VLBI of Sagittarius A*: Detection of time-variable emission on event horizon scales. The Astrophysical Journal Letters, 727, L36.
28. Oya, H. (2022). Interpretation of time-varying radio emissions of SgrA* observed by 1.3 millimeter-wavelength VLBI---with parameters of the super-massive black hole binary at SgrA* based on decameter radio wave pulse observations. *Earth Envi Scie Res & Rev, 5*(4), 185-216. doi.;10.33140/EESRR.05.04.05
29. Oya, H. (2023). Confirmation of Sgr A* using the event horizon telescope data as extreme binary of the supermassive black holes concluded by decameter radio wave pulse observations. Adv Theo Comp Phy,(3), 123-170. doi.;10.33140/ATCP.06.03.02
30. The Event Horizon Telescope Collaboration. First Sagittarius A* EHT results: Calibrated data. doi: 10.25739/m140-ct59.
31. Lu, R. S., Asada, K., Krichbaum, T. P., Park, J., Tazaki, F., Pu, H. Y., ... & Yu, C. Y. (2023). A ring-like accretion structure in M87 connecting its black hole and jet. *Nature, 616*(7958), 686-690.
32. Wielgus, M., Marchili, N., Martí-Vidal, I., Keating, G. K., Ramakrishnan, V., Tiede, P., ... & Liu, J. (2022). millimeter light curves of Sagittarius A* observed during the 2017 event horizon telescope campaign. *The Astrophysical Journal Letters, 930,* l19.
33. Wielgus, M., Moscibrodzka, M., Vos, J., Gelles, Z., Marti-Vidal, I., Farah, J., ... & Messias, H. (2022). Orbital motion near Sagittarius A*-Constraints from polarimetric ALMA observations. *Astronomy & Astrophysics, 665,* L6.
34. Högbom, J. A. (1974). Aperture synthesis with a non-regular distribution of interferometer baselines. *Astronomy and Astrophysics Supplement, 15,* 417.
35. Luminet, J. P. (1979). Image of a spherical black hole with thin accretion disk. *Astronomy and Astrophysics, 75,* 228-235.
36. Fukue, J. (2003). Silhouette of a dressed black hole. *Publications of the Astronomical Society of Japan, 55*, 155-159.
37. Falcke, H., Melia, F., & Agol, E. (1999). Viewing the shadow of the black hole at the galactic center. *The Astrophysical Journal, 528*, L13.
38. Bromley, B. C., Melia, F., & Liu, S. (2001). Polarimetric imaging of the massive black hole at the galactic center. *The Astrophysical Journal, 555,* L83.
39. Noble, S. C., Leung, P. K., Gammie, C. F., & Book, L. G. (2007). Simulating the emission and outflows from accretion discs. *Classical and Quantum Gravity, 24*, S259.
40. Kamruddin, A. B., & Dexter, J. (2013). A geometric crescent model for black hole images. *Monthly Notices of the Royal Astronomical Society, 434,* 765-771.
41. Lu, R. S., Broderick, A. E., Baron, F., Monnier, J. D., Fish, V. L., Doeleman, S. S., & Pankratius, V. (2014). Imaging the supermassive black hole shadow and jet base of M87 with the event horizon telescope. *The Astrophysical Journal, 788*, 120.
42. Bird, S., Harris, W. E., Blakeslee, J. P., & Flynn, C. (2010). The inner halo of M 87: a first direct view of the red-giant population. *Astronomy & Astrophysics, 524,* A71.
43. Blakeslee, J. P., Jordán, A., Mei, S., Côté, P., Ferrarese, L., Infante, L., ... & West, M. J. (2009). The ACS Fornax cluster survey. V. Measurement and recalibration of surface brightness fluctuations and a precise value of the Fornax–Virgo relative distance. *The Astrophysical Journal, 694*, 556.
44. Cantiello, M., Blakeslee, J. P., Ferrarese, L., Côté, P., Roediger, J. C., Raimondo, G., ... & Cuillandre, J. C. (2018). The next generation virgo cluster survey (NGVS). XVIII. Measurement and calibration of surface brightness fluctuation distances for bright galaxies in virgo (and beyond). *The Astrophysical Journal, 856*, 126.
45. Gebhardt, K., Adams, J., Richstone, D., Lauer, T. R., Faber, S. M., Gültekin, K., ... & Tremaine, S. (2011). The black hole mass in M87 from Gemini/NIFS adaptive optics observations. *The Astrophysical Journal, 729,* 119.
46. Landau, L. D., & Lifshitz, E. M. (1967). Classical theory of fields (3rd revised English edition). Pergamon Press.
47. Valtonen, M. J., Dey, L., Hudec, R., Zola, S., Gopakumar, A., Mikkola, S., ... & OJ287-15/16 Collaboration. (2017). High accuracy measurement of gravitational wave back-reaction in the OJ287 black hole binary. *Proceedings of the International Astronomical Union, 13*(S338), 29-36.
48. Britzen, S., Fendt, C., Witzel, G., Qian, S. J., Pashchenko, I. N., Kurtanidze, O., ... & Witzel, A. (2018). OJ287: deciphering the 'Rosetta stone of blazars'. *Monthly Notices of the Royal Astronomical Society, 478*, 3199-3219.
49. Miyoshi, M., Kato, Y., Makino, J., & Tsuboi, M. (2024). The jet and resolved features of the central supermassive black hole of M87 observed with EHT in 2017—comparison with the GMVA 86 GHz results. *The Astrophysical Journal Letters, 963*, 118.

**Appendix A**

We rewrite eqs.(3.4), (3.5), and (3.6) in the main text with an interpretation of the symbols used there in the form of a matrix as follows:

$$\begin{pmatrix} -sin\phi_{Sg} & cos\phi_{Sg} & 0 \\ -sin\delta_{Sg}cos\phi_{Sg} & -sin\delta_{Sg}sin\phi_{Sg} & cos\delta_{Sg} \\ cos\delta_{Sg}cos\phi_{Sg} & cos\delta_{Sg}sin\phi_{Sg} & sin\delta_{Sg} \end{pmatrix} \begin{pmatrix} \hat{x}_e \\ \hat{y}_e \\ \hat{z}_e \end{pmatrix} = \begin{pmatrix} \hat{u} \\ \hat{v} \\ \hat{w} \end{pmatrix}$$

(A1)

By solving this linear equation with respect to $\hat{x}_e, \hat{y}_e,$ and $\hat{z}_e$ in terms of unit vectors $\hat{u}$, $\hat{v}$, and $\hat{w}$, we find the following relations, as follows:

$$\hat{x}_e = -sin\phi_{Sg}\,\hat{u} - sin\delta_{Sg}cos\phi_{Sg}\hat{v} + cos\delta_{Sg}cos\phi_{Sg}\,\hat{w}, \qquad (A2)$$

$$\hat{y}_e = \; cos\phi_{Sg}\,\hat{u} - sin\delta_{Sg}sin\phi_{Sg}\hat{v} + cos\delta_{Sg}sin\phi_{Sg}\,\hat{w}, \qquad (A3)$$

and

$$\hat{z}_e = cos\delta_{Sg}\hat{v} + sin\delta_{Sg}\,\hat{w}. \qquad (A4)$$

By inserting the above eqs.(A2), (A3), and (A4) into eq.(3.2) in the main text, the unit vector $\hat{y}$ that is parallel to the orbital motion of ECB-SMBH observed from Earth is expressed by:

$$\begin{aligned} \hat{y} = {} & \left(cos\delta_{Gp}sin\delta_{Sg}sin\phi_{Gp} - cos\delta_{Sg}sin\delta_{Gp}sin\phi_{Sg}\right)\left(-sin\phi_{Sg}\,\hat{u} - sin\delta_{Sg}cos\phi_{Sg}\hat{v}\right. \\ & \left. + cos\delta_{Sg}cos\phi_{Sg}\,\hat{w}\;\right)^{+}\left(cos\delta_{Sg}sin\delta_{Gp}cos\phi_{Sg}\right. \\ & \left. - sin\delta_{Sg}cos\delta_{Gp}cos\phi_{Gp}\right)\left(cos\phi_{Sg}\,\hat{u} - sin\delta_{Sg}sin\phi_{Sg}\hat{v}\right. \\ & \left. + cos\delta_{Sg}sin\phi_{Sg}\,\hat{w}\right) \\ & + \left(cos\delta_{Sg}sin\phi_{Sg}cos\delta_{Gp}cos\phi_{Gp}\right. \\ & \left. - cos\delta_{Sg}cos\phi_{Sg}cos\delta_{Gp}sin\phi_{Gp}\right)\left(cos\delta_{Sg}\hat{v} + sin\delta_{Sg}\,\hat{w}\right) \\ = {} & \left[cos\delta_{Sg}sin\delta_{Gp} - sin\delta_{Sg}cos\delta_{Gp}cos\left(\phi_{Gp} - \phi_{Sg}\right)\right]\hat{u} \\ & -\left[cos\delta_{Gp}sin\left(\phi_{Gp} - \phi_{Sg}\right)\right]\hat{v} \qquad (A5) \end{aligned}$$

## Appendix B

Table of information of EHT-VLBI observation stations [22].

| Facility | Abbreviation | Location | Latitude | Longitude | Elevation (m) |
|---|---|---|---|---|---|
| ALMA | AA | Chile | $-23^{\circ}01'45''.1$ | $-67^{\circ}45'17''.1$ | 5074.1 |
| APEX | AP | Chile | $-23^{\circ}00'20''.8$ | $-67^{\circ}45'32''.9$ | 5104.5 |
| JCMT | JC | Hawaii USA | $+19^{\circ}49'22''.2$ | $-155^{\circ}28'37''.3$ | 4120.1 |
| LMT | LM | Mexico | $+18^{\circ}59'08''.8$ | $-97^{\circ}18'53''.2$ | 4593.3 |
| PV 30m | PV | Spain | $+37^{\circ}03'58''.1$ | $-3^{\circ}23'33''.4$ | 2919.5 |
| SMA | SM | Hawaii USA | $+19^{\circ}49'27''.2$ | $-155^{\circ}28'39''.1$ | 4115.1 |
| SMT | AZ | Arizona USA | $+32^{\circ}42'05''.8$ | $-109^{\circ}53'28''.5$ | 3158.7 |
| SPT | SP | Antarctica | $-89^{\circ}59'22''.9$ | $-45^{\circ}15'00''.3$ | 2816.5 |

## Appendix C

Starting from the expression of the basic equation related to linearized visibility given in eq.(3.14) as

$$S(\mathrm{p},\theta_0)=\int\int V_L(\ell,\theta_0)exp(i\mathrm{p}\ell)d\ell\ , \qquad (C1)$$

we consider here the real component of the visibility restricted to $\mathrm{p}\ell=\mathrm{p}\ell_{ij}$ rewriting the magnitude of wave vectors coming from the source position p by:

$$\mathrm{p}=\frac{2\pi}{\lambda}cos\Theta. \qquad (C2)$$

with the detection angle $\Theta$ by VLBI of $\ell_{ij}$ baseline for wavelength $\lambda$. Subsequently, the concerning linearized visibility $LV_{ij}$ is expressed by,

$$LV_{ij}=W_{ij}^{*}cos\left(\frac{2\pi}{\lambda}\ell_{ij}cos\Theta\right). \qquad (C3)$$

where $W_{ij}^{*}$ is the visibility amplitude. We rewrite the observing angle $\Theta$ by introducing the $\Delta\Theta$ as the angle corresponding to the deviation of the source position due to the ECB-SMBH orbiting motion, as follows:

$$\Theta=\Theta_0+\Delta\Theta. \qquad (C4)$$

where $\Theta_0$ is the angle corresponding to the direction of the Galaxy center. By finding a

correlation with the visibility toward the Galaxy center, then:

$$LV_{ij} = W_{ij}^{*}\langle cos\left[\frac{2\pi}{\lambda}\ell_{ij}cos(\Theta_0 + \Delta\Theta)\right]\cdot\ cos\left(\frac{2\pi}{\lambda}\ell_{ij}cos\Theta_0\right)\rangle$$

$$= W_{ij}^{*}\langle cos\left[\frac{2\pi}{\lambda}\ell_{ij}cos(\Theta_0 + \Delta\Theta)\right]\cdot\ cos\left(\frac{2\pi}{\lambda}\ell_{ij}cos\Theta_0\right)\rangle$$

$$= \frac{W_{ij}^{*}}{2}cos\left\{\frac{2\pi}{\lambda}\ell_{ij}[cos(\Theta_0 + \Delta\Theta) - cos\Theta_0]\right\}. \qquad (C5)$$

Assuming $\Theta_0 \gg \Delta\Theta$, and rewriting as $W_{ij} = W_{ij}^{*}/2$, it follows that:

$$LV_{ij} = W_{ij}cos\left(\frac{2\pi}{\lambda}sin\Theta_0 \cdot \ell_{ij}\Delta\Theta\right), \qquad (C6)$$

This expression is given as eq.(3.18) in the main text.

## Appendix D

We repeat eq.(4.4) in the main text here as,

$$V_L(\ell, \theta_0, T_m) = \frac{1}{2\pi}\left\{\int_{a-b}^{a+b} A_0 \cdot \cos\left[\frac{\pi(p-a)}{2b}\right]\cdot cos(-\ell\mathrm{p})d\mathrm{p}\right.$$
$$\left. + \int_{-a-b}^{-a+b} A_0 \cdot \cos\left[\frac{\pi(p+a)}{2b}\right]\cdot cos(-\ell\mathrm{p})d\mathrm{p}\right\}. \qquad (\mathrm{D}-1)$$

Considering $cos(-\ell\mathrm{p}) = cos(\ell\mathrm{p})$, the second term on the right side of eq.(D-1) is rewritten by changing p to -p as follows:

$$\int_{-a-b}^{-a+b} A_0 \cdot \cos\left[\frac{\pi(p+a)}{2b}\right]\cdot cos(\ell\mathrm{p})d\mathrm{p}$$
$$= -\int_{a+b}^{a-b} A \cdot \cos\left[\frac{\pi(p-a)}{2b}\right]\cdot cos(\ell\mathrm{p})d\mathrm{p}. \qquad (\mathrm{D}-2)$$

Therefore eq.(D-1) is expressed by:

$$V_L(\ell, \theta_0, T_m) = \frac{1}{\pi}\int_{a-b}^{a+b} A_0 \cdot \cos\left[\frac{\pi(p-a)}{2b}\right]\cdot cos(\ell\mathrm{p})d\mathrm{p}$$
$$= \frac{1}{2\pi}\int_{a-b}^{a+b} A_0 \cdot cos\left(\frac{\pi a}{2b}\right)\left\{\cos\left[\left(\ell + \frac{\pi}{2b}\right)p\right] + \cos\left[\left(\ell - \frac{\pi}{2b}\right)p\right]\right\} d\mathrm{p}$$
$$+ \frac{1}{2\pi}\int_{a-b}^{a+b} A_0 \cdot sin\left(\frac{\pi a}{2b}\right)\left\{\sin\left[\left(\ell + \frac{\pi}{2b}\right)p\right] - \sin\left[\left(\ell - \frac{\pi}{2b}\right)p\right]\right\} d\mathrm{p}. \qquad (\mathrm{D}-3)$$

The integration of eq.(D-3) is then given by:

$$V_L(\ell,\theta_0,T_m)=\frac{A}{2\pi}cos\left(\frac{\pi a}{2b}\right)\left\{\left|\frac{1}{\ell+\frac{\pi}{2b}}\sin\left[\left(\ell+\frac{\pi}{2b}\right)p\right]\right|_{a-b}^{a+b}\right.$$
$$\left.+\left|\frac{1}{\ell-\frac{\pi}{2b}}\sin\left[\left(\ell-\frac{\pi}{2b}\right)p\right]\right|_{a-b}^{a+b}\right\}$$
$$-\frac{A_0}{2\pi}sin\left(\frac{\pi a}{2b}\right)\left\{\left|\frac{1}{\ell+\frac{\pi}{2b}}\cos\left[\left(\ell+\frac{\pi}{2b}\right)p\right]\right|_{a-b}^{a+b}-\left|\frac{1}{\ell-\frac{\pi}{2b}}\cos\left[\left(\ell-\frac{\pi}{2b}\right)p\right]\right|_{a-b}^{a+b}\right\}.$$
(D-4)

Furthermore, we continue the mathematical manipulations for the expression of $V_L(\ell,\theta_0,T_m)$ with given $\theta_0, and\ T_m$ as follows:

$$V_L(\ell,\theta_0,T_m)=\frac{A_0}{2\pi}cos\left(\frac{\pi a}{2b}\right)\left\{\frac{1}{\ell+\frac{\pi}{2b}}\cdot\sin\left[\left(\ell+\frac{\pi}{2b}\right)(a+b)\right]\right.$$
$$-\frac{1}{\ell+\frac{\pi}{2b}}sin\left[\left(\ell+\frac{\pi}{2b}\right)(a-b)\right]+\frac{1}{\ell-\frac{\pi}{2b}}\cdot\sin\left[\left(\ell-\frac{\pi}{2b}\right)(a+b)\right]$$
$$\left.-\frac{1}{\ell-\frac{\pi}{2b}}sin\left[\left(\ell-\frac{\pi}{2b}\right)(a-b)\right]\right\}$$
$$-\frac{A_0}{2\pi}sin\left(\frac{\pi a}{2b}\right)\left\{\frac{1}{\ell+\frac{\pi}{2b}}\cos\left[\left(\ell+\frac{\pi}{2b}\right)(a+b)\right]-\frac{1}{\ell+\frac{\pi}{2b}}\cos\left[\left(\ell+\frac{\pi}{2b}\right)(a-b)\right]\right.$$
$$\left.-\frac{1}{\ell-\frac{\pi}{2b}}\cos\left[\left(\ell-\frac{\pi}{2b}\right)(a+b)\right]+\frac{1}{\ell-\frac{\pi}{2b}}\cdot\cos\left[\left(\ell-\frac{\pi}{2b}\right)(a-b)\right]\right\}$$

$$=\frac{A_0}{\pi}cos\left(\frac{\pi a}{2b}\right)\left\{\frac{1}{\ell+\frac{\pi}{2b}}\cdot\cos\left[\left(\ell+\frac{\pi}{2b}\right)a\right]\cdot cos(\mathrm{b}\ell)-\frac{1}{\ell-\frac{\pi}{2b}}\cdot\cos\left[\left(\ell-\frac{\pi}{2b}\right)a\right]\right.$$
$$\left.\cdot cos(\mathrm{b}\ell)\right\}$$

$$-\frac{A_0}{\pi} sin\left(\frac{\pi a}{2b}\right)\left\{\frac{-1}{\ell+\frac{\pi}{2b}}\sin\left[\left(\ell+\frac{\pi}{2b}\right)a\right]\cdot\cos(\mathrm{b}\ell)+\frac{-1}{\ell-\frac{\pi}{2b}}\sin\left[\left(\ell-\frac{\pi}{2b}\right)a\right]\right.$$

$$\left.\cdot\cos(\mathrm{b}\ell)\right\} \qquad (D.5)$$

Further we rewrite eq.(D5), as

$$V_L(\ell,\theta_0,T_m)=\frac{A_0}{\pi}cos\left(\frac{\pi a}{2b}\right)cos(\mathrm{b}\ell)\left\{\frac{1}{\ell+\frac{\pi}{2b}}\cdot\cos\left[\left(\ell+\frac{\pi}{2b}\right)a\right]-\frac{1}{\ell-\frac{\pi}{2b}}\right.$$

$$\left.\cdot\cos\left[\left(\ell-\frac{\pi}{2b}\right)a\right]\right\}$$

$$+\frac{A_0}{\pi}sin\left(\frac{\pi a}{2b}\right)cos(\mathrm{b}\ell)\left\{\frac{1}{\ell+\frac{\pi}{2b}}\cdot\sin\left[\left(\ell+\frac{\pi}{2b}\right)a\right]+\frac{1}{\ell-\frac{\pi}{2b}}\right.$$

$$\left.\cdot\sin\left[\left(\ell-\frac{\pi}{2b}\right)a\right]\right\}. \qquad (D6)$$

Regarding eq.(D.6), we have two following relations:

$$\frac{1}{\ell+\frac{\pi}{2b}}\cdot\cos\left[\left(\ell+\frac{\pi}{2b}\right)a\right]-\frac{1}{\ell-\frac{\pi}{2b}}\cdot\cos\left[\left(\ell-\frac{\pi}{2b}\right)a\right]$$

$$=\frac{-\pi/b}{\ell^2-(\pi/2b)^2}cos\left(\frac{\pi a}{2b}\right)cos(a\ell)-\frac{2\ell}{\ell^2-(\pi/2b)^2}sin\left(\frac{\pi a}{2b}\right)sin(a\ell)\ , \qquad (D.7)$$

and

$$\frac{1}{\ell+\frac{\pi}{2b}}\cdot\sin\left[\left(\ell+\frac{\pi}{2b}\right)a\right]+\frac{1}{\ell-\frac{\pi}{2b}}\cdot\sin\left[\left(\ell-\frac{\pi}{2b}\right)a\right]$$

$$=\frac{2\ell}{\ell^2-(\pi/2b)^2}cos\left(\frac{\pi a}{2b}\right)sin(a\ell)-\frac{\pi/b}{\ell^2-(\pi/2b)^2}sin\left(\frac{\pi a}{2b}\right)cos(a\ell)\ , \qquad (D.8)$$

By inserting eqs.(D.7) and (D.8) into eq.(D.6), we obtain the final expression for LN as follows:

$$V_L(\ell,\theta_0,T_m) = \frac{A_0}{\pi}cos(\mathrm{b}\ell)\left[\frac{-\pi/b}{\ell^2-(\pi/2b)^2}cos^2\left(\frac{\pi a}{2b}\right)cos(a\ell)\right.$$

$$\left.-\frac{2\ell}{\ell^2-(\pi/2b)^2}cos\left(\frac{\pi a}{2b}\right)sin\left(\frac{\pi a}{2b}\right)sin(a\ell)\right]$$

$$+\frac{A_0}{\pi}cos(\mathrm{b}\ell)\left[\frac{2\ell}{\ell^2-(\pi/2b)^2}cos\left(\frac{\pi a}{2b}\right)sin\left(\frac{\pi a}{2b}\right)sin(a\ell)\right.$$

$$\left.-\frac{\pi/b}{\ell^2-(\pi/2b)^2}sin^2\left(\frac{\pi a}{2b}\right)cos(a\ell)\right]$$

$$=\frac{A_0/b}{(\pi/2b)^2-\ell^2}\cdot cos(a\ell)\cdot cos(\mathrm{b}\ell)\,. \qquad (D.9)$$

**Appendix E**

Corresponding to the expression of the modulated period given in eq.(6.7), which we repeat as

$$T_{os} \approx T_0\left[1-\zeta cos\left(\frac{2\pi}{60}\right)t\right], \qquad (E1)$$

we can set the combination of sinusoidal functions $f(t)$ that give spectra peaks by the Fourier transformation, applying the WKB approximation, with arbitrary constant A, as follows:

$$f(t) = Acos\left(\int_{t_0}^{t}\frac{2\pi}{T_{os}}dt\right) = Acos\left[\int_{t_0}^{t}\frac{2\pi}{T_0}\left(1+\zeta cos\left(\frac{2\pi}{60}\right)t\right)dt\right]\,. \qquad (E2)$$

To make the mathematical manipulation tractable, we rewrite the symbols of eq.(E2) here, as

$$\omega_{0S} \equiv 2\pi/T_0 \quad , \quad p_{0S} \equiv 2\pi/60, \;\; and\; \xi_{0S} \equiv (2\pi/T_0)\cdot\zeta\,. \qquad (E3)$$

Subsequently, eq.(E2) is further written by:

$$f(t) = Acos\left[\omega_{0S}t+\frac{\xi_{0S}}{p_{0S}}sin(p_{0S}t)-\theta_{0S}\right]. \qquad (E4)$$

where $\theta_{0S}$ is a constant phase angle given as values at the starting time $t_0$ as follows:

$$\theta_{0S} = \omega_{0S}t_0 + \frac{\xi_{0S}}{p_{0S}} sin(p_{0S}t_0). \qquad (E5)$$

To see the sinusoidal components as elements of peaks in the resulting Fourier transformation, we rewrite eq.(E4) further, as follows:

$$f(t) = A \cdot cos(\omega_{0S}t - \theta_{0S}) cos\left[\frac{\xi_{0S}}{p_{0S}} sin(p_{0S}t)\right] - A \cdot sin(\omega_{0S}t - \theta_{0S}) sin\left[\frac{\xi_{0S}}{p_{0S}} sin(p_{0S}t)\right]. \qquad (E6)$$

Then, using the first kind Bessel functions $J_n(z)$ for order n with argument $z$ that provide:

$$cos\left[\frac{\xi_{0S}}{p_{0S}} sin(p_{0S}t)\right] = J_0(\xi_{0S}/p_{0S}) + 2J_2(\xi_{0S}/p_{0S}) cos(2p_{0S}t) + \cdots\cdots\cdots, \qquad (E7)$$

and

$$sin\left[\frac{\xi_{0S}}{p_{0S}} sin(p_{0S}t)\right] = 2J_1(\xi_{0S}/p_{0S}) sin(p_{0S}t) + 2J_3(\xi_{0S}/p_{0S}) sin(3p_{0S}t) + \cdots\cdots\cdots, \qquad (E8)$$

eq.(E6) is rewritten by

$$\begin{aligned} f(t) = A\{&J_0(\xi_{0S}/p_{0S}) cos(\omega_{0S}t - \theta_{0S}) - 2J_1(\xi_{0S}/p_{0S}) sin(\omega_{0S}t - \theta_{0S}) sin(p_{0S}t) \\ &+ 2J_2(\xi_{0S}/p_{0S}) cos(\omega_{0S}t - \theta_{0S}) cos(2p_{0S}t) \\ &- 2J_3(\xi_{0S}/p_{0S}) sin(\omega_{0S}t - \theta_{0S}) sin(3p_{0S}t) + \cdots\cdots\cdots\} \end{aligned} \qquad (E9)$$

This gives the final expression, as follows:

$$\begin{aligned} f(t) = A\{&J_0(\xi_{0S}/p_{0S}) cos(\omega_{0S}t - \theta_{0S}) + J_1(\xi_{0S}/p_{0S}) cos[(\omega_{0S} + p_{0S})t - \theta_{0S}] \\ &- J_1(\xi_{0S}/p_{0S}) cos[(\omega_{0S} - p_{0S})t - \theta_{0S}] \\ &+ J_2(\xi_{0S}/p_{0S}) cos[(\omega_{0S} + 2p_{0S})t - \theta_{0S}] \\ &+ J_2(\xi_{0S}/p_{0S}) cos[(\omega_{0S} - 2p_{0S})t - \theta_{0S}] \\ &+ \cdots\cdots\cdots\}. \end{aligned} \qquad (E10)$$

In the Fourier transformation, we calculate the absolute value of the results without phase information. That is, for the case of the term $J_0(\xi_{0S}/p_{0S}) cos(\omega_{0S}t - \theta_{0S})$ of

function $f(t)$, it follows that:

$$F_c(\omega) = \int_{-\infty}^{\infty} J_0(\xi_{0S}/p_{0S})cos(\omega_{0S}t - \theta_{0S})cos(\omega t)dt$$

$$= \int_{-\infty}^{\infty} J_0(\xi_{0S}/p_{0S})[\cos(\omega_{0S}t)\, cos\theta_{0S} + sin(\omega_{0S}t)sin\theta_{0S}]cos(\omega t)dt$$

$$= (1/2)J_0(\xi_{0S}/p_{0S})cos\theta_{0S} \qquad at\ \ \omega = \omega_{0S}\,. \qquad (E11)$$

Similarly, we have:

$$F_s(\omega) = \int_{-\infty}^{\infty} J_0(\xi_{0S}/p_{0S})cos(\omega_{0S}t - \theta_{0S})sin(\omega t)dt$$

$$= \int_{-\infty}^{\infty} J_0(\xi_{0S}/p_{0S})[\cos(\omega_{0S}t)\, cos\theta_{0S} + sin(\omega_{0S}t)sin\theta_{0S}]sin(\omega t)dt$$

$$= (1/2)\, J_0(\xi_{0S}/p_{0S})sin\theta_{0S} \qquad at\ \ \omega = \omega_{0S}\,. \qquad (E12)$$

We obtain the absolute value of the Fourier-transformed function as:

$$F(\omega_{0S}) = \sqrt{F_c(\omega)^2 + F_S(\omega)^2} = (1/2)J_0(\xi_{0S}/p_{0S})\,. \qquad (E13)$$

Thus, we can find the spectra peaks at angular frequencies $\omega_{0S} - 2p_{0S}$, $\omega_{0S} - p_{0S}$, $\omega_{0S}, \omega_{0S} + p_{0S}$, $\omega_{0S} + 2p_{0S}$ by calculating the absolute values of Fourier-transformed functions.